学位論文

Experimental search for hidden photon dark matter by using dish antenna method
(パラボラアンテナを用いた手法による hidden photon ダークマターの実験的探索)

平成 27 年 1 月 博士 (理学) 申請

東京大学大学院理学系研究科
物理学専攻
堀江 友樹

Experimental search for hidden photon dark matter by using dish antenna method

Tomoki Horie
Department of Physics, School of Science,
University of Tokyo

January 9, 2015

Abstract

We searched for the hidden photon cold dark matter(HPDM) in the mass region around 5×10^{-5} eV using dish antenna method. The experimental apparatus consists of a parabolic antenna with a 12-GHz band down converter and a plane aluminum mirror.

We looked for excess emission of electromagnetic wave derived from the HPDMs, but found no significant excess of the power and set the 95% confidence upper limit of $2.0 \times 10^{-12} - 8.0 \times 10^{-12}$ to the mixing angle χ for the hidden photon mass between 49.1865 and 53.3195 μeV. This is the most stringent limit in this mass region.

Contents

Chapter 1

Introduction

The characteristic of dark matter is still one of the most interesting open questions. Such new particles contribute about 27% of the total energy content of the Universe [1]. There are two leading candidates of the dark matter, Weakly interacting slim particles (WISPs) [2] and weakly interacting massive particles (WIMPs) [3]. WIMPs are searched for in the scattering experiments, while WISPs could be searched for by kinetic mixing with photons.

In this thesis, we focused on the "hidden photon" which belongs to a family of the WISPs. This particle arises from extensions of the Standard Model, especially the String theory. Recently, it is argued that the similar mechanism for axion production in the early universe (so-called misalignment mechanism [4] [5] [6]) also works for hidden photons [13] [14].

Until now, a number of theoretical studies and experimental searches for hidden photons have been done and they impose limits on the parameters of the hidden photon models, but most of these searches do not assume the hidden photon being dark matter.

On the other hand, halo-scopes such as ADMX [19](and CARRACK II [20]) are direct dark matter searches. They are built to search for axions, but also have sensitivity to hidden photon dark matter (HPDM). They use a resonant cavity, and achieve extremely high sensitivity when the energy of the dark matter particle corresponds to the frequency of the cavity. However, there is no prediction for the mass of HPDM. To search for HPDM, therefore, we need a broadband experiment which can scan over the wide range of the mass region fast and easily. To meet the demand, D. Horns and others [23] proposed a non-resonant broadband search strategy for HPDM (and other WISPy DM) using a "dish antenna". They found that a reflective surface can convert HPDMs into photons. If HPDMs are converted on the surface into photons, outgoing photons are perpendicular to the surface. So, in the proposal, they suggested to use a spherical mirror as the "dish".

In our experiment, however, we invented a method using a "parabolic" antenna which is more easily available than a spherical antenna. In this method, a parabolic antenna was used not for converting HPDMs into photons, but used to collect photons produced by the HPDM conversion. Aside of the parabolic antenna, we set a plane aluminum mirror to convert HPDMs to photons. If HPDMs are converted on the plane mirror, outgoing photons are plane wave, which can be collected by the parabolic antenna onto the focal point.

In this thesis, we explain what the hidden photon is in Chap. 2, previous studies and proposals in Chap. 3, the new searching methods in Chap. 4, calibrations in Chap. 5, measurement in Chap. 6, result and discussion in Chap. 7, and we conclude in Chap. 8.

Chapter 2

Hidden photon theories

In this chapter, we explain what the hidden photon is, and the recent argument that the hidden photon can be a candidate of dark matter. Also, we describe the parameter space for hidden photon cold dark matter(HP CDM).

2.1 Hidden photons

The Standard Model has some problems such as the strong CP problem. For this reason, many extensions of the Standard Model which solve the problems have been proposed. In some extensions, e.g. String theory, extra $U(1)$ symmetry arises frequently. A gauge boson corresponding to the "hidden" symmetry is called hidden photon (,dark photon, or paraphoton).

Okun and Holdom proposed the model that hidden photons interact with ordinary photons via kinetic mixing [7] [8], which is described by following Lagrangian,

$$\mathcal{L} = -\frac{1}{4}F_{\mu\nu}F^{\mu\nu} - \frac{1}{4}X_{\mu\nu}X^{\mu\nu} + \frac{\chi}{2}F_{\mu\nu}X^{\mu\nu} + \frac{m_{\gamma'}^2}{2}X_\mu X^\mu + J^\mu A_\mu, \tag{2.1}$$

where A_μ and X_μ are photon and HP field with field strength $F_{\mu\nu}$, $X_{\mu\nu}$ respectively, χ is the dimensionless parameter quantifying tiny kinetic mixing, $m_{\gamma'}$ is mass of HP, and J^μ is the ordinary electromagnetic current. As we can see, the new parameters in this Lagrangian are χ and $m_{\gamma'}$.

The kinetic mixing is generated at one-loop by the exchange of heavy messengers that couple both to the ordinary photon and to the hidden photon with coupling constant g.

The parameter region constrained up to now are shown in Fig. 2.1. All limits on the parameters of HPs except "Haloscope" are, however, constrained by the experiments and astrophysical observations that do not require HP as dark matter. So, we will explain about these constraints a little bit on the way to describe HPs (we can see the detailed review in [2]). For "Haloscope", however, we discuss this experiment in more detail in the following chapter.

In Eq. (2.1), the somewhat unusual kinetic mixing term has been introduced. To get a better understanding, it is suitable to remove this term.

To eliminate the kinetic mixing term, it is convenient to introduce a field re-definition. There are two simple shift that we can remove the kinetic mixing term of Eq. (2.1):

(1) $A^\mu \to \tilde{A}^\mu - \chi X^\mu$.
(2) $X^\mu \to \tilde{X}^\mu - \chi A^\mu$.

Although the resulting physics is completely equivalent, the physical picture resulting from both re-definitions is slightly different. Let us now consider about these pictures.

2.1.1 Model (1)

Inserting the shift $A^\mu \to \tilde{A}^\mu - \chi X^\mu$ into Eq. (2.1), and dropping terms of order $\sim \chi^2$, we obtain,

$$\mathcal{L} = -\frac{1}{4}\tilde{F}_{\mu\nu}\tilde{F}^{\mu\nu} - \frac{1}{4}X_{\mu\nu}X^{\mu\nu} + \frac{m_{\gamma'}^2}{2}X_\mu X^\mu + j^\mu(\tilde{A}_\mu - \chi X_\mu). \tag{2.2}$$

Note that this lagrandian describes the mass eigenstates called "massless" photon and "heavy" photon. According to Eq. (2.2), heavy photon couples to ordinary matter via

$$-\chi j^\mu X_\mu \tag{2.3}$$

This coupling causes the modification of Coulomb's law. In order to test the law, the Cavendish type precision experiments have been done, and these measurements provide the constraints labelled "Coulomb" (Fig. 2.1).

2.1.2 Model (2)

Inserting the shift $X^\mu \to \tilde{X}^\mu - \chi A^\mu$ into Eq. (2.1), dropping terms of order $\sim \chi^2$, we find,

$$\mathcal{L} = -\frac{1}{4}F_{\mu\nu}F^{\mu\nu} - \frac{1}{4}\tilde{X}_{\mu\nu}\tilde{X}^{\mu\nu} + \frac{m_{\gamma'}^2}{2}(\tilde{X}_\mu\tilde{X}^\mu - 2\chi A_\mu\tilde{X}^\mu + \chi^2 A_\mu A^\mu) + J^\mu A_\mu. \tag{2.4}$$

After inserting this shift, we can see the flavor eigenstates so-called "interacting" photon and "sterile" photon. Furthermore, we get a non-diagonal mass term. This term leads that hidden photon and photon can convert each one to another, in the same manner as neutrino oscillation. A number of theoretical and experimental search for HPs have been done up to now.

For example, helioscope and light shining through a wall (LSW) experiments can search a wide range of the relevant parameter space. In fact, we also have conducted the helioscope experiment [9]. This experiment searched for HPs produced outside and in the center of the Sun, and LSW experiments assume HPs produced in the laboratory.

The experimental and observational constraints of solar hidden photons are shown as "Tokyo" (the result of our experiment), "CAST" and "Solar Lifetime" [10] in Fig. 2.1. On the other hand, the current best constraint from LSW experiments is provided by ALPS [11]. The excluded area is shown as "LSW" in Fig. 2.1.

2.2 Hidden photon for candidate of dark matter

2.2.1 Summary of the misalignment mechanism

In this subsection, we describe that very light particles including HPs can be good candidates of dark matter. One of the most famous examples is the misalignment mechanism, discussed mostly for axions.

The mechanism relies on supposing that fields in the early universe have a random initial state. And the fields will be smoothed by the expansion of the universe. Even so, the zero-momentum component of the scalar field ϕ in the FRW (Friedmann-Robertson-Walker) background with mass m has the equation of motion:

$$\ddot{\phi} + 3H\dot{\phi} + m^2\phi = 0, \tag{2.5}$$

where H is the time-dependent Hubble parameter. This equation is reminiscent of the damped harmonic oscillator with damping term H.

In the early Universe ($H(t) \gg m$), ϕ act as an over-damped oscillator. After inflation, the H(t) becomes diminished. After the time t_0 characterized by $9H^2(t_0) - 4m^2 = 0$, the discriminant of Eq. (2.5) becomes negative, and the field A begins to oscillate and we can call them "particles". The particles are extremely cold and non-relativistic, regardless of their mass. An adiabatic perturbation spectrum derived from the fluctuations of the inflation field will produce adiabatic spatial variations on the density of the scalar particles, as needed to fit the WMAP data.

Now, let us come back to the discussion of HPs. Nelson and Scholtz have considered that a similar mechanism can apply to generate a population of HPs in the mass eigenstate basis discussed in Sect. 2.1 [14]. They calculated the equation of motion:

$$-\partial_\nu \left(X^{\mu\nu}\sqrt{(-g)} \right) = m_{\gamma'}^2 X^\mu \sqrt{(-g)} \tag{2.6}$$

where g is the coupling constant. As inflation expands a small patch of space, we can suppose HPs are uniformly distributed and pick a particular polarization.

This means $\partial_i X^\mu = 0$, and Eq. (2.6) enforces $X^0 = 0$. Using this, Eq. (2.6) satisfies,

$$\ddot{X}^i + 3H\dot{X}^i + m_{\gamma'}^2 X^i = 0 \tag{2.7}$$

This equation has the same form as Eq. (2.5).

Additionally, as argued in [13], we will consider two possible scenarios for the direction of the **X** field in the following.

(a) The direction is not affected by structure formation, and all HPs point in the same direction
(b) The direction changes during the process of structure formation and behave with random directions.

These have crucial consequences for direct detection.

If we assume that all the dark matter energy density in the galactic halo of order,

$$\rho_{\mathrm{CDM,halo}} \simeq \frac{0.3\mathrm{GeV}}{\mathrm{cm}^3}, \tag{2.8}$$

consisted of a hidden photon condensate, then the energy density is given by

$$\rho_{\mathrm{HP}} = \frac{m_{\gamma'}^2}{2}\langle|\mathbf{X}_{\mathrm{DM}}|^2\rangle = \rho_{\mathrm{CDM,halo}} \simeq \frac{0.3\mathrm{GeV}}{\mathrm{cm}^3}. \tag{2.9}$$

The average is only relevant in the case (b) and trivial in the case (a).

2.2.2 Allowed parameter space for HP CDM

Although HPs can be a candidate of dark matter, we must make sure of allowed parameter space for HP CDM by considering that HPs do not decay, or spoil observations such as CMB. This computation has been done in [13], and this leads to constraints on the kinetic mixing parameter.

The allowed parameter space for HP CDM is shown in Fig. 2.1. In this section, we will explain about the suppression of the kinetic mixing.

Let us come back to the discussion of the model (1). In this basis, we can identify that $\tilde{A}$ and X are the propagation eigenstates in vacuum. The universe is, however, not empty. The interactions between photons and the charged particle in the primordial plasma induce refraction and absorption. This can be represented with an effective mass squared of photon,

$$M^2 \equiv m_\gamma^2 + i\omega\Gamma, \tag{2.10}$$

where both the plasma mass m_γ and the interaction rate Γ depend on the photon frequency ω, and the modules of the wavenumber k [12]. As argued in [13], if

$\Gamma \neq 0$, the HPDMs decay with rates $\Gamma' = \chi_{\text{eff}}\Gamma$, where χ_{eff} is effective mixing angle which can be approximated by

$$\chi^2_{\text{eff}} \simeq \frac{\chi^2 m^4_{\gamma'}}{\left(m^2_\gamma - m^2_{\gamma'}\right)^2 + \mu^4} \tag{2.11}$$

where $\mu^2 = \max\{\chi m^2_{\gamma'}, m_{\gamma'}\Gamma\}$. Before recombination, m^2_γ is positive so there might be a moment where plasma mass is equal to $m_{\gamma'}$. According to Eq. (2.11), this equality causes the resonance.

The decay of the HP condensate can be written by the ratio

$$\frac{X_{\text{today}}}{X_{\text{initial}}} = \left(\frac{a_{\text{initial}}}{a_{\text{today}}}\right)^{3/2} \exp\left(-\frac{\tau_2}{2}\right), \qquad \left(\tau_2 \equiv \int_{t_{\text{initial}}}^{t_{\text{today}}} dt\Gamma'\right) \tag{2.12}$$

where a is the universe scale factor. The exponential term of this equation gives the damping of the total energy density due to the resonance.

In the mass range from neV to 10^4eV order, this disappearance mechanisms of HPs dominate. These caused not only the decay of the HP condensate, but also transferring energy to the ordinary electrons and producing extra photons. These can lead to effects such as CMB distortions or changing the effective number of relativistic neutrino species N^{eff}_ν. These bounds are calculated in [13] and shown as "CMB Distortions" and "N^{eff}_ν" in Fig. 2.1

The lower limit of the CMB constraints, $m_{\gamma'} \simeq$ neV, is coincident with resonances happening around the onset of recombination. Smaller HP masses suffer the resonance around this epoch because neutral Hydrogen affect m^2_γ to be a negative quantity which increases with time and finally makes $m^2_\gamma = 0$ by compensating the contribution of free electrons. HPs with sub-neV mass have their resonance around this epoch. However, we cannot ascertain the fate of the low energy photons injected during recombination, therefore we cannot constrain the kinetic mixing by this way. However, there is a simple way of limiting the kinetic mixing of HP CDMs in this small mass region. The density fluctuations are already imprinted in the CMB at late recombination, and they enable us to estimate the DM density. It was computed in [13], and the value agrees roughly with the average DM density observed today. Therefore, we cannot allow the resonant transition of HPs into photons at this epoch or any later, thus requiring about $\tau_2 < 1$, This bounds is shown in Fig. 2.1 labelled as "$\tau_2 > 1$".

If HP mass is below twice the electron mass, HP can decay into three photons. By considering that the population of decay photons is lower than the diffuse X-ray backgrounds, one can constrain the mixing parameter. This has been done in [12], and the excluded area is shown as "X-rays" in Fig. 2.1.

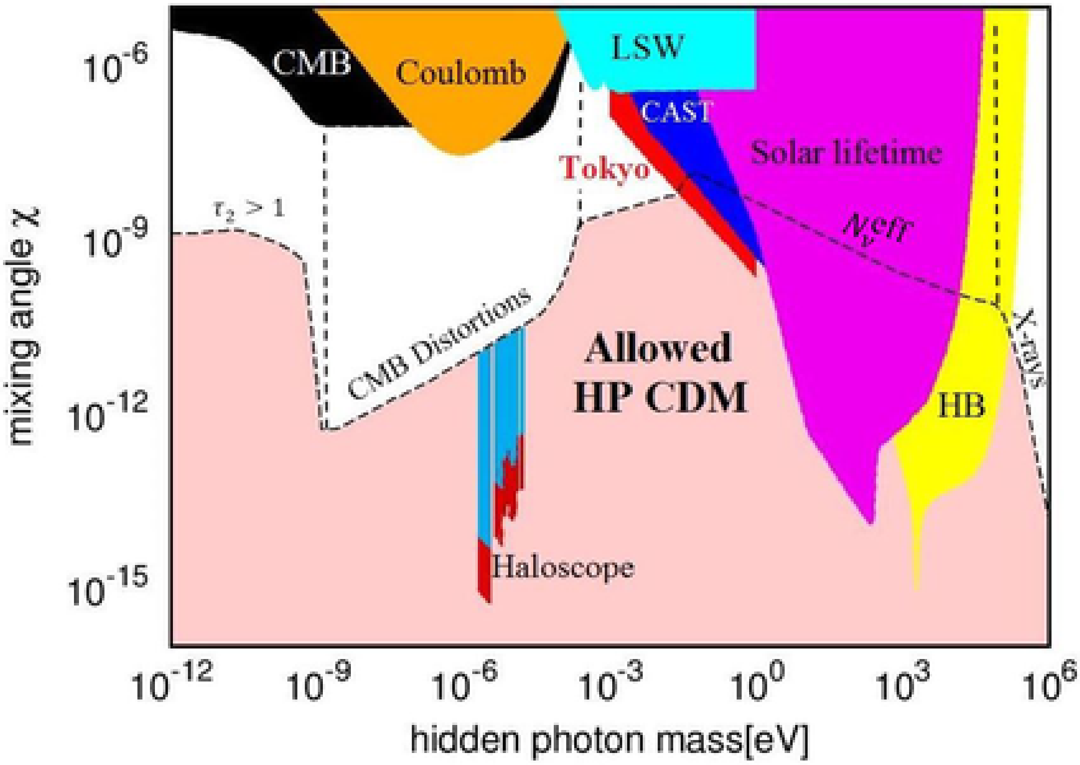

Figure 2.1: The allowed region of HPCDM is shown in light-red. The other painted regions arise from experiments and astrophysical observations that do not require HP dark matter except the region labelled "Haloscope". We explain several of them in the text.

Chapter 3

Previous studies and proposals to search for HPDM

In the past, haloscope searches had imposed the limit on the parameter space for HPDMs. Moreover, a new method to search for HPDMs (or other WISPy cold dark matter) is proposed recently. In this chapter, we will explain about the searches with haloscopes and the proposal.

3.1 Microwave cavity

One of the famous methods to search for WISPy dark matter is so-called "haloscopes". This tool has been used to search for axion dark matter, but this also has the sensitivity to HPDMs. Let us summarize the basic principle of the haloscope, and explain about the sensitivity to HPDMs.

Let us now come back to the discussion of HP-photon oscillation. In Eq. (2.4), we can see that the HP field plays a role as a source for the ordinary photon.

In the experiments, HP → photon conversion can resonantly occur when the frequency of conversion photon corresponds to the resonant frequency of the cavity. The energy of conversion photons corresponds to the energy of the incoming HPDMs. Since the HPDMs are very cold, their energy coincides approximately with their mass.

A number of experiments of this type have been already done [15–19], and the analysis to constrain HPDM parameters with these experiment has been carried out in [13]. The result of the analysis is shown in Fig. 2.1, with the "Haloscope" label.

3.2 Dish antenna

In this section, we will discuss a new technique with dish antennas. This method is proposed recently, and we applied this proposal to our experiment. Therefore, we will explain about this technique in more detail than others.

For discussion about the proposal, let us restart from Eq. (2.4). The equation of motion for plane waves with frequency ω and momentum k is,

$$\left[(\omega^2 - k^2)\begin{pmatrix} 1 & 0 \\ 0 & 1 \end{pmatrix} - m_{\gamma'}^2 \begin{pmatrix} \chi^2 & -\chi \\ -\chi & 1 \end{pmatrix}\right]\begin{pmatrix} \mathbf{A} \\ \mathbf{X} \end{pmatrix} = \begin{pmatrix} 0 \\ 0 \end{pmatrix}. \tag{3.1}$$

Since the particles are very cold, i.e. they have very small velocities, momentum k is nearly zero. Therefore, we can achieve $X^0 \approx A^0 \approx 0$ by a suitable gauge choice.

For a particle traveling with momentum $\mathbf{k}$ and frequency $\omega = \sqrt{m_{\gamma'}^2 + |\mathbf{k}|^2}$ we get,

$$\left.\begin{pmatrix} \mathbf{A} \\ \mathbf{X} \end{pmatrix}\right|_{\mathrm{DM}} = \mathbf{X}_{\mathrm{DM}}(\mathbf{k}) \begin{pmatrix} -\chi \\ 1 \end{pmatrix} \exp(-i(\omega t - \mathbf{kx})). \tag{3.2}$$

Although the field of HPDM is almost sterile, it has a small component of an ordinary electromagnetic field that will enable HPDMs to be detected.

$$\mathbf{E}_{\mathrm{DM}}(\mathbf{k}) = \chi m_{\gamma'} \mathbf{X}_{\mathrm{DM}}(\mathbf{k}) \tag{3.3}$$

In order to explain about the dark matter search using dish antennas, let us start considering a perfect plane mirror at z=0. In this case, an ordinary electric field is required to vanish on the surface in all directions parallel to the surface,

$$\mathbf{E}_{||}|_{\mathrm{surface of the plane}} = 0, \tag{3.4}$$

Here,the index || means the directions parallel to the plane. As a result, the ordinary electric field of the HPDM is cancelled by emitting a suitable outgoing almost ordinary electromagnetic plane wave[1] with the same frequency,

$$\begin{pmatrix} \mathbf{E} \\ \mathbf{E}_{\mathrm{hid}} \end{pmatrix}_{\mathrm{out}} = \mathbf{E}_{\mathrm{DM},||} \exp(-i(\omega t - \mathbf{px})) \begin{pmatrix} 1 \\ \chi \end{pmatrix}, \tag{3.5}$$

where $\mathbf{E}$ and $\mathbf{E}_{\mathrm{hid}}$ are visible and hidden electric field respectively.

On the plane at z=0, the field of HPDMs and outgoing wave satisfy the boundary condition Eq. (3.4),

---

[1] Note that, this wave has a tiny field of HPs, therefore, we named this “almost” ordinary photon.

$$\begin{aligned}\left(\begin{array}{c}\mathbf{E}\\ \mathbf{E}_{\text{hid}}\end{array}\right)_{\text{total},\|} &= \mathbf{E}_{\text{DM},\|}\left[\left(\begin{array}{c}1\\ \chi\end{array}\right)\exp(-i(\omega t-\mathbf{px}))+\frac{1}{\chi}\left(\begin{array}{c}-\chi\\ 1\end{array}\right)\exp(-i(\omega t-\mathbf{kx}))\right]_{z=0}\\ &= \mathbf{E}_{\text{DM},\|}\frac{1}{\chi}\left(\begin{array}{c}0\\ 1\end{array}\right). \qquad (3.6)\end{aligned}$$

By the boundary condition, we get,

$$\mathbf{p}\cdot\mathbf{x}|_{z=0}=\mathbf{k}\cdot\mathbf{x}|_{z=0}. \qquad (3.7)$$

Therefore,

$$\mathbf{p}_{\|}=\mathbf{k}_{\|}, \qquad (3.8)$$

and this decides two of three components of $\mathbf{p}$. The rest component can be determined by conservation of energy, which is described by,

$$|\mathbf{p}|=\omega=\sqrt{m_{\gamma'}^2+|\mathbf{k}^2|}. \qquad (3.9)$$

Clearly, we get,

$$\mathbf{p}=\sqrt{m_{\gamma'}^2+|\mathbf{k}_{\perp}|^2\mathbf{n}+\mathbf{k}_{\|}}, \qquad (3.10)$$

where $\mathbf{k}_{\perp}$ is the component of $\mathbf{k}$ which is perpendicular to the surface, and $\mathbf{n}$ is the unit vector which is perpendicular to the surface, too.

Since the momenta of the incoming HPDMs are non-relativistic $|\mathbf{k}| \ll m_{\gamma'}$, the outgoing electromagnetic waves are emitted at a small angle ($\phi \simeq |\mathbf{p}_{\|}|/m_{\gamma'}$) with respect to the axis which is normal to the surface (Fig. 3.1).

Therefore, if we use a dish antenna shaped spherically, these outgoing waves are concentrated in the center of the sphere, as recently discussed in [23] (Fig. 3.2). Nearly all dish antennas on the market, however, are not spherical, but parabolic. Furthermore, even if a parabolic antenna is very flat enough to be taken as approximately spherical, a receiver of the antenna is attached not to the center, but the focal point of the dish (Fig. 3.3).

In order to solve the problem, we invented a new method to search for HPDMs with "parabolic antenna" which can be realized easily. In Chap. 4, we will discuss the new technique.

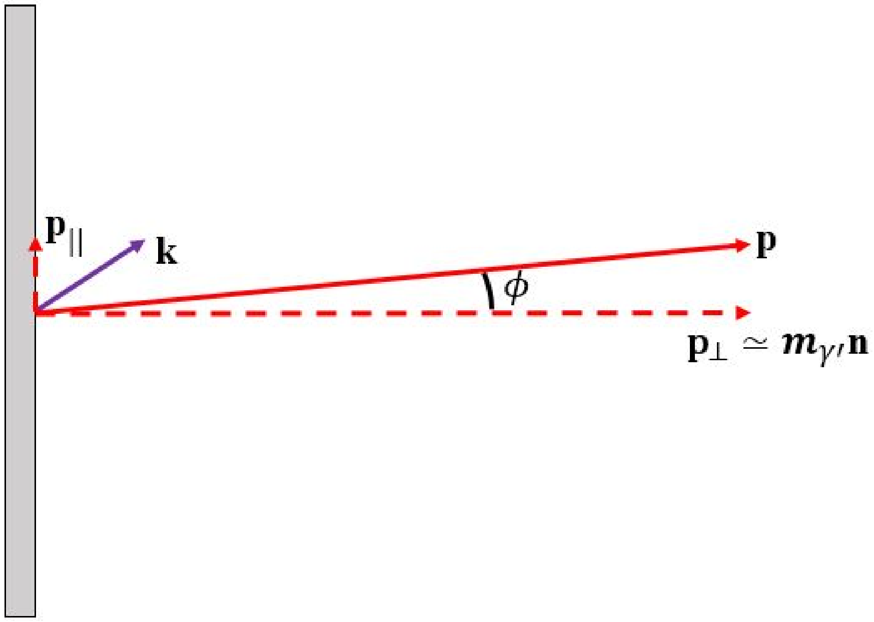

Figure 3.1: In response to an incoming HPDM, an outgoing (almost) ordinary photon is emitted at a small angle with respect to the axis which is normal to the surface.

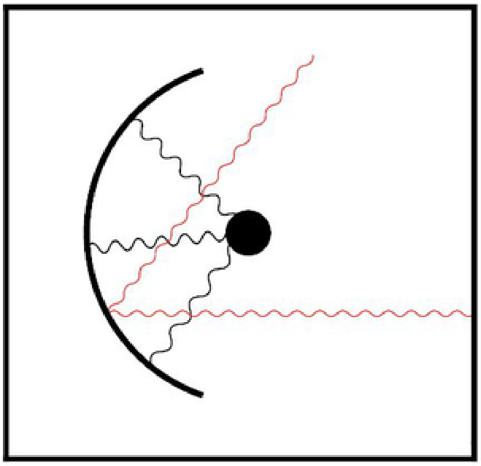

Figure 3.2: Schematic view of HPDM experiment using dish antenna.

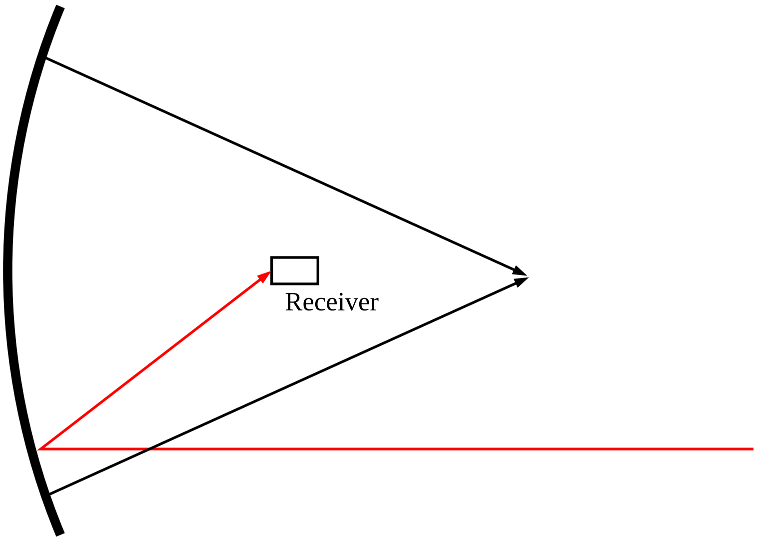

Figure 3.3: Schematic view of parabolic antenna which can be approximated by spherical one. But a receiver is attached to its focal point, not center.

We now estimate the sensitivity of a search experiment with practical parameters to the mixing parameter χ on the basis of the following assumptions:

- We assume that the vector field of HPDM $\mathbf{X}_{\mathrm{DM}}$ has random directions(case (b)).
- We assume the isothermal dark matter halo, i.e. the velocity of the HPDMs obeys Maxwell-Boltzmann distribution.
- We assume that the time over which HPDMs will interact coherently is much longer than our measurement time.

Note that, if the measurement time is longer than signal coherence time, the shape of signal derived from HPDMs is modulated as argued in ref. [27]. However, there is no prediction of the coherence time. Therefore, we assumed the coherence time is much longer than the measurement time as is implied in the analysis of "Haloscope" [13]. In this assumption, the shape of signal derived from HPDMs is not affected by the incoherence. On the other hand, if the coherent time turns out to be relatively short, we will be able to evaluate the effect of the incoherence according to the arguments in ref. [27].

Let us consider the situation: the electrons of the mirror's surface oscillate under the tiny electromagnetic field of HPDMs. The outgoing photons have the field magnitude which is related to χ by Eq. (3.3) and is set by the dark matter density via,

$$\sqrt{\langle|\mathbf{E}_{\mathrm{DM},||}|^2\rangle} = \chi\sqrt{2\rho_{\mathrm{HP}}}\alpha \tag{3.11}$$

where α represents,

$$\begin{array}{lll} |\cos(\theta)| & \text{case (a)} & \text{and} \\ \sqrt{\frac{2}{3}} & \text{case (b).} & \end{array} \tag{3.12}$$

θ is the angle between the HP field (it points in the same direction everywhere and it is unknown for case (a)) and the surface of mirror. In case (b), this value arises from the average over the random orientation of the HPs.

The power collected into the receiver is approximately,

$$P_{\mathrm{center}} \simeq A_{\mathrm{eff}}\langle|\mathbf{E}_{\mathrm{DM},||}|^2\rangle = 2\langle\alpha^2\rangle_{\mathrm{dish}}\chi^2\rho_{\mathrm{HP}}A_{\mathrm{eff}}, \tag{3.13}$$

where A_{eff} is the effective area of the dish.

Therefore, the sensitivity to the kinetic mixing parameter is,

$$\chi_{\mathrm{sens}} = 4.5 \times 10^{-14}\left(\frac{P_{\mathrm{det}}}{10^{-23}\mathrm{W}}\right)^{\frac{1}{2}}\left(\frac{0.3\mathrm{GeV/cm}^3}{\rho_{\mathrm{HP}}}\right)^{\frac{1}{2}}\left(\frac{1\mathrm{m}^2}{A_{\mathrm{eff}}}\right)^{\frac{1}{2}}\left(\frac{\sqrt{2/3}}{\alpha}\right). \tag{3.14}$$

where P_{det} is the detectable power in presence of various backgrounds. The mass range which we focuced on is about 5×10^{-5}eV. In this region, $\chi_{\mathrm{sens}} \simeq 10^{-10}$ is required to surpass the existing constraint. If we use the dish antenna which has the effective area 1 m^2, $P_{\mathrm{det}} \simeq 5 \times 10^{-17}$ W is required.

In our experiment, room temperature black body radiation is the dominant background. As shown in the appendix A, the power of input noise to a receiver with frequency band width $\Delta\nu$ is,

$$P_{\mathrm{RT}} = k_{\mathrm{B}}T\Delta\nu, \tag{3.15}$$

where T is room temperature ($\simeq$ 300 K). The frequency dispersion of the signal derived from HPDMs is a few tens of kHz as estimated later in Sect 7.1. Therefore, the power of input noise can be estimated to be order of 4×10^{-17} W.

Since the required power sensitivity with the dish antenna which has the effective area 1 m^2 roughly corresponds to the power of the background, we can achieve required sensitivity easily.

On the other hand, we used the Fast Fourier Transform (FFT-analyzer, see Sect. 4.2). In our set up of searching for HPDMs, a bin bandwidth[2] of FFT power spectrum was set to 5 kHz in order that the signal derived from HPDMs has several bins wide (discussed in Chap. 7.1).

---

[2] In this thesis, we call the frequency bandwidth of a bin " Resolution Band Width (RBW) ".

Chapter 4

New method of searching for HPDM using parabolic antenna

4.1 How to search for HPDMs with parabolic antenna

As discussed in the previous chapter, it is the original idea to use a spherical antenna for searching for the HPDMs, but it may not be easily available because of the necessary conditions. Even if we can get the antenna, it may be difficult to calibrate the apparatus.

To avoid such problems, we decide to use a commercially available parabolic antenna. Unfortunately, however, we cannot collect the conversion photons with parabolic antenna alone. So, we devised the system using a combination of a parabolic antenna and a plane mirror. Fig. 4.1 is a sketch of the new method.

In this method, we used a parabolic antenna not as an emitter of the waves derived from HPDMs, but only to collect the plane waves. If a plane mirror emits the waves derived from HPDMs, emitted waves are plane waves. So they can be collected by a parabolic antenna easily.

In the following section, we explain about the experimental apparatuses separately.

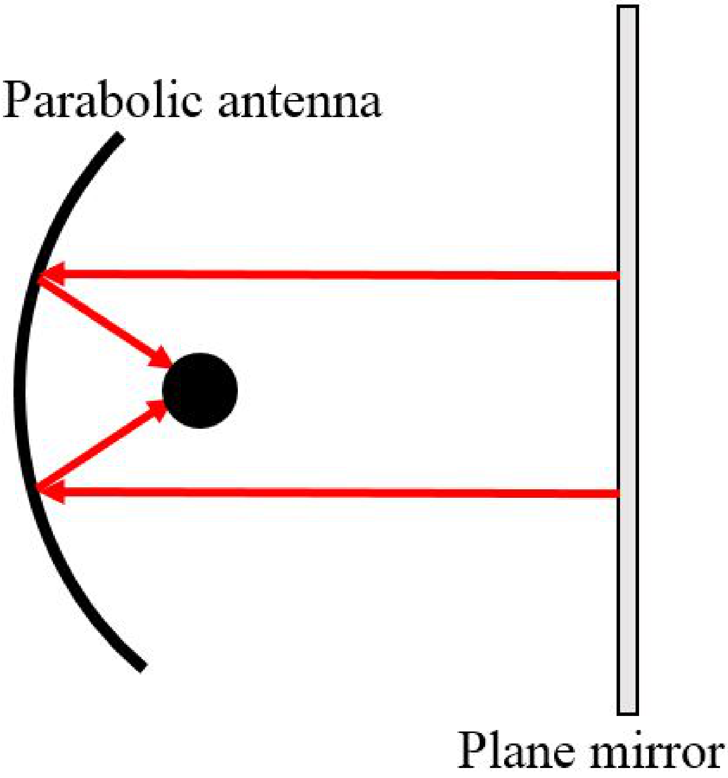

Figure 4.1: Schematic view of the new method.

4.2 Experimental apparatus

4.2.1 Parabolic antenna

The frequency band which we focused on is “Ku band” (12-18GHz). This band is used for satellite communications, especially broadcast services. In Japan, around 12GHz band is used for broadcasting satellite (BS) and communications satellite broadcasting (CS). We decided to use the parabolic antenna used for BS and CS broadcasting which is easily available.

As discussed in the previous chapter, $A_{\text{eff}} \geqq 1\text{m}^2$ is good condition to search for HPDMs.

Thus we used the parabolic antenna which has 2.2 m diameter (SXT-220, Anstellar, Fig. 4.2). In Japan, most parabolic antennas are off-axis feed, but SXT-220 is axial feed type. This antenna has a pillar named “king post” for supporting the dish and setting up the antenna on a ground or a floor (Fig. 4.3). We used the aluminum frames (HFS4590 series, Misumi) for legs of the antenna, and the channel bars for connecting the frames and the king post (Fig. 4.4).

Tab. 4.1 shows the specification of the dish. Let us explain the technical terms of radio astronomy used in the table.

The VSWR means “voltage standing wave ratio” which is a function of the reflection coefficient Γ known as return loss. This is defined by

$$\mathrm{VSWR} \equiv \frac{1+|\Gamma|}{1-|\Gamma|}. \tag{4.1}$$

For example, in Tab. 4.1, the VSWR value is 1.3. Therefore, the ratio of reflected power and input power is $|\Gamma|^2 \simeq 0.017$. This means about 98.3 percent of input power can be collected to the receiver.

“-3dB beam width” denotes the attenuation level when we incline the dish axis off the direction of the satellite. If we incline the axis by a half of the beam width with respect to the direction, then the gain attenuates by about half (-3dB).

“Gain” represents the ratio of the effective aperture of dish and the area of ideal isotropic antenna. For more information, see Appendix B.

Even if we incline the antenna by an angle larger than “-3dB beam width”, a small part of the power from the satellite can be collected by the dish. This efficiency is described as “side lobe”. Conversely, the antenna has a tiny sensitivity, even if the incident angle of the signal is large. For this reason, there were cases where we obtained the signals from exterior sources when we conducted the measurement of searching for HPDMs. This problem is discussed in Chap. 6 and Appendix C.

Finally, “Noise temperature” denotes the black body radiation from the ground, which the antenna can collect when the elevation angle of the antenna is small. For example, according to Tab. 4.1, the power of the radiation collected by the antenna corresponds to the power of black body radiation at 42K when elevation angle is 10°.

Figure 4.2: Picture of the parabolic antenna

Diameter	2.2m
Frequency	10.95 to 12.75 GHz
VSWR	1.3:1
Insertion loss	0.2dB
-3dB Beamwidth	0.708°
Side lobe	$32 - 25\log\theta$ $2^\circ \leqq \theta \leqq 20^\circ$
Gain	47.32dB (at 12.5GHz)
Noise temperature	42 K at 10°
Antenna optics	Prime-focus antenna
Elevation adjustment	5 to 90 °
Azimuth Adjustment	0 to 360 °

Table 4.1: The specification of the parabolic antenna

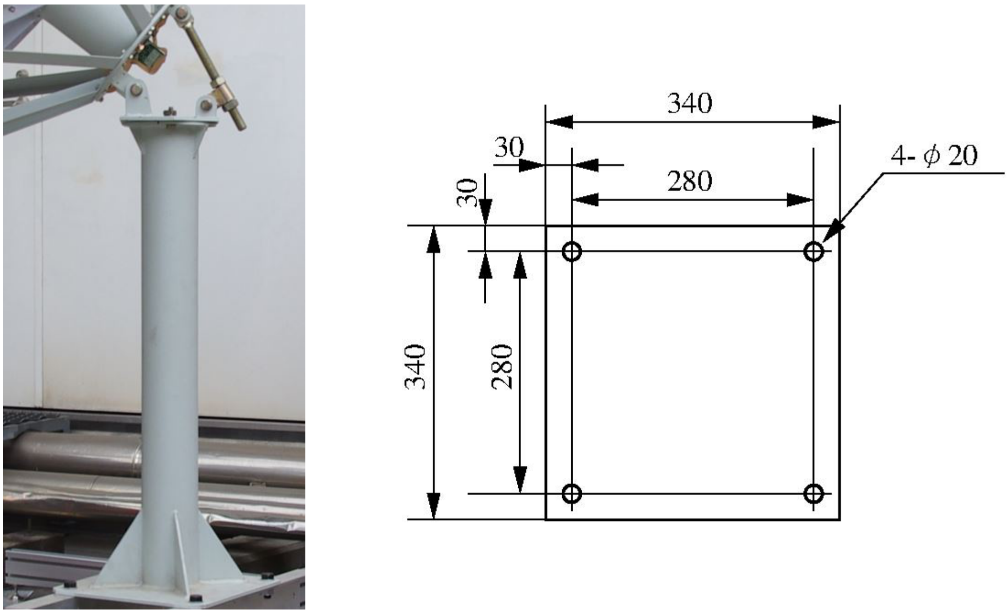

Figure 4.3: Left: Photograph of king post. Right:Schematic bottom view of king post.

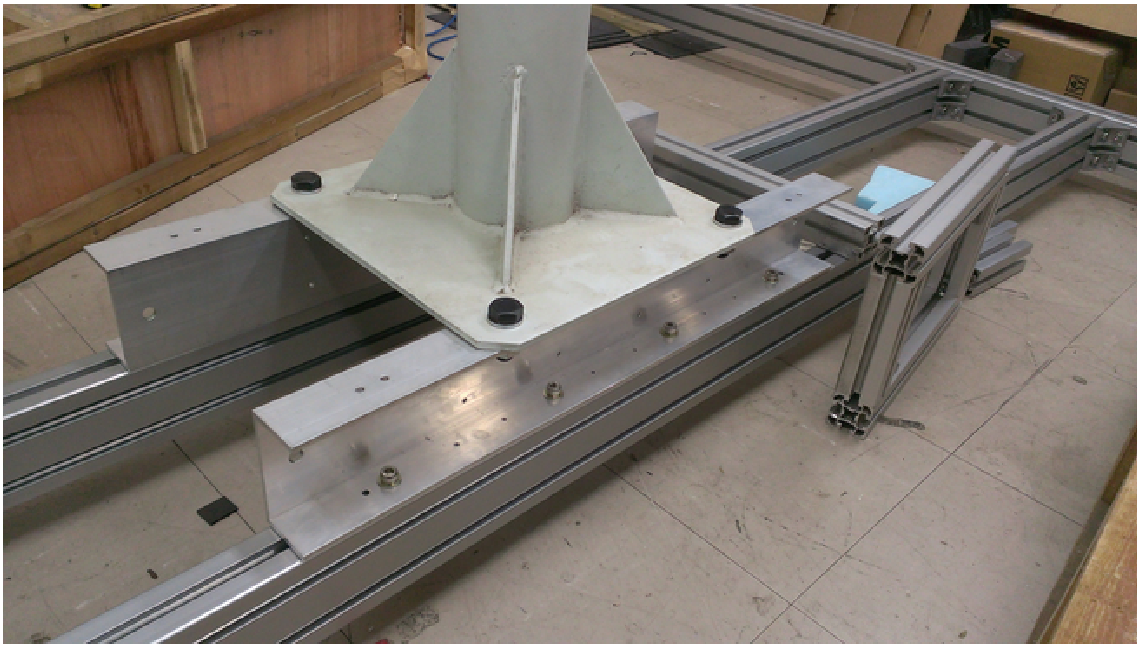

Figure 4.4: Two channels connecting king post and the flames

4.2.2 Low Noise Block converter(LNB)

We used a Low Noise Block down-converter with Feedhorn (LNBF) at the focal point of the dish (Fig. 4.5). The LNBF which we selected is Norsat 4506B. This LNBF is normally used as a receiver for CS broadcasting whose wave polarization is linear. Thus, for the following discussion, we also call it the “receiver”.

The receiver has 11.3GHz local oscillation frequency with which LNBF converts received radio wave down into about $\mathcal{O}(1\text{GHz})$.

The characteristics of the receiver are listed in Tab. 4.2.

Figure 4.5: Picture of Low Noise Block converter

Frequency	12.25 to 12.75 GHz
Local oscillation (L.O.) frequency	11.3GHz
Output frequency	950 to 1450 MHz
L.O. stability (over temperature range)	± 500 kHz
Noise figure Phase noise	0.6dB -65dBc/Hz at 1kHz -80dBc/Hz at 10kHz -100dBc/Hz at 100kHz
Input VSWR	2.2:1
Output VSWR	2.2:1
Conversion gain	64dB
Output P1dB	8dBm
Power requirements	+15 to +24 V supplied through center conductor of IF cable
Dimensions	85(L) × 43(W) × 43(H) mm
Weight	120g
Temperature range	-40°C to +60°C

Table 4.2: The specification of the Low Noise Block converter

4.2.3 Signal generator

According to the specification of the LNBF, L.O. stability is 500kHz over the temperature range (from -40°C to + 60°C). It means that the frequency of L.O. might be shifted with a change in room temperature. If room temperature is varied by 0.5°C , the frequency of L.O. might be shifted by 5kHz. This frequency shift can be fatal problem because our setting value of the 1bin RBW in searching for HPDMs is 5kHz which we explain in Chap. 6. Therefore, we used the a signal from the signal generator (2023A, Aerofrex)to calibrate the L.O. frequency (Fig. 4.6, Tab. 4.3).

According to the specification, the frequency stability of the signal generator is better than $\pm 7 \times 10^{-7}$ over the operating range of 0 to 55°C. For example, let us consider that the signal generator outputs 12 GHz as a reference signal. The frequency shift is lower than 8.4kHz over the operating range. The predicted change of the room temperature is a few °C, thus the frequency shift can be considered to be lower than 1kHz which is much smaller than the RBW for searching for HPDMs. Therefore, we used this signal generator for the calibration of L.O. frequency.

Figure 4.6: Picture of the signal generator

Carrier frequency (C.F.) range	9kHz to 1.2GHz
C.F. resolution	1Hz
C.F. accuracy (Ageing rate)	less than 1 $\times 10^{-6}$ per year
(Against temperatures)	Better than $\pm$ 7 $\times 10^{-7}$ over the operating range of 0 to 55 °C
Output level range	-140dBm to +13dBm
Level resolution	settable 0.01dB
	displayed 0.1dB
Level accuracy	±0.8dB
	Temp. coefficient ±0.02dB/°C
VSWR	Less than 1.3:1 for output levels less than -5dBm
	Less than 1.5:1 for output levels greater than -5dBm
Harmonics	Typ. better than -30dBc for RF levels up to +7dBm
	Typ. better than -25dBc for RF levels up to +13dBm
SSB phase noise	Better than -124dBc/Hz at 20kHz offset from a C.F. 470MHz
	Better than -121dBc/Hz at 20kHz offset from a C.F. 1GHz

Table 4.3: The primary specification of the signal generator.

4.2.4 Fast Fourier Transform(FFT) analyzer

After converting and amplifying, output frequency is about 1GHz. So we used the spectrum analyzer (FSV-4, Rohde & Schwarz, Fig. 4.7) whose frequency range is from 10Hz to 4GHz. Tab. 4.4 show the primary specification of the analyzer. It can calculate Fast Fourier Transformation (FFT) with 28MHz signal analysis bandwidth, and plot the signal power against the frequency.

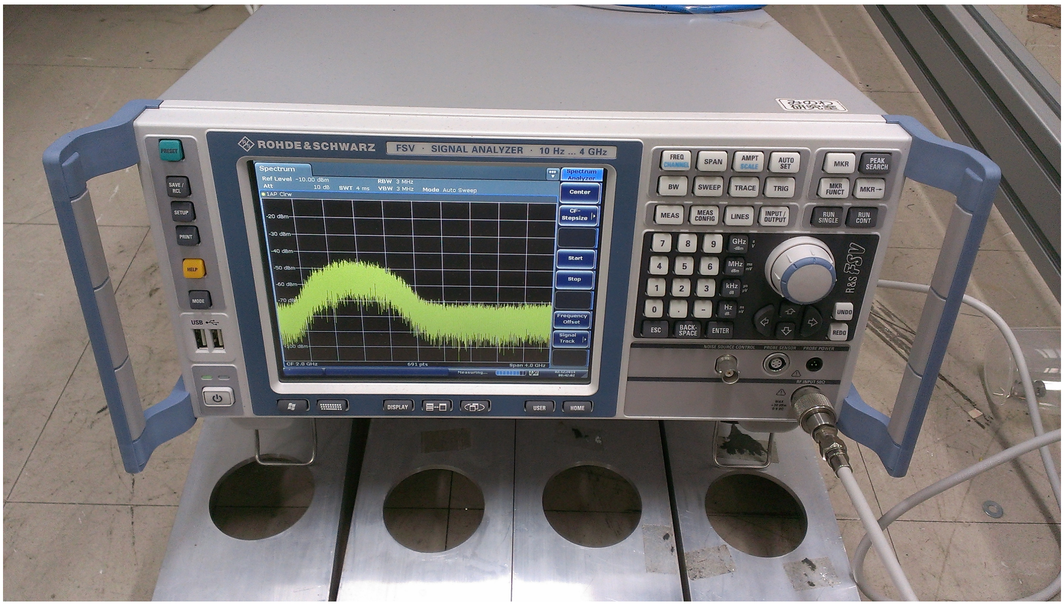

Figure 4.7: Picture of the Fast Fourier Transform analyzer

Frequency range	10 Hz to 4 GHz
Resolution bandwidth (standard sweep)	1Hz to 10MHz
Resolution bandwidth (FFT sweep)	1Hz to 300kHz
Signal analysis bandwidth	28MHz
Displayed average noise level(DANL) with 1Hz bandwidth	-150dBm, typ. -153dBm at 3GHz
Phase noise (1GHz carrier frequency)	-106dBc

Table 4.4: The primary specification of the Fast Fourier Transform analyzer.

4.2.5 Plane mirror

We used aluminum boards as plane mirror. The reasons for using the aluminum plane are as follows:

- High reflectance at $\simeq$ 12GHz.
- Thin skin depth at the frequency.

For a substance that is very conductive such as aluminum, the reflectance and the skin depth can be described by the following form;

$$P_{\mathrm{ref}} \simeq 1 - 4\sqrt{\frac{\pi f \epsilon_0}{\sigma}} \tag{4.2}$$

$$\delta \simeq \sqrt{\frac{1}{\pi \sigma f \mu}} \tag{4.3}$$

where ϵ_0 is the vacuum permittivity, f is the frequency, σ is conductivity, and μ is magnetic permeability. The frequency we observed is about 12GHz and conductivity is $\sigma \simeq 4.0 \times 10^7 \Omega^{-1}\mathrm{m}^{-1}$, therefore we obtain,

$$4\sqrt{\frac{\pi f \epsilon_0}{\sigma}} \simeq 3.7 \times 10^{-4}. \tag{4.4}$$

This represents only a small power loss of 3.7×10^{-2}%, therefore the aluminum plane acts as very good mirror at the frequency.

Next, let us consider the skin depth. The magnetic permeability of aluminum are $\mu \simeq \mu_0 = 4\pi \times 10^{-7}$H/m. Therefore, the skin depth of aluminum plane at the frequency is less than 1.0μm.

For these reasons, we can consider the aluminum plane as almost perfect mirror at this frequency. On the other hand, although the thickness of the plane is not important, we decided to use the aluminum planes which has 2mm thickness. It is in order not to be deformed, for example, when we set up it.

We decided to use the four aluminum planes whose size is 1245(H) × 1240 (W) × 2(D) mm. We installed them in parallel with one another on a same plane with about 10mm gaps as shown in Fig. 4.8

Five small holes were punched in each plane for geometrical adjustment. We explain the geometrical adjustment in Sect.6.1.

Figure 4.8: Phorograph of the plane mirror.

Chapter 5

Calibrations

5.1 The standard deviation of the power of the thermal noise of the FFT analyzer

We must know the standard deviation of the power measured by the FFT analyzer. As noted below, we can obtain the standard deviation of the power from the values of signal analysis bandwidth and the measurement time. However, it depends on the setting value of the FFT analyzer, and we have no means to know the analysis bandwidth. Therefore, in order to estimate the standard deviation, we measured the thermal noise of the FFT analyzer directly.

Let us start with explaining the standard deviation of the power of Gaussian random noise (e.g. thermal noise). In the measurement of searching for HPDMs, the black body radiation, which is also gaussian random noise, is the dominant noise source. It is well known in the field of radio astronomy that the standard deviation of the power of Gaussian random noise P with the RBW $\Delta\nu_{\mathrm{RBW}}$ and the measurement time τ is,

$$\sigma_P = \frac{P}{\sqrt{\Delta\nu_{\mathrm{RBW}}\tau}}. \tag{5.1}$$

Here, τ relates the sweep time T and the number of sweep points n as,

$$\tau = \frac{T}{n} \tag{5.2}$$

In the case of sweep type spectrum analyzer,

$$n = \frac{S}{\Delta\nu_{\mathrm{RBW}}}, \tag{5.3}$$

where S is the frequency span. On the other hand, in the case of FFT analyzer with analysis bandwidth $\Delta\nu_{\mathrm{FFT}}$ which is much broader than $\Delta\nu_{\mathrm{RBW}}$, the number of sweep points is,

$$n_{\mathrm{FFT}} = \frac{S}{\Delta\nu_{\mathrm{FFT}}}. \tag{5.4}$$

Therefore, τ increases by the factor of $\Delta\nu_{\mathrm{FFT}}/\Delta\nu_{\mathrm{RBW}}$,

$$\tau_{\mathrm{FFT}} = \frac{T}{n_{\mathrm{FFT}}}, \tag{5.5}$$

and the deviation becomes,

$$\sigma_{P_{\mathrm{FFT}}} = \frac{P}{\sqrt{\Delta\nu_{\mathrm{RBW}}\tau_{\mathrm{FFT}}}}. \tag{5.6}$$

As we explained above, we do not know $\Delta\nu_{\mathrm{FFT}}$ and, therefore, cannot evaluate $\sigma_{P_{\mathrm{FFT}}}$ with Eq. (5.4) – (5.6). Instead, we measured the thermal noise of the FFT analyzer and estimated $\sigma_{P_{\mathrm{FFT}}}/P$. Conversely, we also got $\Delta\nu_{\mathrm{FFT}}$ with these equations, i.e. in this measurement, we can obtain $\sigma_{P_{\mathrm{FFT}}}/P$ and $\Delta\nu_{\mathrm{FFT}}$.

5.1.1 Measurement

For measuring the thermal noise, we did not install the LNBF to the FFT analyzer. Thus we measured only the thermal noise of the FFT analyzer. However, we confirmed Eq. (5.6) is also valid for measurement of searching for HPDMs.

This measurement was done by the setup for searching for HPDMs (we explain this setup in the following chapter). We conducted the measurement by the same setup with the actual measurement (Tab. 5.1).

The setup value of RBW and measurement frequency range of searching for HPDMs are 5kHz and 0.6 to 1.6 GHz, respectively. Then, the number of bins is,

$$N = \frac{1\mathrm{GHz}}{5\mathrm{kHz}} = 2.0 \times 10^{5}. \tag{5.7}$$

The FFT analyzer which we used cannot measure such a large number of bins at one time. Therefore, we separated the frequency region into a plurality of partial regions and measured in order. We decided to divide the frequency range into 20 equal parts. In this way, the measurement is conducted from 0.6 to 1.6 GHz in increments of 50MHz. In this thesis, we named each 50-MHz part a “sub-sweep” and the whole set of 20 parts a “sweep”. Fig. 5.1 shows two examples of sub-sweep. At first, we measured the frequency range of 0.6-0.65 GHz and then we measured the next frequency range of 0.65-0.7GHz.

We can obtain the result of single-sweep by connecting the result of sub-sweeps. For example, Fig. 5.2 shows the result of connecting two sub-sweeps shown in Fig. 5.1.

Center frequency	from 675 MHz to 1575 MHz (in incliments of 50MHz)
Span	50MHz
RBW	5kHz
Number of bins	10001
Sweep time	3 sec.
Average type	Power
Detector mode	Average

Table 5.1: Set up of searching for HPDMs

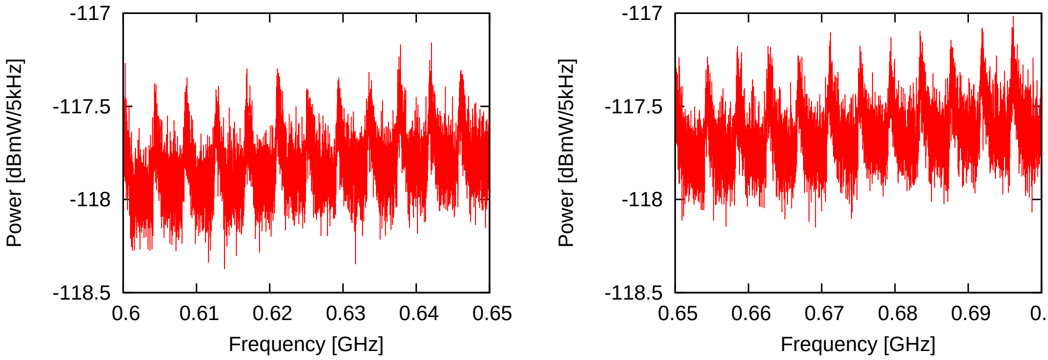

Figure 5.1: Two examples of sub-sweeps. Sweep ranges are 0.6 to 0.65 GHz and 0.65 to 0.7 GHz respectively.

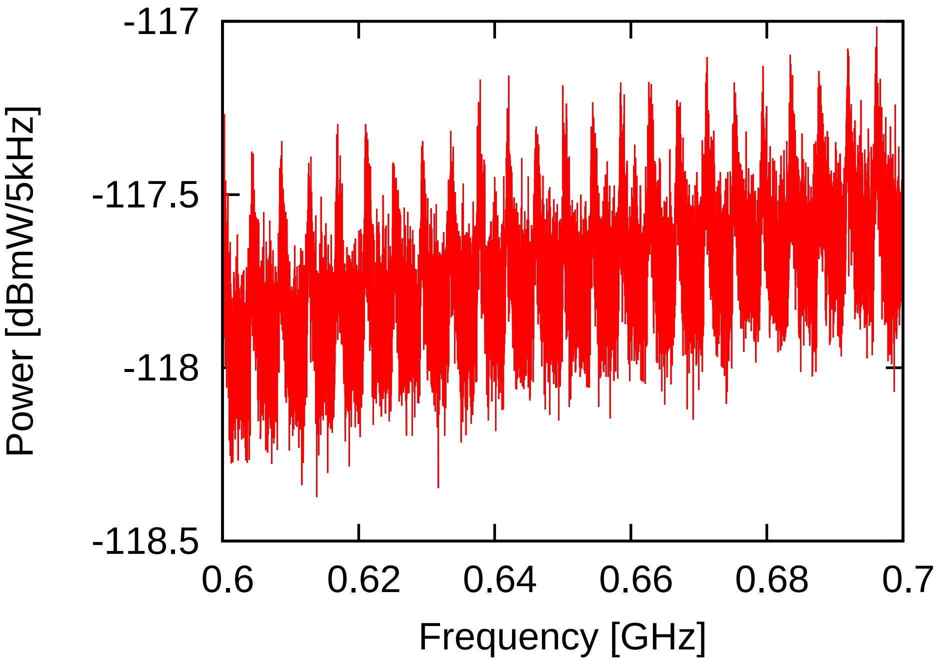

Figure 5.2: The result of connecting two sub-sweeps shown in Fig. 5.1.

The result of single sweep measurement is shown in Fig. 5.3. There are some frequency characteristics in the result. The characteristics are:

- There are discontinuities at the several connecting points of sub-sweeps.
- There is periodical structure whose period is about 4.2 MHz.

This period is supposedly related to the analysis bandwidth of the FFT analyzer (the details of this is discussed below).

5.1.2 Estimation

The deviation of the thermal noise power

In order to estimate the deviation of the thermal noise power, we selected the 1.55 to 1.6 GHz frequency sub-sweep where the power can be regarded as white noise, i.e. the power is constant in the frequency span(Fig. 5.4). Also, we performed fitting of the data of Fig. 5.4 for correcting the distortion of the baseline. We conducted the fitting by the following method;

- We fitted the quadratic functions with the least squares.
- Fitting was performed for every 50 points (250 kHz).
- The adjacent functions were formed to be continuous without a step.

The result of the fitting is shown in Fig. 5.5. After the fitting, we subtracted the fitting result from the measurement data in order to correct the baseline to be zero (Fig. 5.6). Eventually, we calculated the distribution of the power of each RBW bin around the baseline.

Next, we fitted gaussian:

$$\frac{N}{\sqrt{2\pi\sigma^2}} \exp\left(-\frac{(p-\mu)^2}{2\sigma^2}\right), \tag{5.8}$$

to the distributions, where p represents the power which corresponds to the horizontal axis of Fig. 5.7. Fitting results are shown in Tab. 5.4.

According to the result of fitting, if we conduct a single sweep with this setup, we obtain,

$$\frac{\sigma_{P_{\mathrm{FFT}}}}{P} = 2.57 \times 10^{-2}. \tag{5.9}$$

In order to calculate Eq. (5.9), we used the value $P = 1.15 \times 10^{-12}$ mW/5kHz ($\simeq -119.4$ dBmW/5kHz) which roughly corresponds to the average power before subtraction. Of course, if we conduct N times sweeps, the deviation decreases as the square root of N.

The analysis bandwidth

As described above, there are the periodical structure in the spectrum. We considered thath the cause of this structure is the analysis bandwidth $\Delta\nu_{\mathrm{FFT}}$. In order to estimate $\Delta\nu_{\mathrm{FFT}}$, we solved Eq. (5.4) for $\Delta\nu_{\mathrm{FFT}}$. Furthermore, using (5.5) and (5.6), we obtain,

$$\Delta\nu_{\mathrm{FFT}} = \left(\Delta\nu_{\mathrm{RBW}} \times \frac{T}{S}\left(\frac{\sigma_{P_{\mathrm{FFT}}}}{P}\right)^2\right)^{-1}. \tag{5.10}$$

Inserting Eq. (5.9), $\Delta\nu_{\mathrm{RBW}} = 5$ kHz , $T = 3$ sec., and $S = 50$ MHz into Eq. (5.10), we obtain,

$$\Delta\nu_{\mathrm{FFT}} = \left(\frac{5000 \text{ Hz} \times 3 \text{ sec.}}{50 \text{ MHz}} \times (2.57 \times 10^{-2})^2\right)^{-1} \simeq 5.0 \text{ MHz}. \tag{5.11}$$

It is slightly larger than 4.2 MHz. It might be due to the characteristics of the FFT analysis method. In FFT calculation, an analysis bandwidth may overlaps with neighboring analysis bandwidth making the period of structure smaller than the actual analysis bandwidth. However we have no means to know the detailed calculation method of the FFT-analyzer, and this is beyond the reach of this thesis. Even so, it is certain that the periodical structure is not derived from outside, bacause the LNBF was not installed to the FFT-analyzer.

This structure and the discontinuities at the several connecting points of sub-sweeps can be considered to have an effect on the searching for HPDMs. Therefore we must take care of this effect in the measurement of the searching for HPDMs which we explain in Chap. 6.

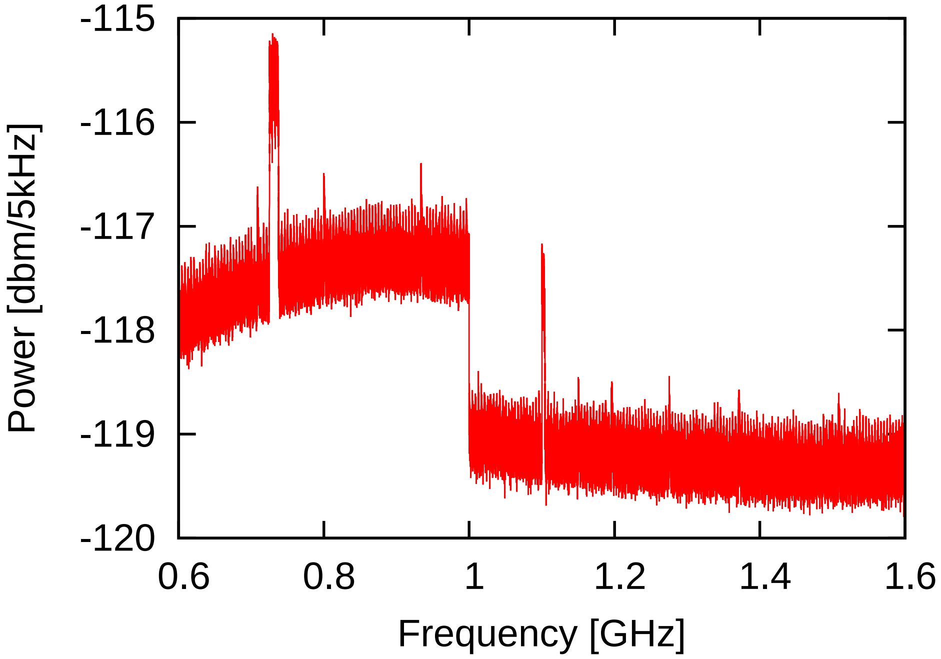

Figure 5.3: The result of single sweep measuement of thermal noise of the FFT-analyzer.

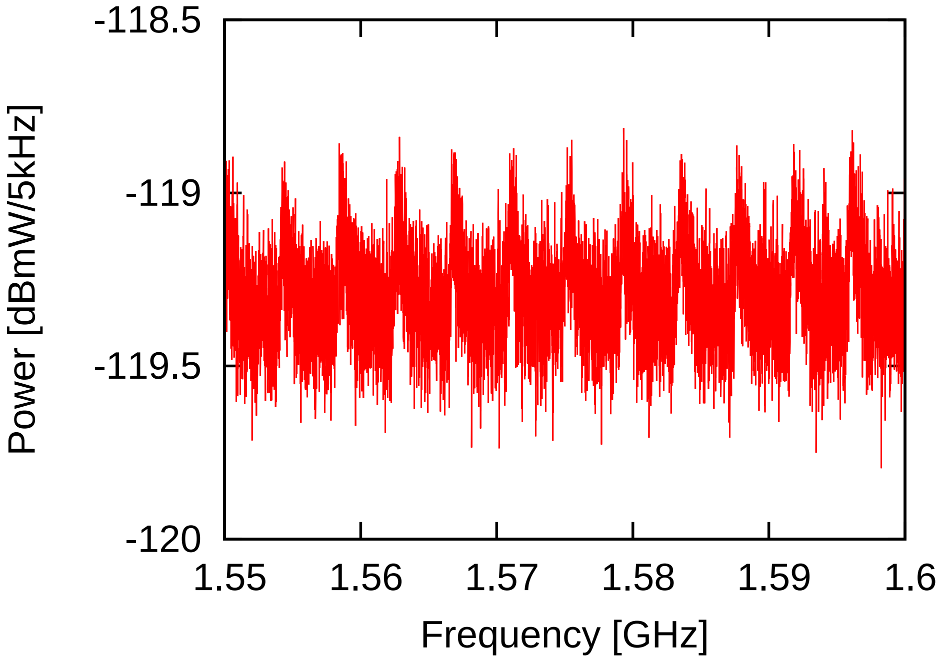

Figure 5.4: Enlarged view of the single sweep of Fig. 5.3.

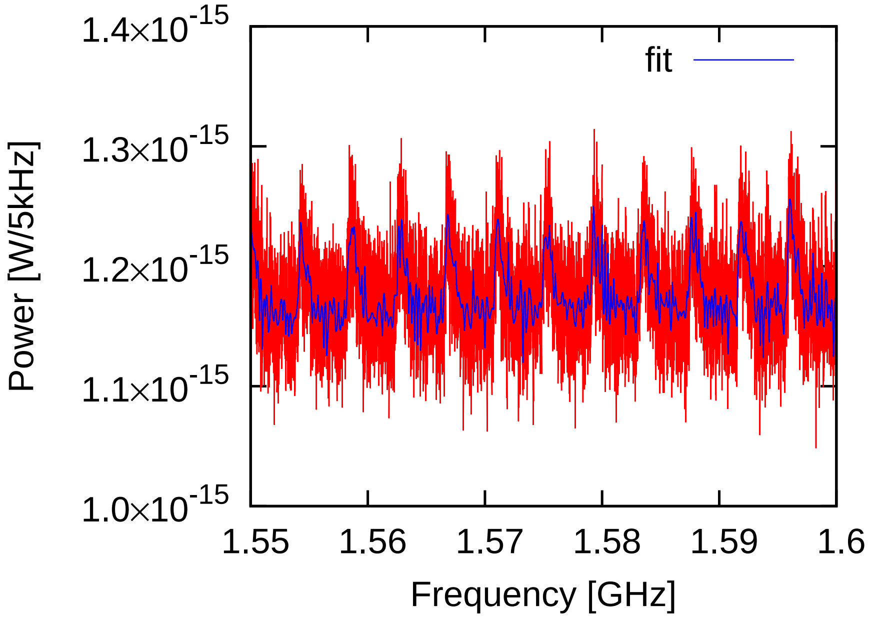

Figure 5.5: The result of fitting. The vertical axis is changed to linear scale.

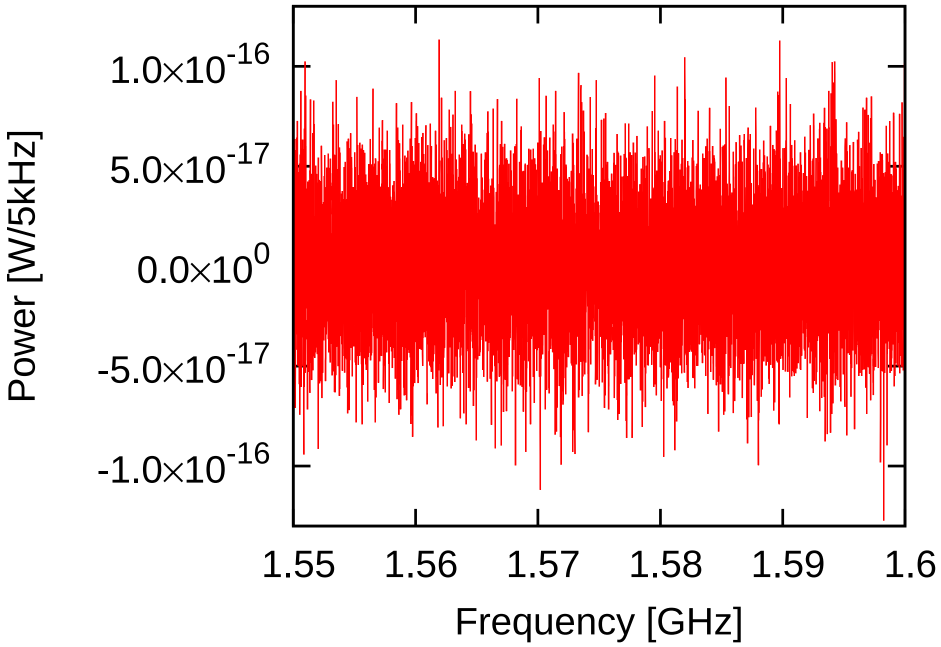

Figure 5.6: The result of subtraction between the data and the result of fitting.

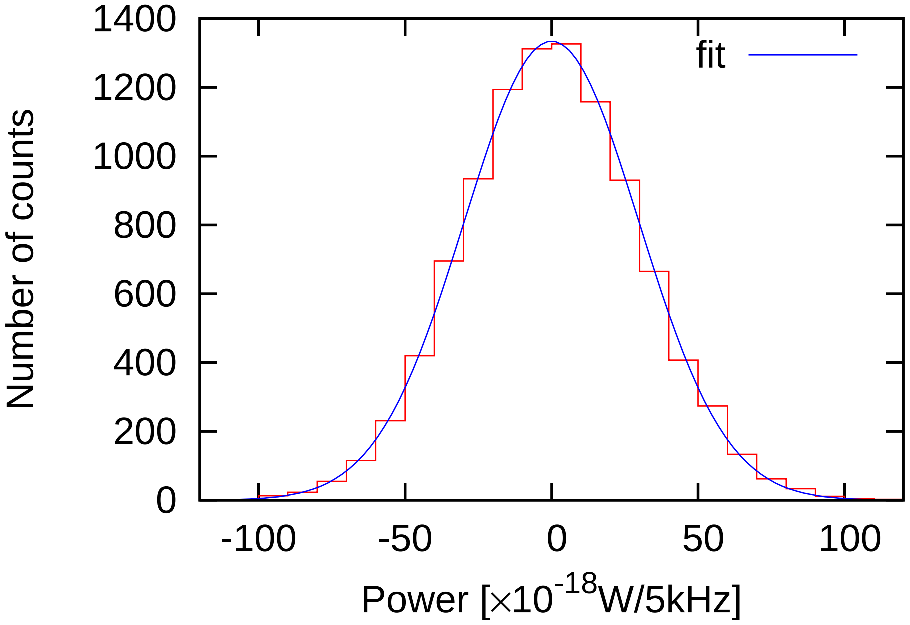

Figure 5.7: The distribution of the power of each RBW bin.

Fitting parameter	Result
N	99262.1 ± 548.2
μ	-0.374074 ± 0.1816
σ	29.5679 ± 0.207

Table 5.2: The result values of fitting parameters.

5.2 Gain of the receiver

In the receiver calibration process, we use a black absorber as a noise source. As shown in the appendix A, the total input power to the receiver with frequency band width $\Delta\nu$ is,

$$P_{\mathrm{NS}} = k_{\mathrm{B}} T_{\mathrm{abs}} \Delta\nu, \tag{5.12}$$

where, k_{B} is boltzmann constant, T_{abs} is temperature of the absorber. Note that this equation is valid only in the situation that the absorber covers the entire visual field of the receiver.

Furthermore, the output of the receiver gets additional noise at the time of the amplification. If we define the noise temperature as,

$$T_{\mathrm{sys}} \equiv \frac{N_{\mathrm{sys}}}{k_{\mathrm{B}} \Delta\nu} \tag{5.13}$$

where $N_{\rm sys}$ is the additional noise. Then, total output power is,

$$P = k_{\rm B}(T_{\rm abs} + T_{\rm sys})G\Delta\nu \tag{5.14}$$

where, G is gain of the receiver. To calibrate the gain of receiver, it is important to measure the output power with different input noise temperature. For this reason, we measured the absorber at room temperature $T_{\rm RT}(\simeq 300{\rm K})$ and at liquid nitrogen temperature $T_{\rm LN}(\simeq 77{\rm K})$.

$$\left\{ \begin{array}{l} P_{T_{\rm RT}} = k_{\rm B}(T_{\rm RT} + T_{\rm sys})G\Delta\nu \\ P_{T_{\rm LN}} = k_{\rm B}(T_{\rm LN} + T_{\rm sys})G\Delta\nu \end{array} \right\} \tag{5.15}$$

Taking difference of these powers, we get

$$P_{T_{\rm RT}} - P_{T_{\rm LN}} = k_{\rm B}(T_{\rm RT} - T_{\rm LN})G\Delta\nu, \tag{5.16}$$

then we can get gain of the receiver. Fig. 5.8 shows an absorber called "Eccosorb" (AN-73, E & C engineering) which we used for calibration. Reflectance of the absorber at around 12GHz region is about -22dB, i.e. we can regard the absorber as almost completely black body at this region.

In this calibration measurement, we set the receiver not only at room temperature, but also in a cooled and heated environment. We conducted the measurement of searching for HPDMs at room temperature. However, the room temperature was easily conceivable to vary over time. Therefore, the gain of the receiver might be changed by the time varying of the temperature. In order to solve the problem, we calibrate at several different temperature conditions and we decided to use the worst gain values for conservative estimation.

We used cement resistors for heating and a starling refrigerator for cooling (Fig.5.9). The receiver was fixed in a Styrofoam box, and a fan stirs air heated (or cooled) by the device (Fig. 5.10 and Fig. 5.11). In these measurements, we set the value of RBW to be 10 kHz. This is different from the value of 5kHz which we used for searching for HPDMs. Therefore, these measurements did not mean the gain calibration, but we can decide the temperature, which we use for the gain calibration by comparing the result of these measurements, i.e. we must conduct additional measurement for the gain calibration.

On the other hand, in order to satisfy the Eq. (5.12), we must cover the whole viewing field of the receiver with eccosorb. The dish of the antenna has 2200 mm diameter, and 770 mm focal length, so the receiver is required to have the viewing field as shown in Fig. 5.12.

The measurement has been done at 37 mm of the distance from the eccosorb. We estimated the attenuation by the wall of the Styrofoam box and found it is negligible [26]. According to Fig. 5.12, the diameter of the eccosorb was required to be larger than 220 mm diameter, thus we used the square eccosorb which has a side length of about 300 mm.

The measurements have been done by changing the temperature of the receiver from 20 to 40 °C in increments of 10 °C. Fig. 5.14 and 5.15 shows the result of power-versus-frequency spectrum, and we calculated the gain of the receiver by Eq. (5.16). Since the gain got worse when the temperature of the receiver became higher, we conducted the calibration measurement at 40 °C with the setup of the FFT analyzer for searching for the HPDMs. The number of sweeps was five for both of the measurements of the eccosorb at room temperature [1] and at liquid nitrogen temperature. The result of the calibration is shown in Fig. 5.16.

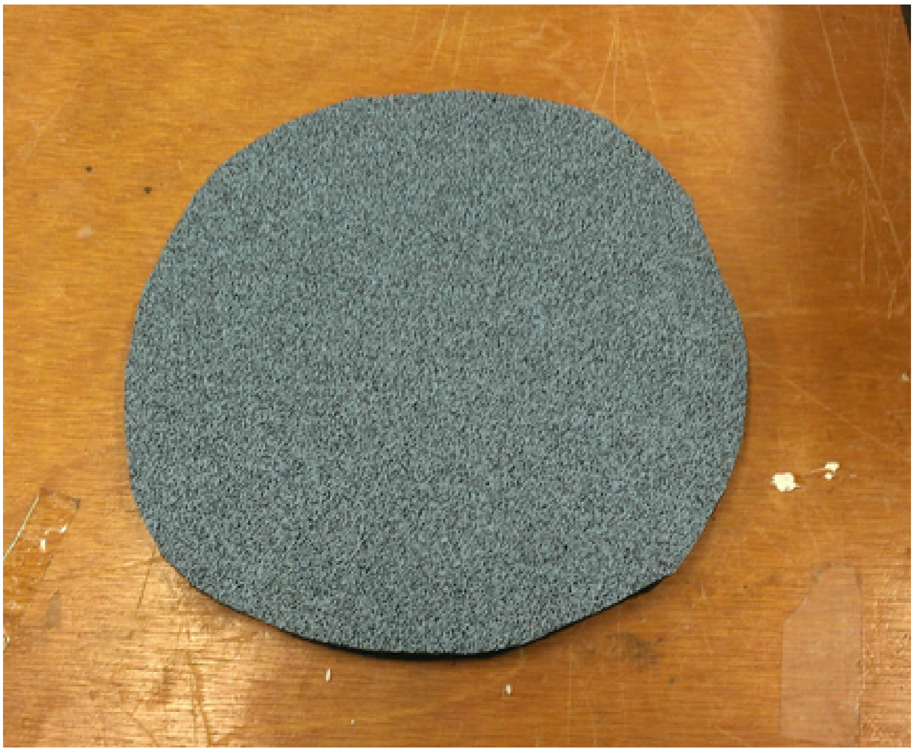

Figure 5.8: Eccosorb

---

[1] The room temperature was about 25°C when we conducted the measurements.

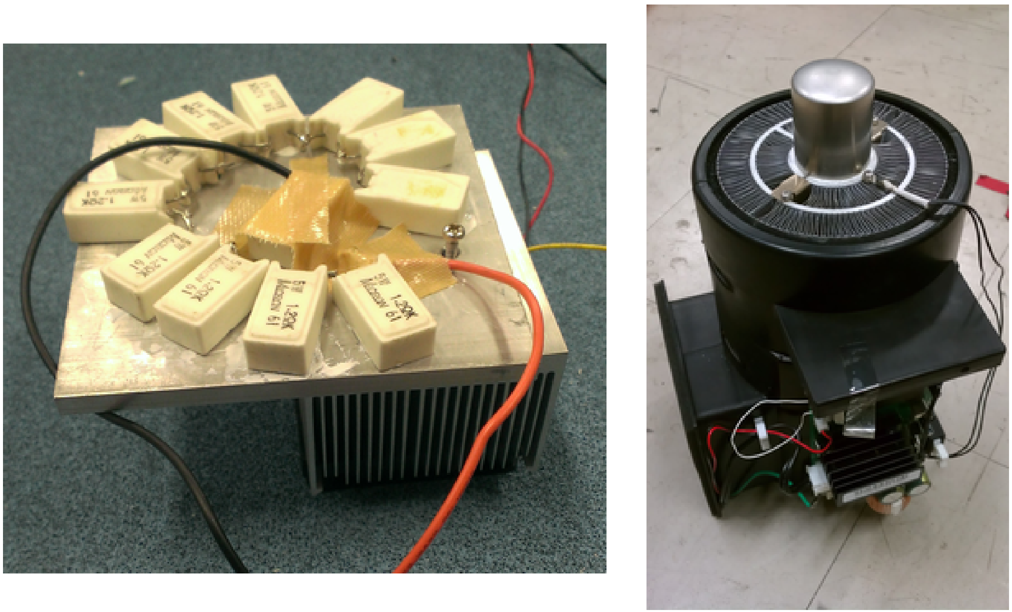

Figure 5.9: The devices for temperature control. The left one is cement resistor for heating and the right one is starling refrigerator for cooling.

Figure 5.10: The receiver fixed in the Styrofoam box.

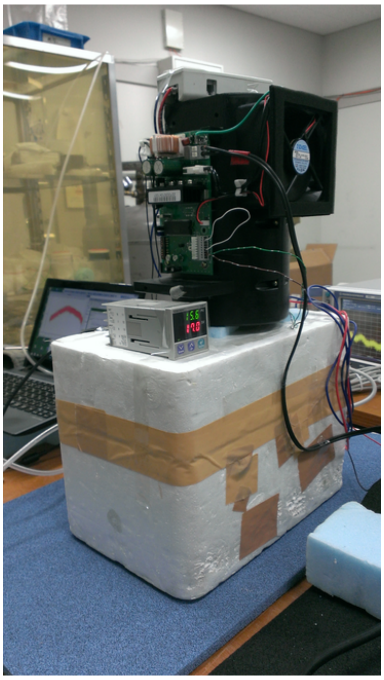

Figure 5.11: Set up of the measurement. The photograph shows the measurement with starling refrigerator. The temperature of the receiver is controlled at 20 °C.

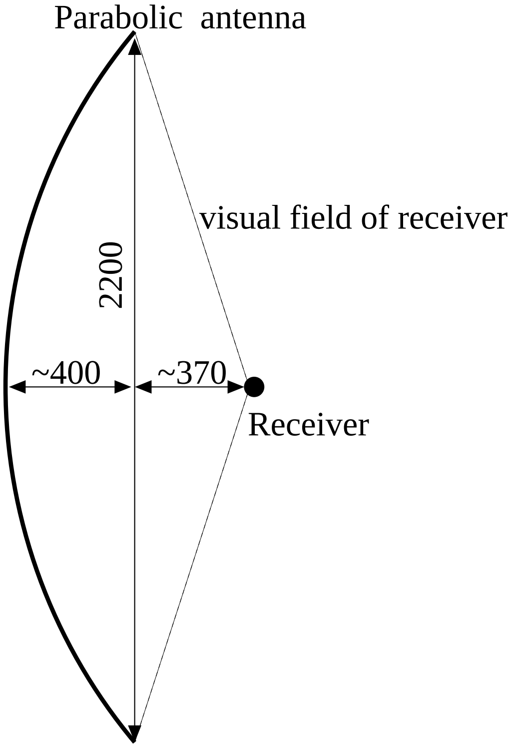

Figure 5.12: Schematic view of the visual field of the receiver.

Figure 5.13: Photograph of the measurement for eccosorb at LN temperature.

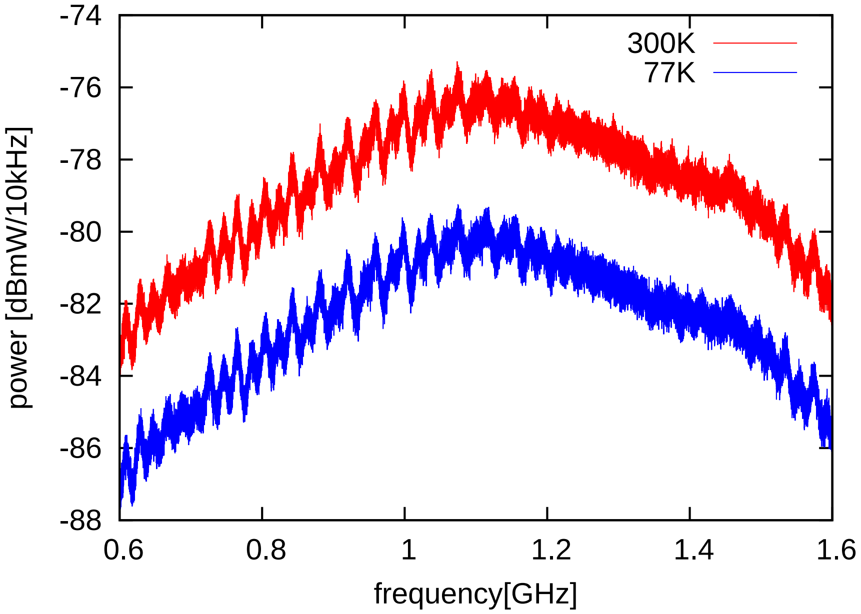

Figure 5.14: The measurement result of black body radiation at RT(about 300K) and LN temperature (about 77K) when the temperature of the receiver was 20 °C.

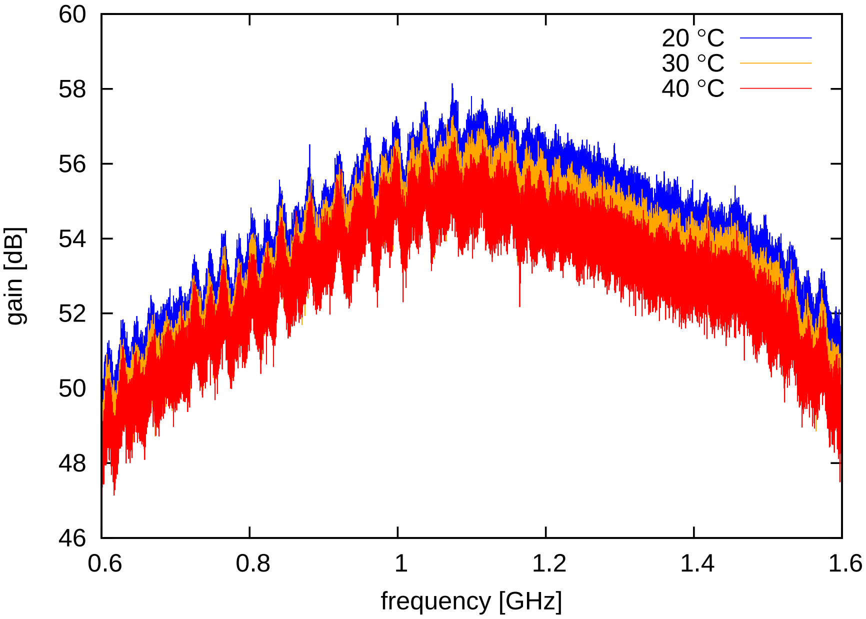

Figure 5.15: The comparison of gain in three temperature environment of the receiver.

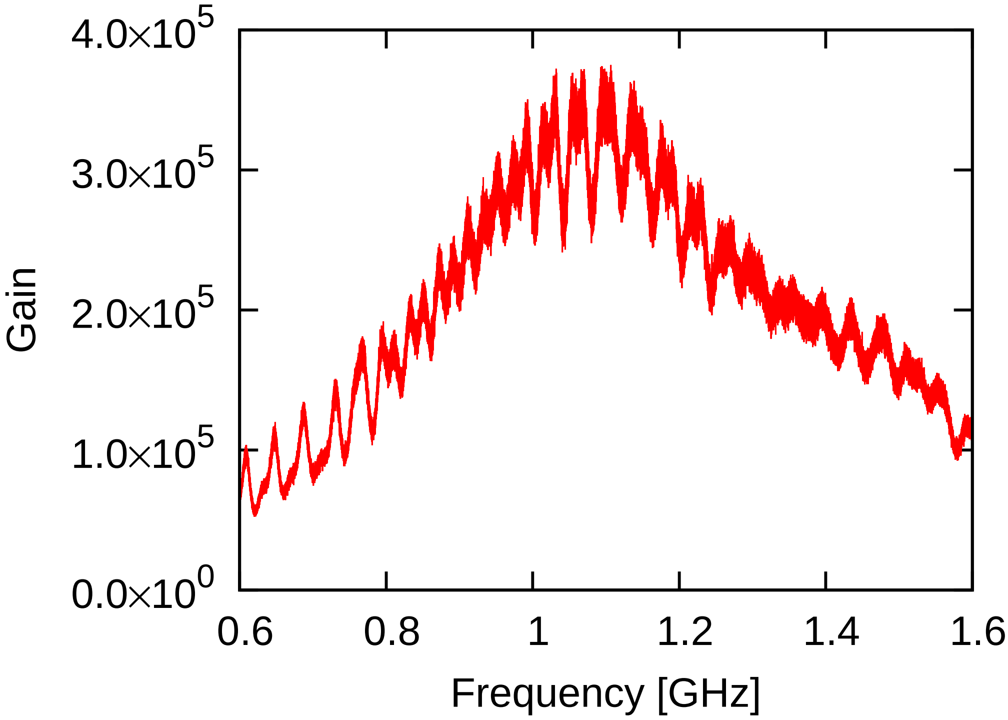

Figure 5.16: The result of calibration of gain of the receiver.

5.3 About the dish of parabolic antenna

For the parabolic antenna, gain calibration of the dish and measurement of power pattern versus angle of input are required. Even if the shape of a dish of parabolic antenna is completely paraboloidal surface, it cannot collect electromagnetic wave perfectly when angle between the axis of parabolic antenna and the direction of the wave is not aligned. And to make matter worse, there is no parabolic antenna which has completely paraboloidal surface. In fact, there are some phase error caused by the fabrication tolerances of the mirror. The gain of the dish of the antenna got worse by the inaccuracy of the direction and the deformation of the dish. It means that the area of the dish become effectively smaller by these reasons.

In order to estimate the gain and its angle dependence, we observed satellite broadcasting (BS/CS). For setting the antenna toward the direction of a satellite, we used the angle adjusting screw which connect the antenna and the king post(Fig. 5.17 and Fig. 5.18).

Figure 5.17: The adjustment mechanism for elevation angle.

Figure 5.18: The adjustment mechanism for azimuth angle.

5.3.1 Location and assumption

At first, we chose the rooftop of the science building#1, the University of Tokyo for the location of the measurement. The rooftop is surrounded by walls and there is a sunshade above a door. So we set the antenna carefully so that the signal from the satellite are not hidden by the walls and the sunshade(Fig. 5.19, 5.20). The satellite, which we focused on is N-SAT-110 whose orbit position is at longitude 110 degrees east. In Tokyo, Japan, the satellite can be seen in the direction whose elevation angle and azimuth angle from the true north are 38.0° and 224.4° respectively. The shadowed area was calculated on the basis of the information about the direction of the satellite. Fig. 5.20 shows the overview of our measurement location , the direction of the satellite, and shadow of the signals from the satellite caused by the walls and the sunshade.

We assumed any attenuation caused by the atmosphere is negligible. And we adjusted the azimuth angle to maximize the signal power by looking at the FFT analyzer. In this way, there is a risk to underestimate the gain. From the point of view to search for HPDMs, however, the assumption The assumption makes the estimation only conservative, and therefore, we decided to take this way.

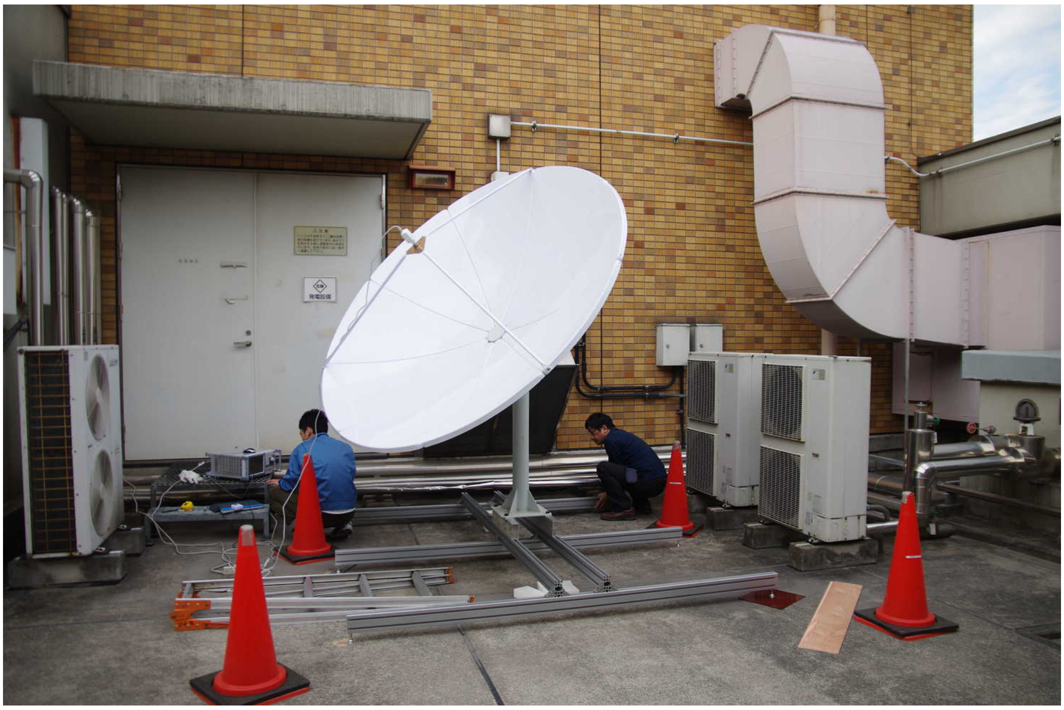

Figure 5.19: The parabolic antenna at the rooftop

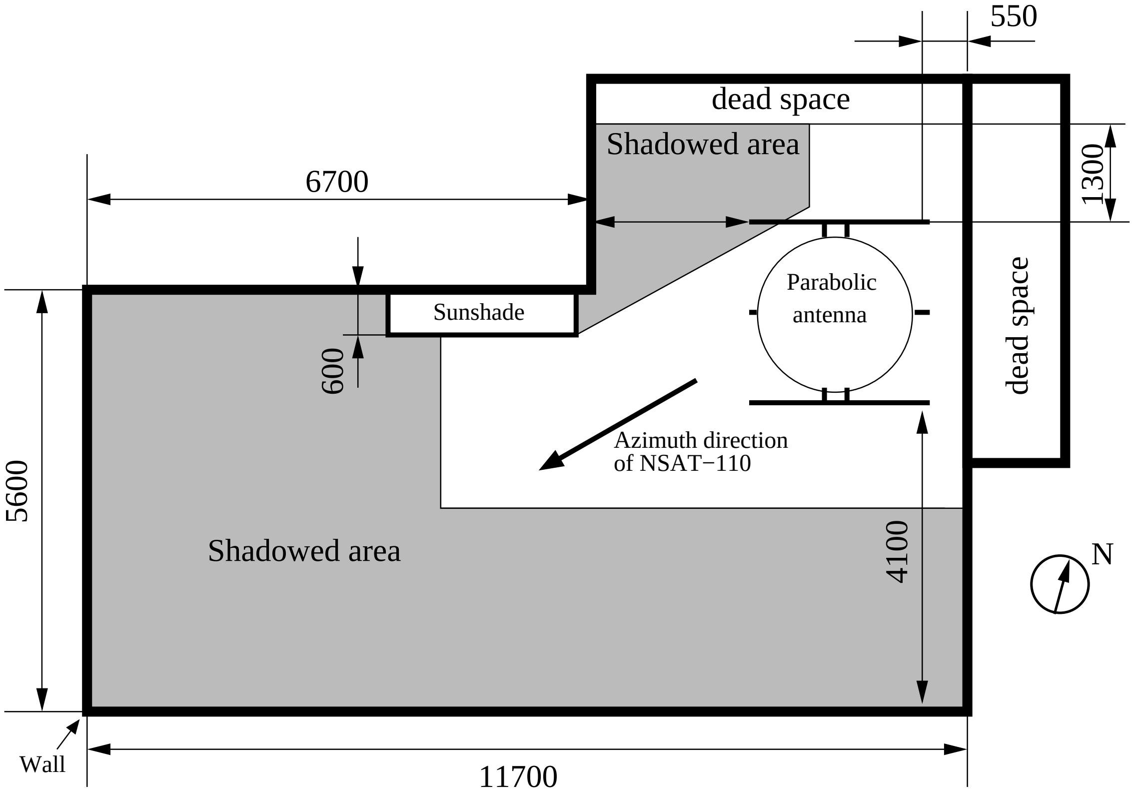

Figure 5.20: Schematic overhead view of the rooftop.

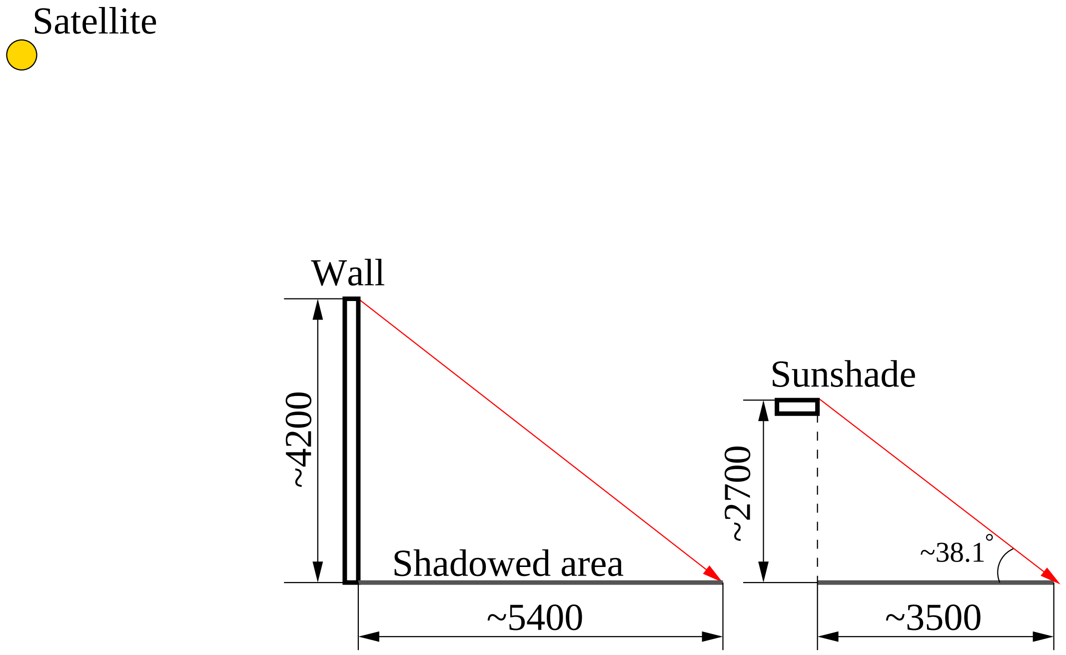

Figure 5.21: Schematic view of the satellite shadowed area.

5.3.2 Estimation of the standard deviation

We estimated the standard deviation of the power from the satellite in the similar manner as discussed in Sect. 5.1.

- We did not install the LNBF to the FFT-analyzer (Fig. 5.22)
- The setup value of the FFT-analyzer was same as the setup of the satellite measurement(Tab. 5.3)
- We selected the frequency span of 1.2 to 1.75GHz which can be regarded as white noise (Fig. 5.23)
- we calculated the distribution of the power of each RBW bin around the baseline (Fig. 5.24, Tab. 5.4)

Note that, there is not periodical structure discussed in Sect. 5.1, but there is the step structure which arises in Fig. 5.22. Although we did not find out the reason of the step structure, this can be considered not to affect the spectrum of the signal power from the satellite because the power is much larger than the thermal noise of the FFT-analyzer.

As the result, we obtain;

$$\frac{\sigma_{P_{\mathrm{FFT}}}}{P} = 7.93 \times 10^{-2}. \tag{5.17}$$

Center frequency	1GHz
Span	1.5GHz
RBW	1MHz
Sweep point	1501
RF attenuation	20dB
Sweep time	1.51msec
Detector mode	Average
Trace mode	Average
Average type	Power
Number of sweeps	100

Table 5.3: Set up of the satellite measurement.

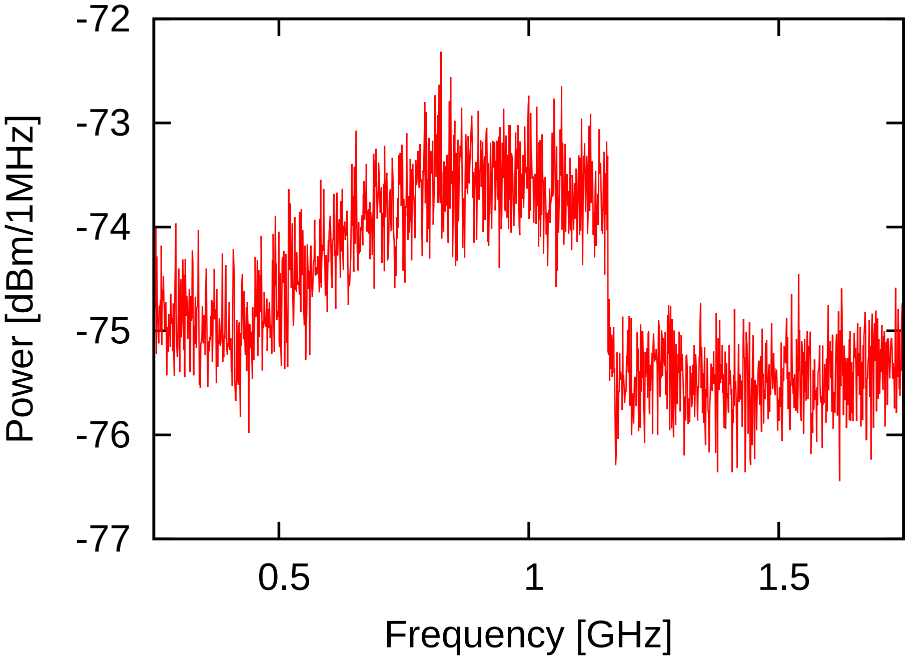

Figure 5.22: The result of single sweep measurement of the thermal noise of the FFT-analyzer.

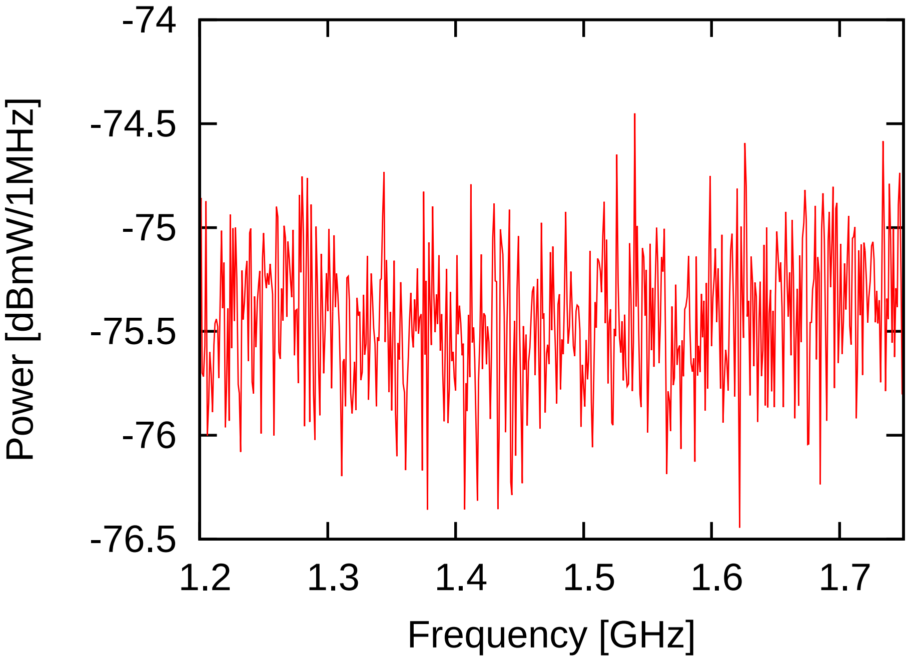

Figure 5.23: Enlarged view of Fig. 5.22.

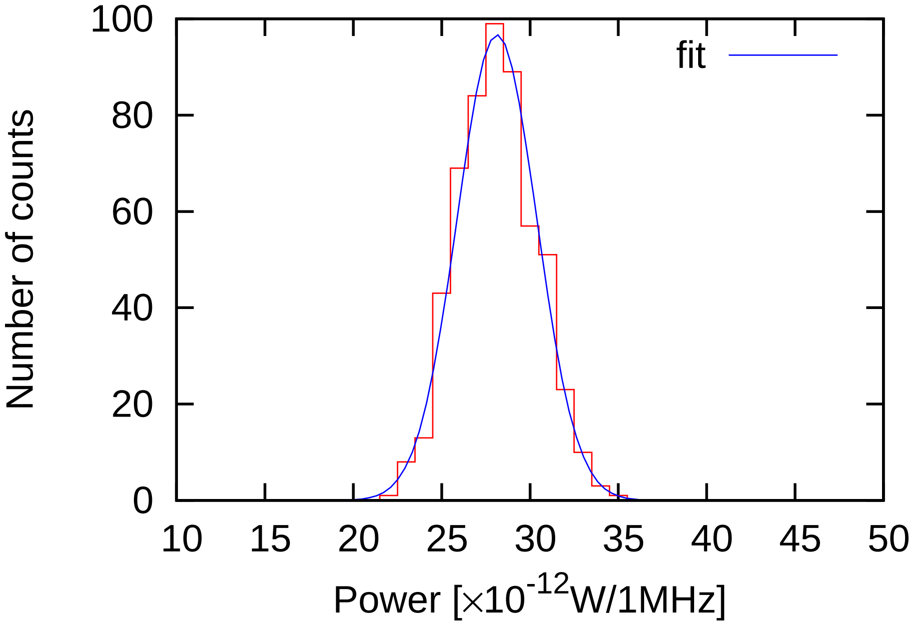

Figure 5.24: The distribution of the power of each RBW bin.

Fitting parameter	Result
N	545.462±24.49
μ	28.1274 ± 0.1088
σ	2.2317 ± 0.09635

Table 5.4: The result values of fitting parameters.

5.3.3 Result

After adjustment of azimuth angle as mentioned above, we also adjusted elevation angle in the same way. For elevation angle, however, the angle dependence of the dish gain was measured. So we varied the elevation angle from the point of the gain maximum (about 38°). Here we assumed the power pattern which centered on the maximum is rotationally symmetric, because a parabolic antenna has a rotational symmetry, thus we did not vary the azimuth angle.

We measured the elevation angle with level meter called "bevel box" (BB-180A, Niigata Seiki, Fig. 5.25). We equipped the back of parabolic antenna with the bevel box and we varied the elevation angle in increments of 0.1 degrees. The result of the measurement at several elevation angles is shown Fig.5.26. The several peaks of the power represent signal from the plurality of the transponders. Several programs belonging to the same category are transmitted by grouping them together in a single transmission channel at each transponder of the satellite. We numbered the serial number to the peaks from TP-1 to TP-12 in order of frequency increasing.

For calculating of the dish gain, let us begin by considering signal propagation from the satellite, and concentration of the signal. The signal emitted from a certain transponder of NSAT-110 satellite (P_{TP}) is attenuated by propagation broadening (Ls). After that, the signal has been collected by the parabolic antenna whose gain is G_{d}, so we get the power entering to the receiver,

$$P_{\mathrm{input}} = \frac{P_{\mathrm{TP}}}{2} \times Ls \times G_{\mathrm{d}}, \tag{5.18}$$

where the factor $\frac{1}{2}$ arises from following reason. Our converter has a sensitivity for linearly polarized wave, but the signal from the satellite is circularly polarized wave which is composed of a combination of two vertically-aligned linearly polarized waves. Since the converter can receive only one component of linearly polarized wave, the input power is half of the total.

As shown in Appendix B, the degree of attenuation of the signal power can be calculated by,

$$Ls = \left(\frac{\lambda}{4\pi d}\right)^2, \tag{5.19}$$

where d is the distance between the satellite and the measurement location, and λ is observation wavelength. The distances between Tokyo and the satellite is 37,930 km, so Ls can be calculated to be -205.8 dB for the wave of 12.3 GHz frequency.

For getting P_{TP}, we contacted the "SKY Perfect JSAT Corporation" which operates the satellite (NSAT-110). According to their response, The equivalent isotropic radiated power (EIRP) at Tokyo is 58dBW, and the fluctuation of EIRP is less than ± 1dB. For conservative estimation (to estimate the gain worse than real value), we decided to use 59dBW as P_{TP}.

According to Eq. (5.18), in order to estimate the dish gain, P_{input} is required. We used the result of the measurement for the satellite in order to calculate P_{input}. For example, we explain about the result of measurement at elevation angle of 37.7° shown in Fig. 5.26. We divided this power by the gain of the receiver which is discussed in Sect. 5.2 (Fig. 5.27). This means the power before amplification by the receiver, i.e. the power of the radio wave entering to the receiver. In order to estimate P_{input}, we summed the power of each sweep point (p_{SP}) for whole frequency band of a transponder. For TP2, for example:

$$P_{\mathrm{input}} = \sum_{\mathrm{TP2}} p_{\mathrm{SP}}. \tag{5.20}$$

Since each p_{SP} has the error which can be estimated from Eq. (5.17). The error of P_{input} can be calculated as,

$$\sigma_{P_{\text{input}}} = \sqrt{\sum_{\text{TP2}} \sigma^2_{p_{\text{SP}}}}. \tag{5.21}$$

We conducted these calculation for the result of measurement at each elevation angle. In order to estimate the gain of the dish and its error, we inserted the calculation result of P_{input} and $\sigma_{P_{\text{input}}}$, $Ls = -205.8$ dB (for 12.3 GHz frequency of TP2), and P_{TP} into the Eq. (5.18). Thus we obtain,

$$G_{\text{d}} = 2 \times 10^{20.58-5.9} \times P_{\text{input}}, \tag{5.22}$$

$$\sigma_{G_{\text{d}}} = 2 \times 10^{20.58-5.9} \times \sigma_{P_{\text{input}}}. \tag{5.23}$$

Fig. 5.28 shows the result of calculations. We fitted following gaussian function,

$$\frac{N}{\sqrt{2\pi\sigma^2}} \exp\left(-\frac{(\theta-\mu)^2}{2\sigma^2}\right), \tag{5.24}$$

to the result, where θ represents elevation angle. The result values of fitting parameters are shown in Tab. 5.5. The maximal dish gain G_{d} is $3.94 \times 10^4 \pm 1000$ (45.9 ± 0.1 dB) at $\theta = \mu$, and "-3dB beam width" is 0.9°. The obtained gain and the beam width are slightly lower and broader than the specification values in Table 4.1. The relation between the dish gain and the effective area of the dish is, as described in appendix B,

$$A_{\text{e}} = \frac{\lambda^2}{4\pi} G_{\text{d}}, \tag{5.25}$$

where $G_{\text{d}} = 3.94 \times 10^4 \pm 1000$. We decide to use the 2σ smaller value, i.e. $G_{\text{d}} = 3.74 \times 10^4$, thus we obtain,

$$A_{\text{e}} = \frac{(24.4 \times 10^{-3}\text{m})^2}{4\pi} \times 3.84 \times 10^4 \simeq 1.77 \ \ [\text{m}^2]. \tag{5.26}$$

Therefore, we evaluated the effective area of the dish to be 1.77 m^2. Note that, we can obtain this value when we precisely orient the parabolic antenna toward the satellite, but if the direction is inaccurate, the effective area becomes smaller depending of the angular dependence shown in Fig. 5.28.

Figure 5.25: Photograph of bevel box.

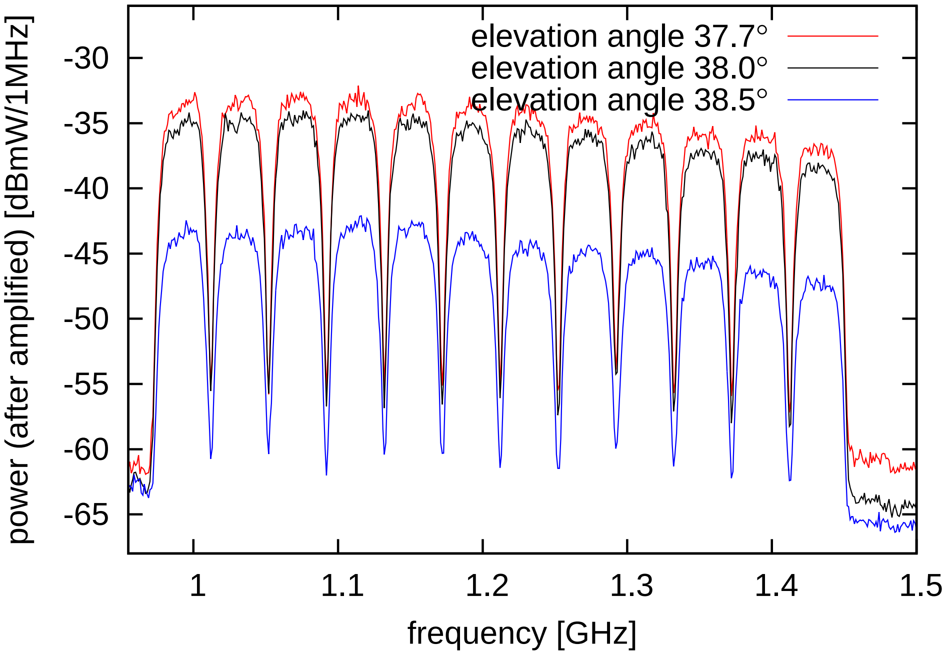

Figure 5.26: The result of the measurement at several elevation angles. The vertical axis represents the power output from the receiver.

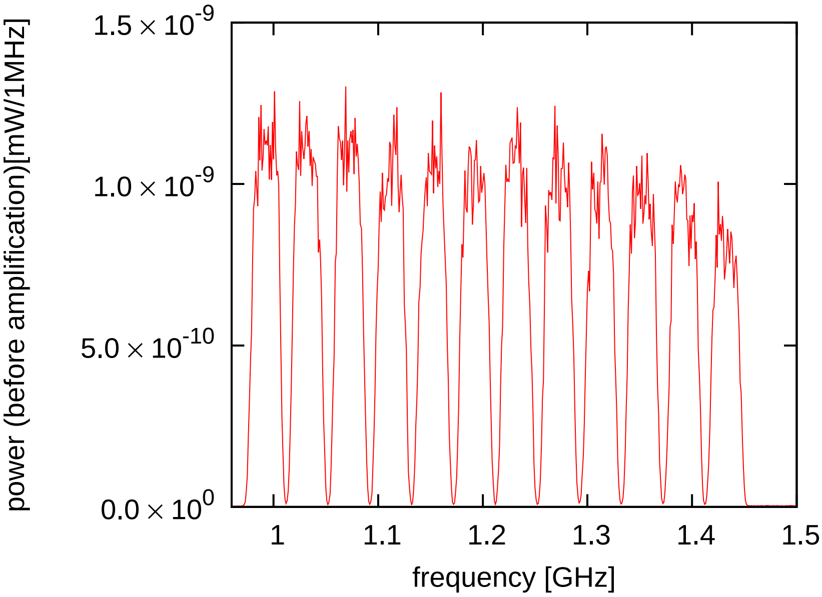

Figure 5.27: The power before amplification. The vertical axis represents the input power p_{SP}.

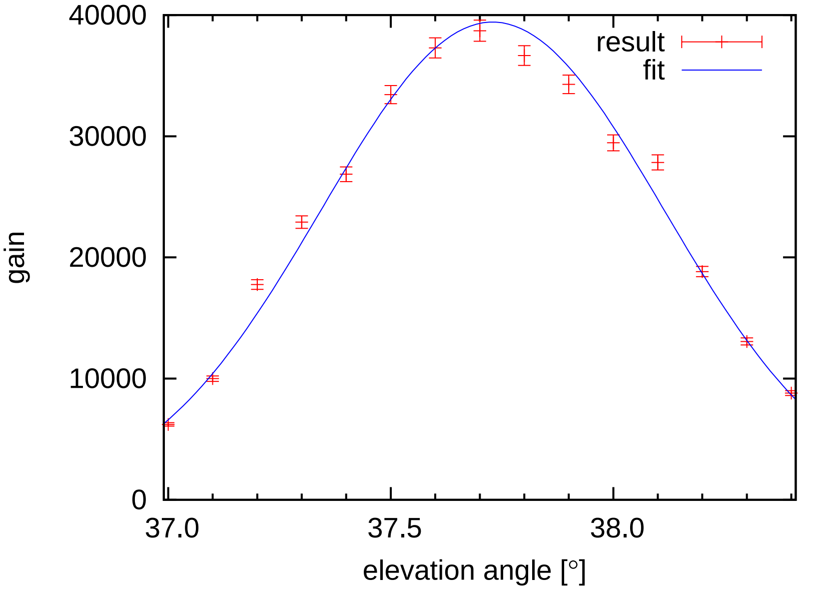

Figure 5.28: Angular dependence of dish gain

Fitting parameter	result
N	38091.4 ± 692.1
μ	37.7288 ± 0.007275
σ	0.38547 ± 0.006774

Table 5.5: The result values of fitting parameters.

Chapter 6

Measurement

6.1 Geometric adjustment

The aluminum plane was used to emit the photons derived from HPDMs as plane waves. This allows the parabolic antenna to collect the photons.

However, the aluminum plane is not perfectly flat. The phase error caused by the incompleteness of the plane affects the sensitivity for HPDMs to be worse. However, a phase error that varies linearly along some direction across the plane can be treated as tilt. Eventually, only the phase error caused by the fabrication tolerances of the plane affects the gain.

If the plane has some tolerance ϵ, this will cause a phase error,

$$\delta = 2\pi\frac{\epsilon}{\lambda} \tag{6.1}$$

where λ is the observation wavelength. In the field of radio astronomy, the effect of tolerance is well computed by Ruze [21] [22]. He calculated the effect of phase error when it follows a Gaussian distribution where its mean is zero and standard deviation is σ_δ;

$$P_{\text{eff}} = P_0 \exp(-\sigma_\delta^2) \tag{6.2}$$

where P_0 is the total power that we can obtain if the tolerance is zero. In this case the deviation of phase error is,

$$\sigma_\delta = 2\pi\frac{\sigma_\epsilon}{\lambda}, \tag{6.3}$$

where σ_ϵ is the deviation of tolerances assuming that it follows a Gaussian distribution whose meen is zero. If the tolerance is greater than $\frac{1}{10}$ of the wavelength, the signal power is extremely attenuated (shown in the Fig. 6.1). Since the wavelength which we focused on is about 25 mm, it is necessary for our experiment to adjust the distortion of the planes to be less than about 2mm.

On the other hand, we used four aluminum planes as already discussed in Sec. 4.2. Therefore, we must make an adjustment of the planes to be aligned in the same plane.

Additionally, the planes are required to be perpendicular to the symmetrical axis of parabolic antenna with extreme accuracy. In this section, we describe the geometrical adjustment of the planes, and the adjustment of relative positions of the planes and the parabolic antenna, respectively.

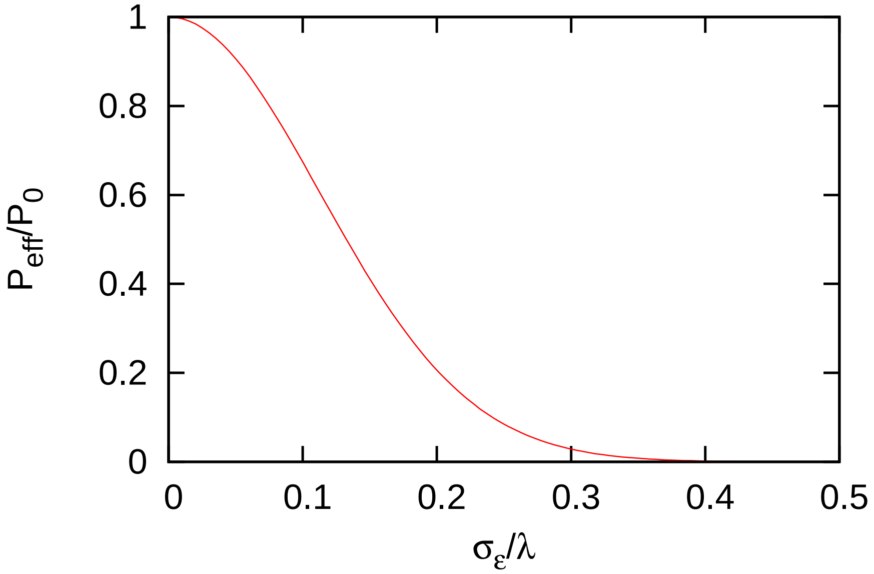

Figure 6.1: Degrees of power attenuation versus torelance.

6.1.1 Adjustment of the aluminum planes

In order to adjust geometry of the aluminum plane, we set the springs together with screws between five holes of each plane and the aluminum frame. (Fig. 6.2) We adjusted the geometry by applying moderate force to the springs.

After adjustment, we measured the space coordinates of the planes by triangulation using a theodolite (SOKKIA SLT-20, Fig. 6.3). Fig. 6.4 shows how to measure the space cordinates of the planes.

The result of measurement and the plane fitted by least squares are shown in Fig. 6.5. We obtained the degrees of irregularity of the planes by subtracting the space coordinates. The distribution of the degrees of irregularity is shown in Fig. 6.6

This result denotes that all planes are in the same plane, and the irregularity of the plane is ±1 mm at the maximum. The minimum value of the observation wavelength is about 23.3 mm corresponding to the frequency of 12.9 GHz. From the measurement result, we decide conservatively that the deviation of the irregularity is 1mm. Inserting the values of $\lambda = 23.3$ mm and $\sigma_\epsilon = 1$ mm into Eq. (6.2), we obtain,

$$\frac{P_{\text{eff}}}{P_0} \simeq 0.930. \tag{6.4}$$

Therefore, the degrees of the decreasing power caused by the irregularity of the plane mirror is 93.0%

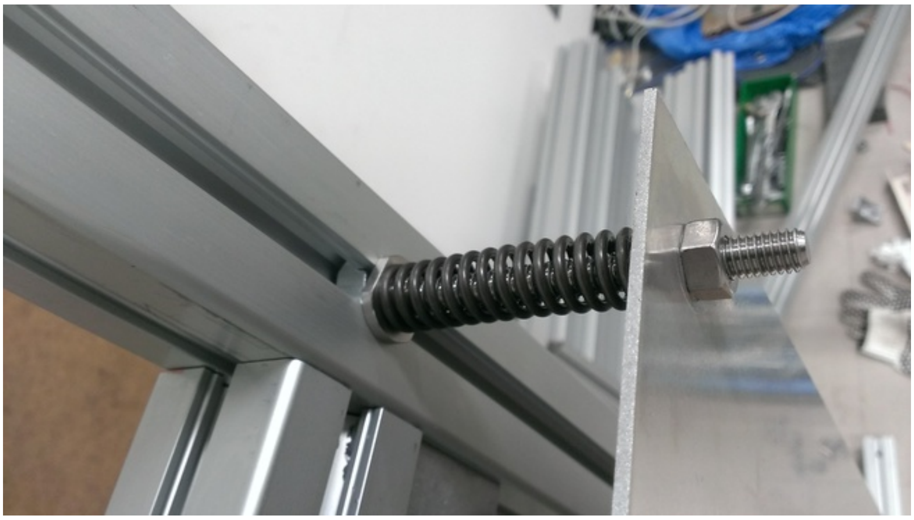

Figure 6.2: Spring

Figure 6.3: Photograph of SLT20. It was used for triangulation.

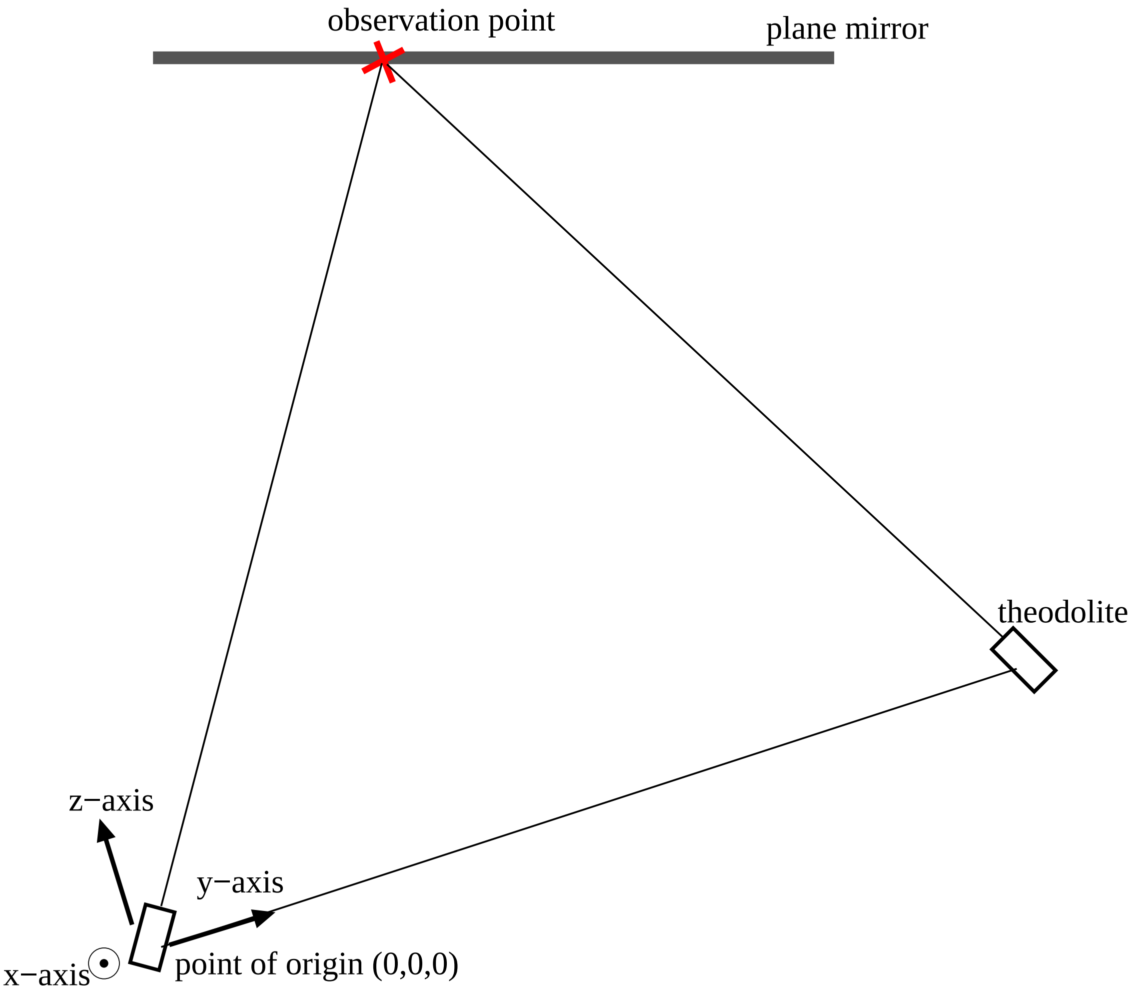

Figure 6.4: Schematic overhead view of the triangulation.

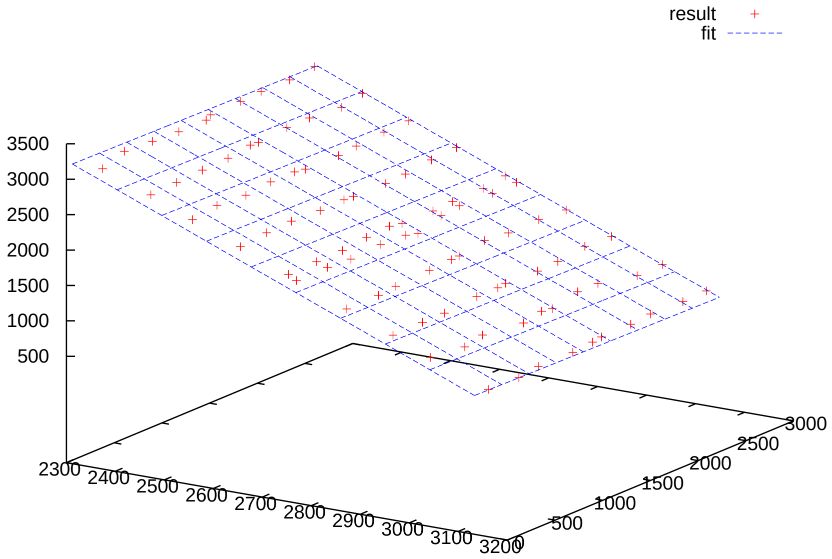

Figure 6.5: The result of the triangulation measurement and the best fit plane

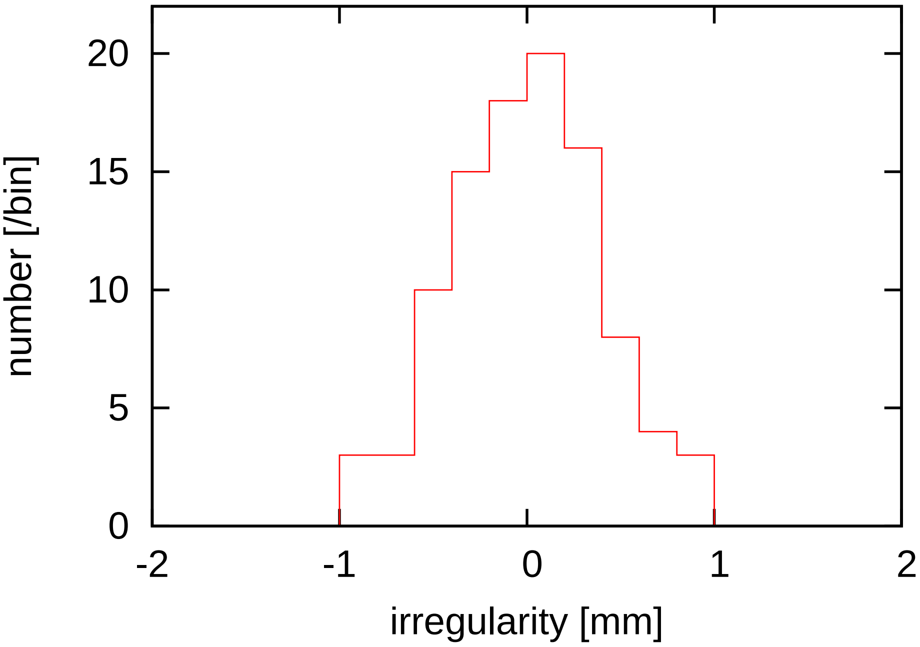

Figure 6.6: The distribution of the degrees of irregularity.

6.1.2 Adjustment of relative positions of the aluminum planes and the parabolic antenna

After adjusting the aluminum planes, we installed the parabolic antenna (Fig. 6.7). When we install the antenna, the geometric alignment is required so that the symmetrical axis of the antenna is perpendicularly crossed the planes with accuracy.

For adjusting the alignment, we measured the distance between the planes and the edge of the dish. Furthermore, we measured the form of the parabolic antenna in order to make sure of the result of the distance measurement.

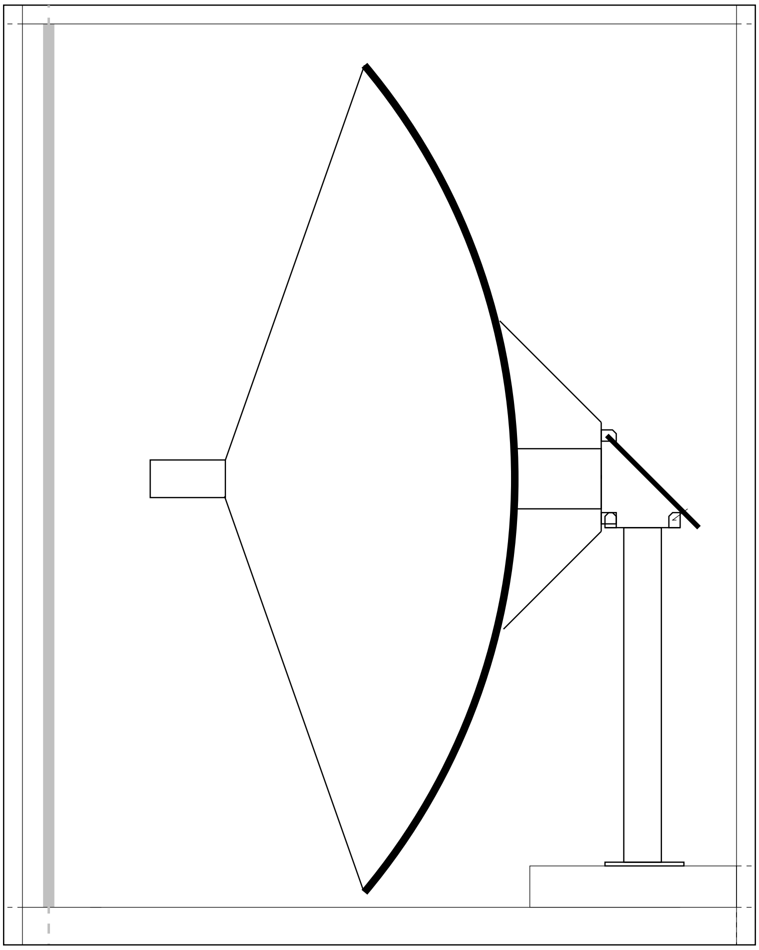

Figure 6.7: Schematic view of the apparatus for direct detection of HPDMs.

The distance between the planes and the edge of the dish

We used a ruler with aluminum frames which fit the ruler perpendicularly to the plane mirror, and a slide caliper for measuring the distance between the parabolic antenna and the ruler (Fig. 6.8). The measurement points are shown in Fig. 6.9. We conducted the measurement before and after searching for HPDMs measurement. The result is shown in Tab. 6.1. The variation of the distances between two apparatuses was smaller than ± 4mm. This variation could probably be due to the deformation of the dish from the ideal parabolic shape. If this is the case, we cannot adjust the inclination of the parabolic antenna relative to the plane mirror with higher precision than,

$$\arctan\left(\frac{4\ \mathrm{mm}}{1100\ \mathrm{mm}}\right) \simeq 0.2^\circ, \tag{6.5}$$

where 1100mm is the radius of the dish. In order to make sure of the result of the distance measurement, we measured the form of the parabolic antenna.

Figure 6.8: Picture of the ruler and the slide caliper.

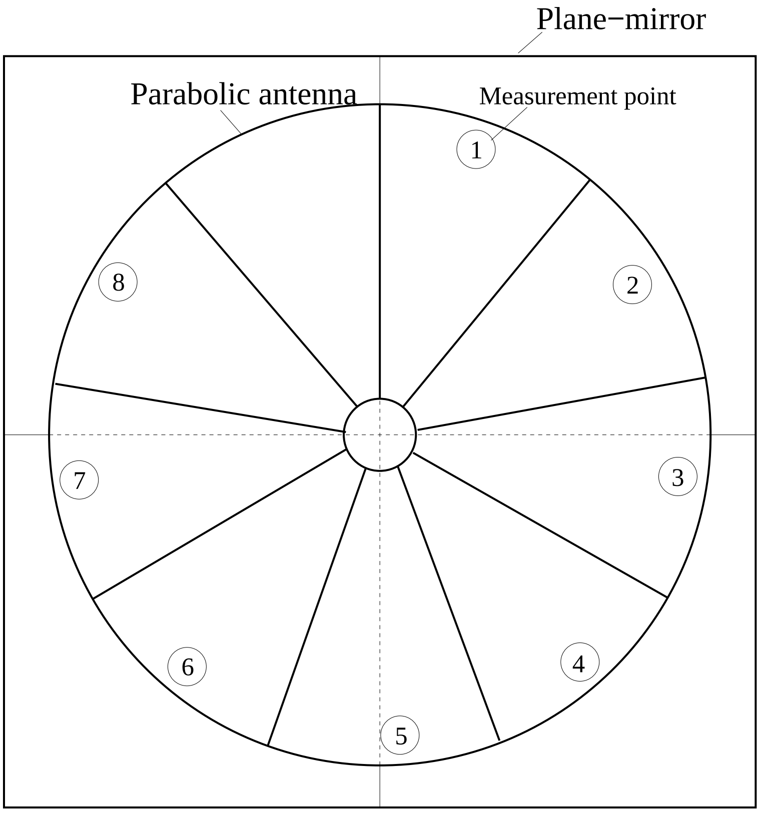

Figure 6.9: Shematic view from behind the parabolic antenna. We assigned the serial numbers to measurement points.

Serial number	Date	Distance (between the edge and the ruler) [mm]
1	Oct. 9, 2014	56.7
	Dec. 1, 2014	56.4
2	Oct. 9, 2014	60.0
	Dec. 1, 2014	59.2
3	Oct. 9, 2014	62.9
	Dec. 1, 2014	62.8
4	Oct. 9, 2014	58.3
	Dec. 1, 2014	59.2
5	Oct. 9, 2014	58.7
	Dec. 1, 2014	59.7
6	Oct. 9, 2014	64.0
	Dec. 1, 2014	64.4
7	Oct. 9, 2014	62.2
	Dec. 1, 2014	63.8
8	Oct. 9, 2014	59.5
	Dec. 1, 2014	60.7

Table 6.1: Result of the distance measurement.

The form of the parabolic antenna

We measured form of the parabolic antenna in the same manner as the adjustment of the aluminum plane, i.e. triangulation. We fitted the result of triangulation with the method of least square and the result is shown in Fig. 6.10.

We calculated subtraction between the result of triangulation and the fitted parabolic shape. As a result of calculation, we find that the deviations between the shape of parabolic antenna and ideal parabolic shape are within ± 4mm (Fig. 6.11). This result confirmed the result of the distance measurement discussed above. Therefore, we adopted the value of $0.2°$ as the inclination of the parabolic antenna relative to the plane mirror.

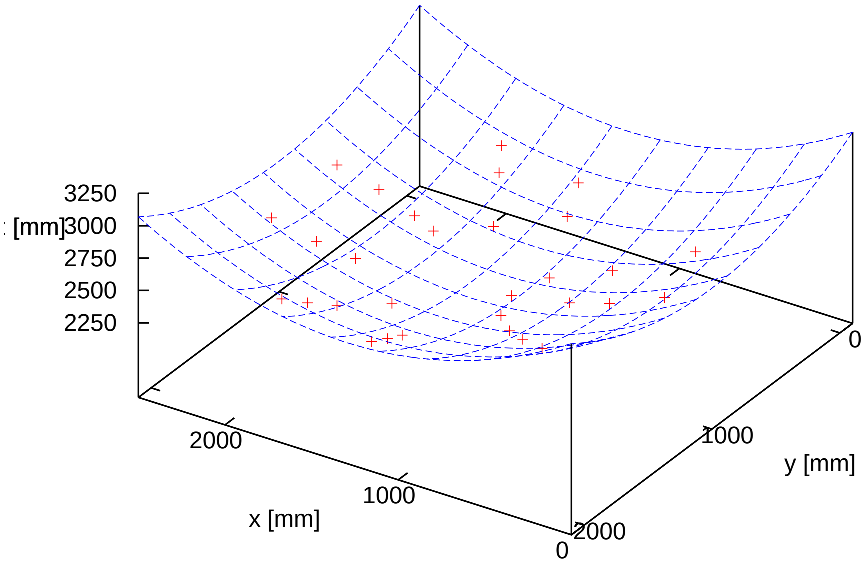

Figure 6.10: The result of triangulation measurement and fitting of parabolic antenna.

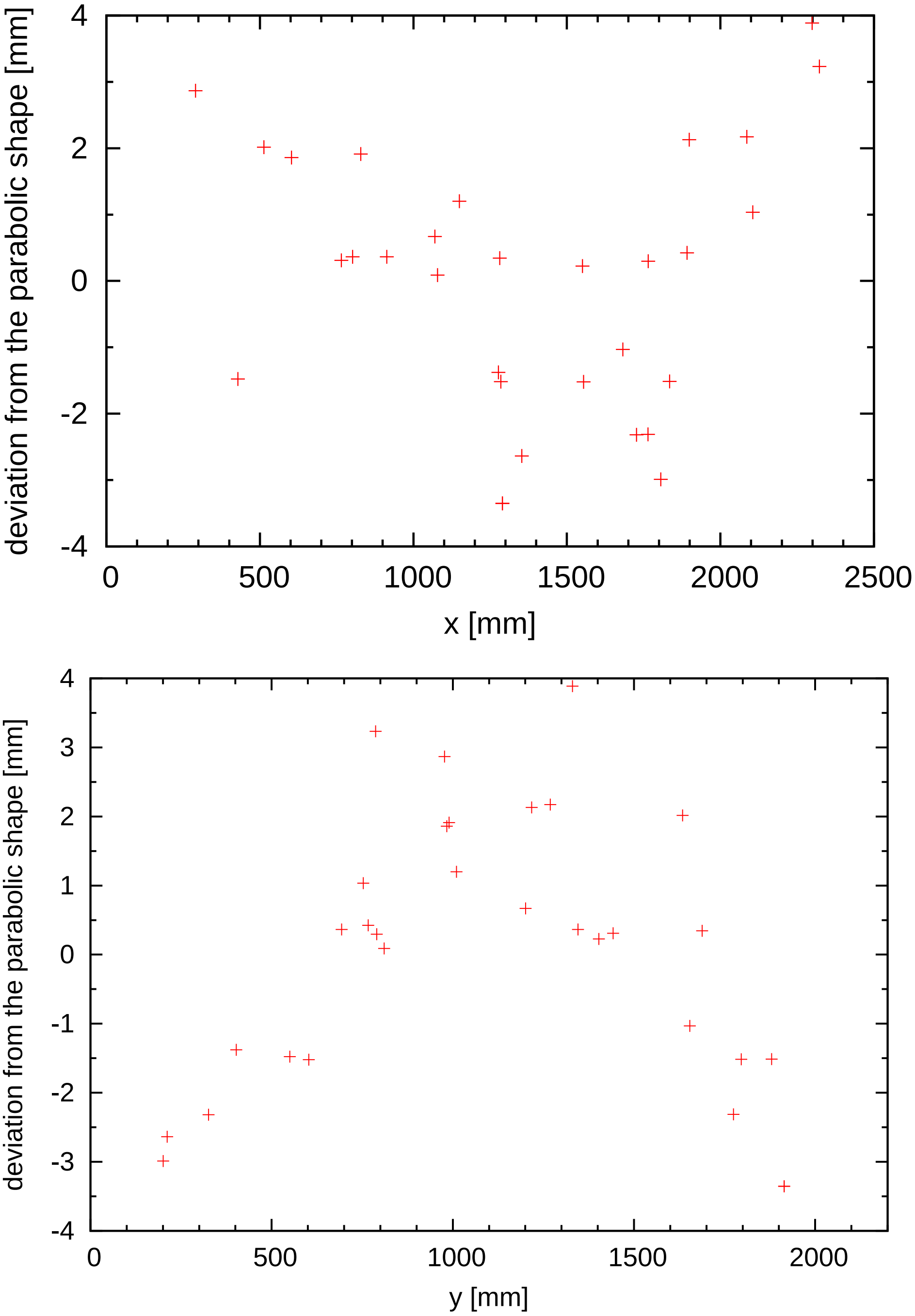

Figure 6.11: The degrees of deviation from the parabolic shape.

6.2 Search for HPDMs

6.2.1 An example of single sweep

After completion of geometric adjustment, we started searching for HPDMs. At first, let us consider the setting value of the FFT analyzer. If we assume the dark matter is isothermal, the typical velocity of the dark matter in the galaxy is expected to be $v_{\rm typ}/{\rm c} \simeq 10^{-3}$. Therefore the energy of HPDMs can be supposed to be,

$$\omega = \frac{m_{\gamma'}}{\sqrt{1-\left(\frac{v_{\rm typ}}{\rm c}\right)^2}} \simeq m_{\gamma'}\sqrt{1+(\mathcal{O}(10^{-3}))^2} \simeq m_{\gamma'}(1+\mathcal{O}(10^{-6})) \tag{6.6}$$

Since the observed frequency is about 12GHz, we obtain the signal peak from HPDMs with $\mathcal{O}$(10kHz) bandwidth. With this consideration, as we already discussed in Sect. 5.1, we determined to set the value of resolution bandwidth to be 5kHz.

The setting values of FFT analyzer in our experiment is shown in Tab. 6.2 (same as we explained in Sect. 5.1). Note that, this table represents the setting values for sub-sweep. Therefore, in order to obtain the result of single sweep, we must joint the 20 times sub-sweeps from 0.6 to 1.6 GHz. It means that the sweep time and the number of sweep points are 60 seconds and 200020 for single sweep.

Center frequency	from 675 MHz to 1575 MHz (in incliments of 50MHz)
Span	50MHz
Resolution band width	5kHz
Video band width	5kHz
Sweep point	10001
Sweep time	3 sec.
Average type	Power
Detector mode	Average

Table 6.2: Setting values of FFT analyzer for searching for HPDMs.

Fig. 6.12 shows two examples of the spectrum of single sweep. One of them has been done with the setup for search for the HPDMs, which we explained in Sect. 6.1, and the other has been done in the condition that the receiver was covered by the eccosorb at room temperature. In settings for search for HPDMs, the noise is derived from the receiver. The black body radiation derived from the receiver is returned to the receiver via the dish and the plane mirror. Although the temperature of the receiver roughly corresponds to room temperature, the spectrum does not coincide with the spectrum of the measurement of black body radiation from eccosorb at room temperature. Subtracting the latter from the former, we obtain the periodical structure as shown in Fig. 6.13. It can be considered that the cause of this difference is that the apparatuses play a role of a resonator.

Fig. 6.15 shows an explanation of resonance. In this situation, resonance condition is, of course,

$$L = n\lambda, \tag{6.7}$$

where L is the length of light path, n is natural number, λ is observed wavelength. Let us consider two adjacent frequencies f_1, f_2 ($f_2 > f_1$), and both of them satisfy the requirement of Eq. (6.7) i.e. $L = n\frac{c}{f_1} = (n+1)\frac{c}{f_2}$. The frequency subtraciton is,

$$\begin{aligned} \Delta f &\equiv f_2 - f_1 \\ &= (n+1)\frac{c}{L} - n\frac{c}{L} \\ &= \frac{c}{L}. \end{aligned} \tag{6.8}$$

The length of the ruler which we used for the geomtric adjustment as we discussed in Sect. 6.1 is 60cm, i.e. the distance between the plane mirror and the edge of the dish is about 66 cm. Since the depth of the dish is about 400mm (see Fig.5.12) and the focal length is 770mm, thus the length of light path is estimated about 3.6 m. Then we obtain,

$$\Delta f \simeq \frac{3.0 \times 10^8 \mathrm{m/s}}{3.6\mathrm{m}} \simeq 80\mathrm{MHz}. \tag{6.9}$$

This agrees rather well with the result of the single sweep(Fig. 6.13).

Furthermore, we measured the sweep with different distance. We moved the parabolic antenna closer to the planes than the initial position by 6mm. This will change the length of light path by 12mm which is approximately equal to half the wavelength. Compared with the measurement conducted at the initial position, the resonance condition was reversed (Fig. 6.14), confirming the above hypothesis.

On the other hand, we can see another periodical structure of $\Delta f \simeq 20$ MHz in the result of the eccosorb measurement. Same structures are arisen in the receiver gain as we discussed in Sect. 5.2. This corresponds to the light length path of 15 m. It can be considered that the resonance occurs between the output of the receiver and the input of the FFT analyzer. The receiver and the FFT analyzer were connected by a cable of 6 m long. If the signal reciprocated in the cable, the path length is 12 m which can explain the resonance frequencies.

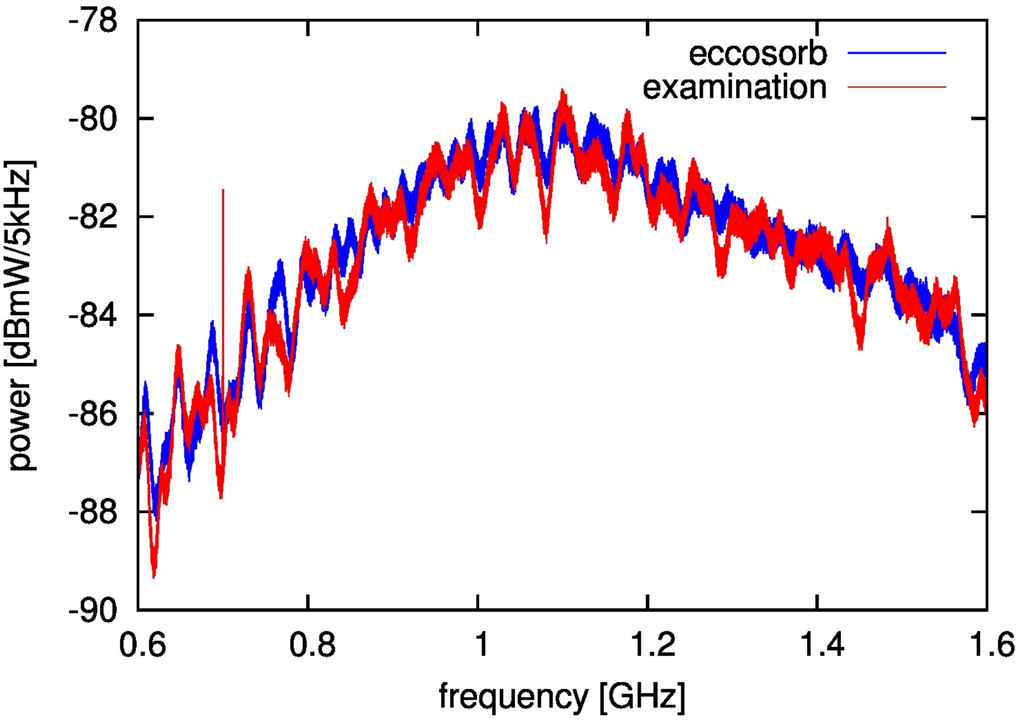

Figure 6.12: The result of measurement of the setup for searching for HPDMs compared with the eccosorb measurement.

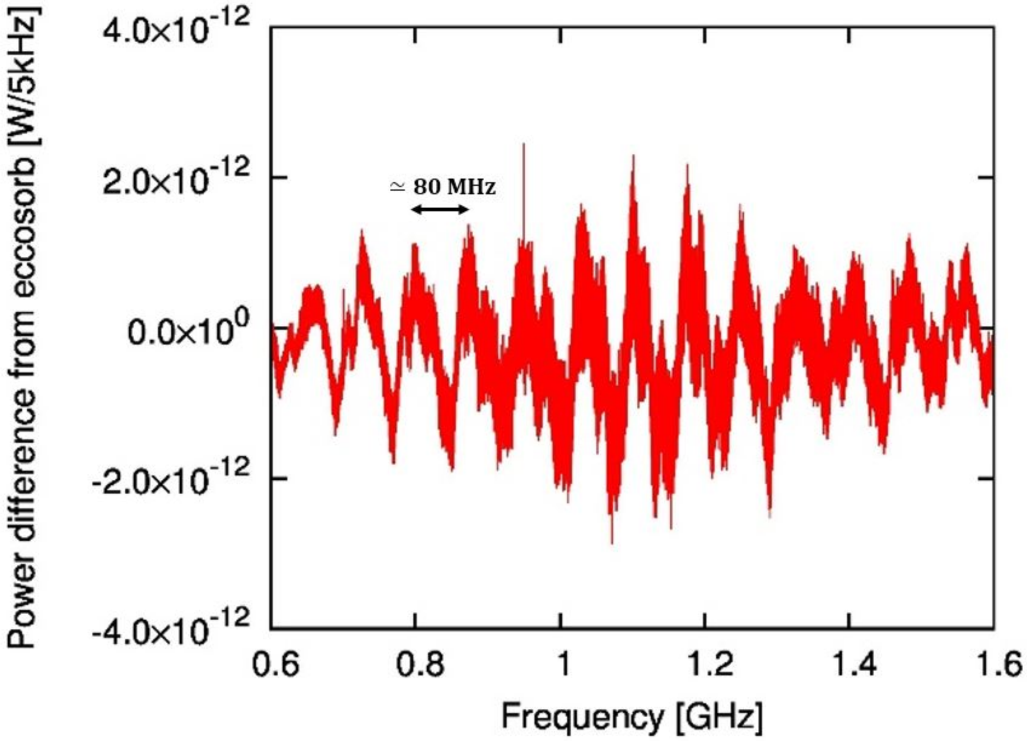

Figure 6.13: The result of subtraction between The result of measurement of the setup for searching for HPDMs and the result of the eccosorb measurement.

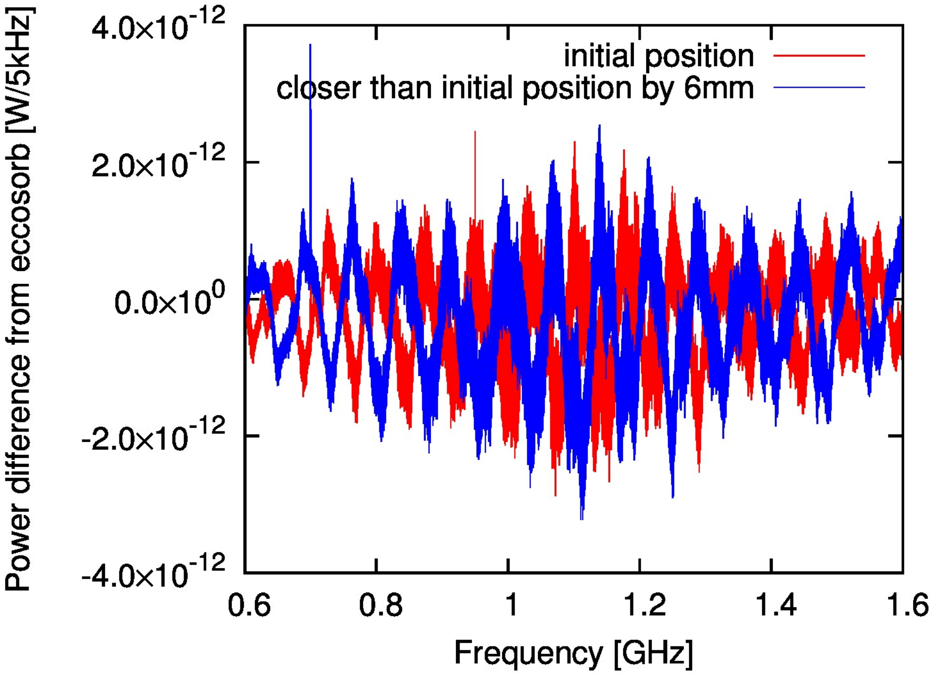

Figure 6.14: The comparison of the single sweep with different distance.

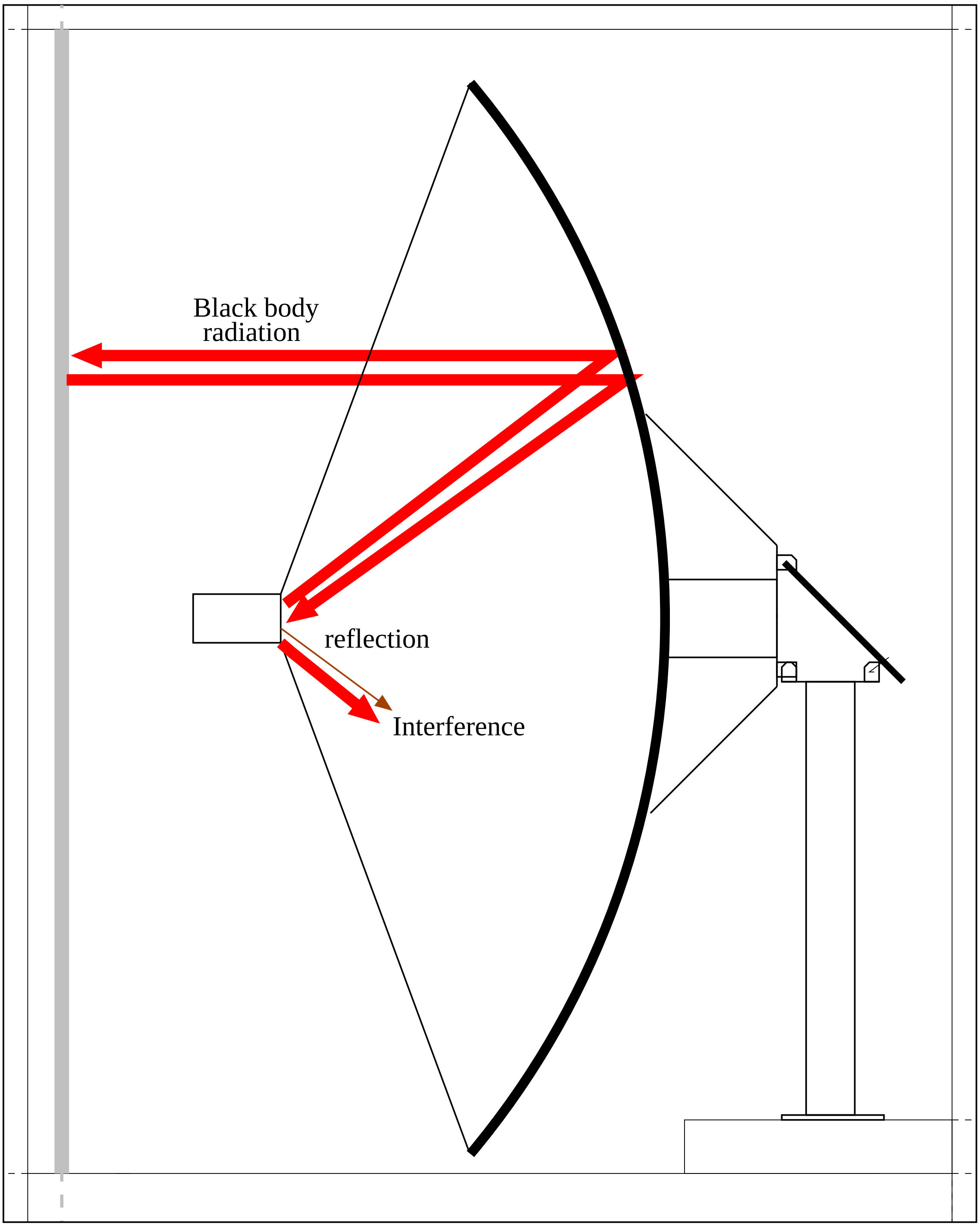

Figure 6.15: Schematic diagram of the resonance.

6.2.2 Measurement for a long period of time

Measurement and analysis procedure

The measurement was done from November 25th, 2014 to November 28th, 2014 (4days). The measurement procedure is as follows:

(1) We conducted a sweep from 0.6 to 1.6 GHz with 50MHz sub-sweep spans as we explained in section 5.1.

(2)After each sweep, we measured an extra sweep around 1050 MHz in detail in order to calibrate the local oscillator frequency of the receiver (we named this "calibration sweep"). The signal generator was installed outside of the space between the plane mirror and the parabolic antenna in order not to disrupt the propagation of the radio wave arising from HPDMs at the plane mirror (Fig. 6.16). A piece of wire with a length of 10mm was attached to the center conductor of the output of the signal generator, and it was used to radiate the signal into the space.
The setting parameters of the generator and FFT analyzer for the calibration sweep are shown in Tab. 6.3. Since the output frequency is 950MHz, the frequency of the thirteenth harmonic wave is received by the receiver with the frequency of 12.35GHz (the down-converted frequency is 1.05GHz). The receiver receives the signal collected by the parabolic antenna directly, or the signal reflected once by the plane mirror and then by the parabolic antenna. Two examples of the result of calibration sweep are shown in Fig. 6.17.

(3)We repeated the steps (1) and (2).

During the measurement, we repeated the above procedure 2700 times. Time variations in temperature of the receiver and L.O. frequency during the search of HPDMs are shown in Fig. 6.18 and Fig. 6.19 respectively.

It is seen that the nominal frequency of FFT was drifting with the temperature with respect to the standard frequency of the signal generator. The frequency shift Δf ranged from 40 kHz to 85 kHz.

We sorted the obtained sweep data into the groups of the same L.O. frequency shift Δf within the resolution bandwidth of 5kHz. They are summarized in Tab. 6.4.

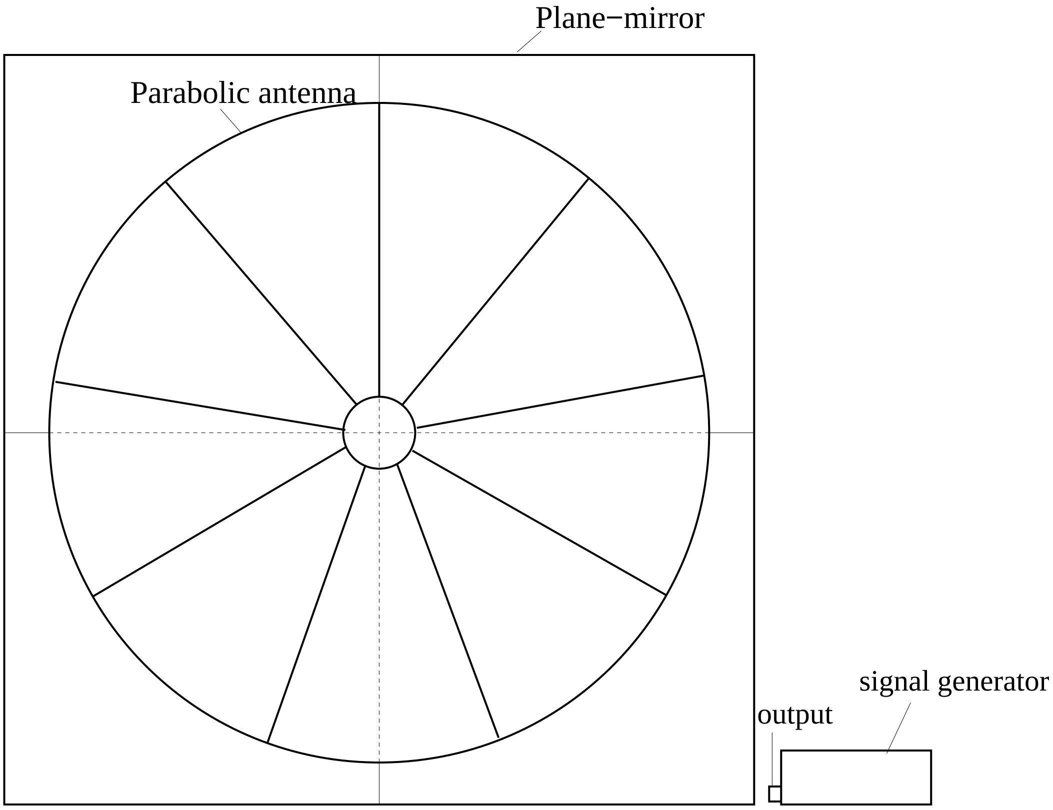

Figure 6.16: Schematic view from behind the parabolic antenna. The signal generator was set on the outside of the searching apparatuses.

Component	parameter	value
Signal generator	Carrier frequency	950 MHz
	RF level	+13dBm
	Modulation	Off
FFT analyzer	Center frequency	1.050050 GHz
	Span	200kHz
	Resolution band width	100Hz

Table 6.3: Setting parameters of the signal generator and FFT analyzer for the calibration sweep

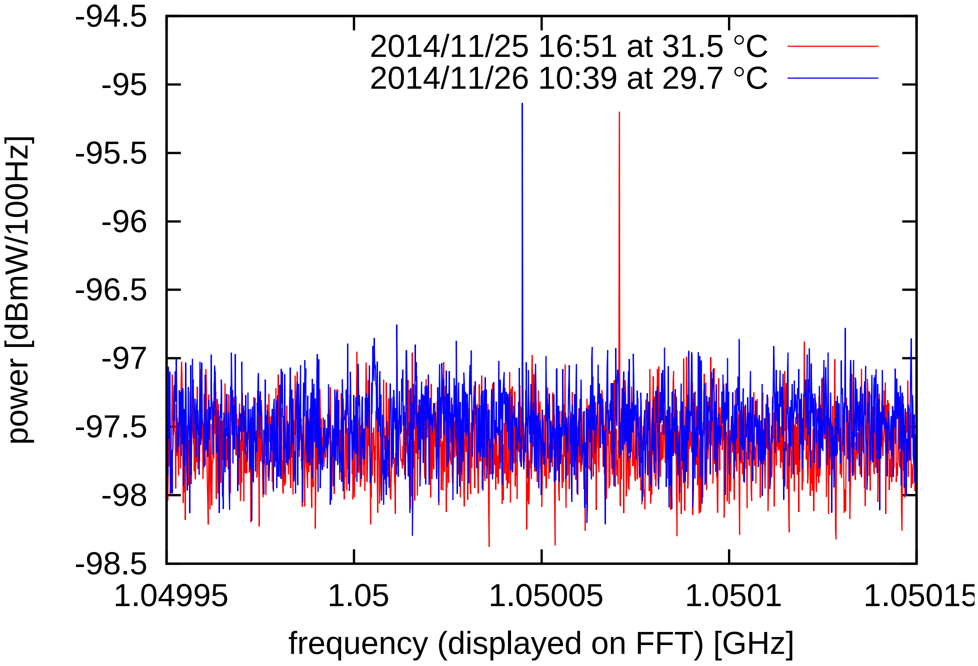

Figure 6.17: Two examples of the result of reference signal measurement

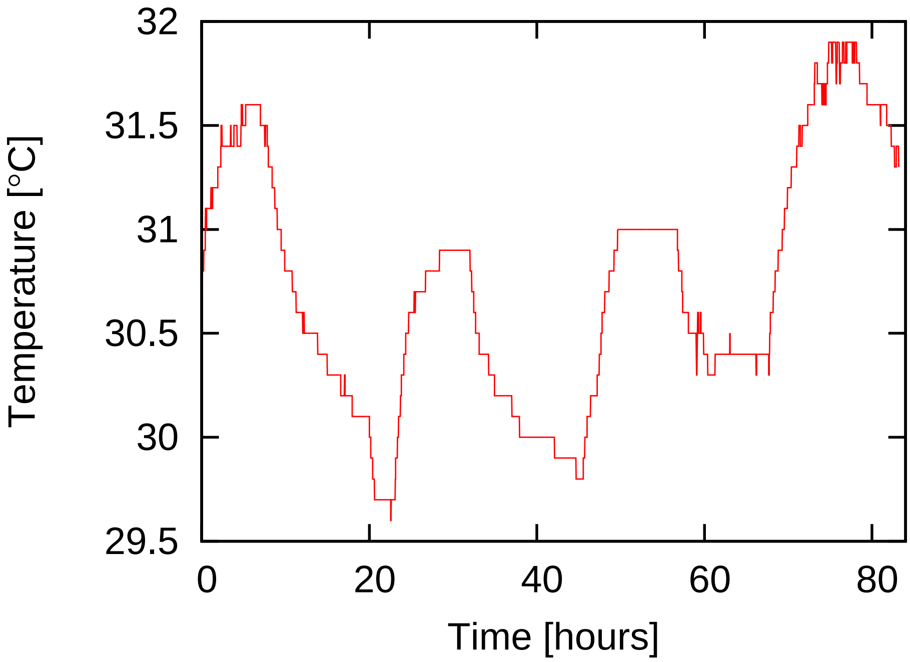

Figure 6.18: The time series graph of the temperature of the receiver. The origin of the time is Nov. 25 12:59:56.

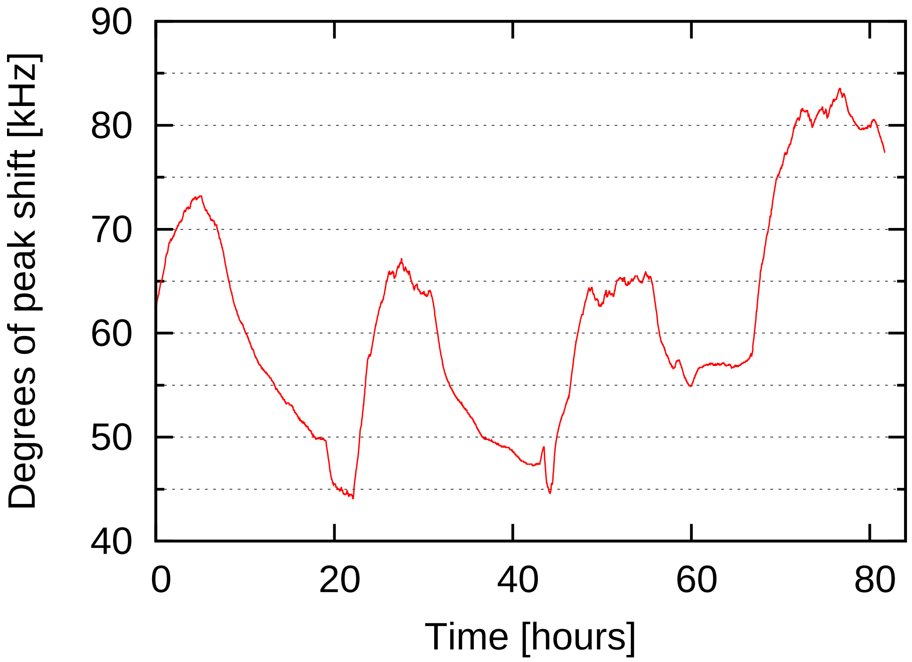

Figure 6.19: The time series graph of the peak shift.The origin of the time is Nov. 25 12:59:56 and the origin of the frequency is 1050MHz.

Frequency shifts [kHz]	Number of sweeps
$40 \leqq \Delta f < 45$	63
$45 \leqq \Delta f < 50$	377
$50 \leqq \Delta f < 55$	353
$55 \leqq \Delta f < 60$	557
$60 \leqq \Delta f < 65$	456
$65 \leqq \Delta f < 70$	326
$70 \leqq \Delta f < 75$	188
$75 \leqq \Delta f < 80$	157
$80 \leqq \Delta f < 85$	251

Table 6.4: Number of sweeps in the Frequency shift groups

To find out the possible evidence of HPDMs from the data of the measurements, we take several steps of the analytical process which we explain in the following.

1. We combined all 2700 sweeps without correcting the frequency shift. We calculated difference between ends of two sub-sweeps, thus we obtained the depth of the discontinuities. Note that, we did not use the combined data for later analysis because the data were not corrected.

2. We combined the data of each group and each sub-sweep span separately. For example, the number of sub-sweeps of 0.6-0.65 GHz in the group of 40 kHz$\leqq \Delta f <$45 kHz is 63 (the other sub-sweeps were also conducted 63 times). We combined these 63 sub-sweeps data.

   After combining, we eliminated the discontinuities by adding the difference between ends of two sub-sweeps which we calculated in procedure 1. Since the discontinuities were corrected, we jointed each sub-sweep.

3. We corrected the L. O. frequency of the LNBF, and combined the data of all groups.

4. We divided the power by the LNBF gain, thus we obtained the emission power which entered the LNBF.

5. We searched for possible excess power derived from HPDMs by fitting the sum of a quadratic function and expected peak shape function for HPDM. We calculated optimum excess power and its error at each frequency bin.

6. We computed the distribution of P/Δ_P. Because of the correlation between a certain bin and its neighboring two bins, the distribution of P/Δ_P is broadened, i.e. Δ_P is made small. We corrected this broadening by the correlation from the distribution of P/Δ_P.

7. We examined the significance of the excess power with the correction of procedure 6. If there is no significant excess of the power, we estimated upper limit of kinetic mixing parameter χ.

We explain each step of the analysis in more detail below.

1. Estimating the discontinuities

At first, we estimated the depth of the discontinuities which exist at the connecting points of sub-sweeps. Since these discontinuities arose at the connecting points of sub-sweeps independent of the frequency shifts, thus we combined all 2700 single-sweeps without correcting the frequency shifts (Fig. 6.20). For example, there is a discontinuity at 0.8 GHz (Fig. 6.21). Tab. 6.5 shows the discontinuities of all connecting point of sub-sweeps. We corrected the discontinuities.

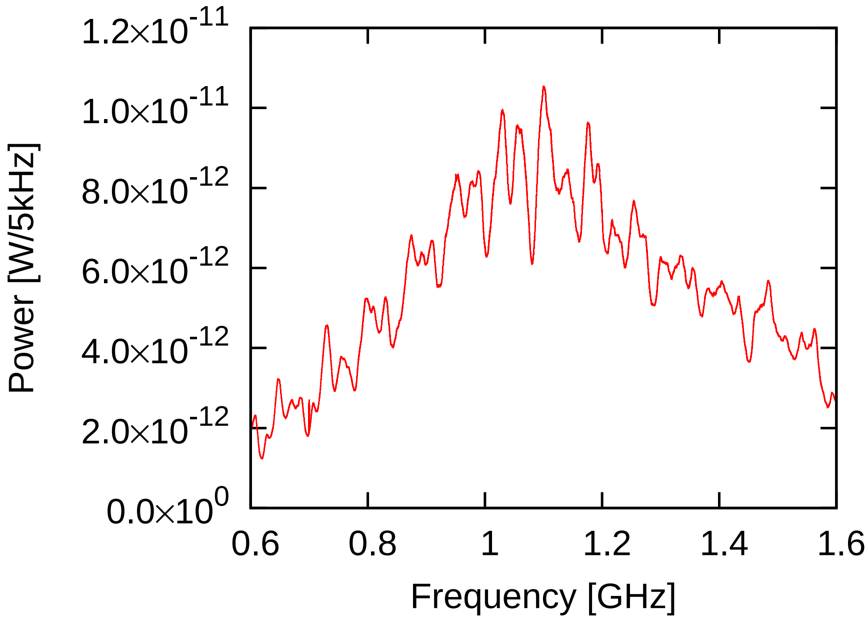

Figure 6.20: The spectrum combined without correcting the frequency shifts.

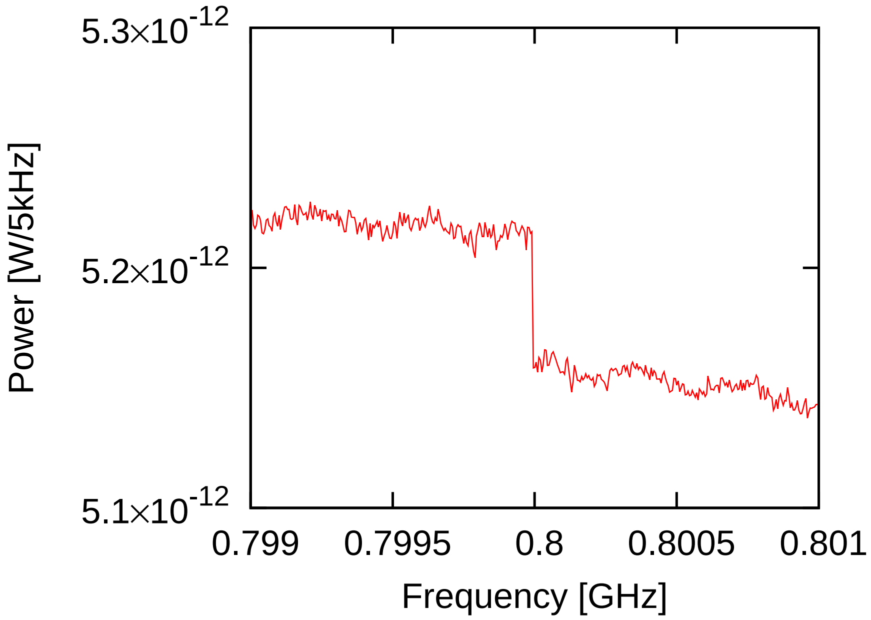

Figure 6.21: The enlarged view of Fig. 6.20. We determined the difference between ends of two single-sweeps as the depth of the discontinuities.

Frequency [GHz]	Difference of power [$\times 10^{-15}$W/5kHz]
0.65	8.48
0.7	5.3
0.75	10.8
0.8	-56.76
0.85	2.13
0.9	1.66
0.95	8.60
1.0	-11.1
1.05	0.97
1.1	14.9
1.15	-92.1
1.2	48.57
1.25	9.46
1.3	-1.94
1.35	-2.10
1.4	-3.15
1.45	6.70
1.5	3.54
1.55	6.32

Table 6.5: The depth of the discontinuities at each joint of sub-sweeps. “ Difference of power ” means the subtraction of the end of lower frequency side of sub-sweep from higher one.

2. Correcting the discontinuities

We combined the data of each frequency shift group and each sub-sweep span separately. For example, we added the correction value estimated in Tab. 6.5 into sub-sweeps of 0.75-0.8 GHz and 0.8-0.85 GHz in the group of 55 kHz$\leqq \Delta f <$60 kHz (Fig. 6.22). As a result, the discontinuous structure is corrected, thus we were allowed to connect all the sub-sweeps in same frequency shift group to make a power spectrum of the full frequency range between 0.6-1.6 GHz.

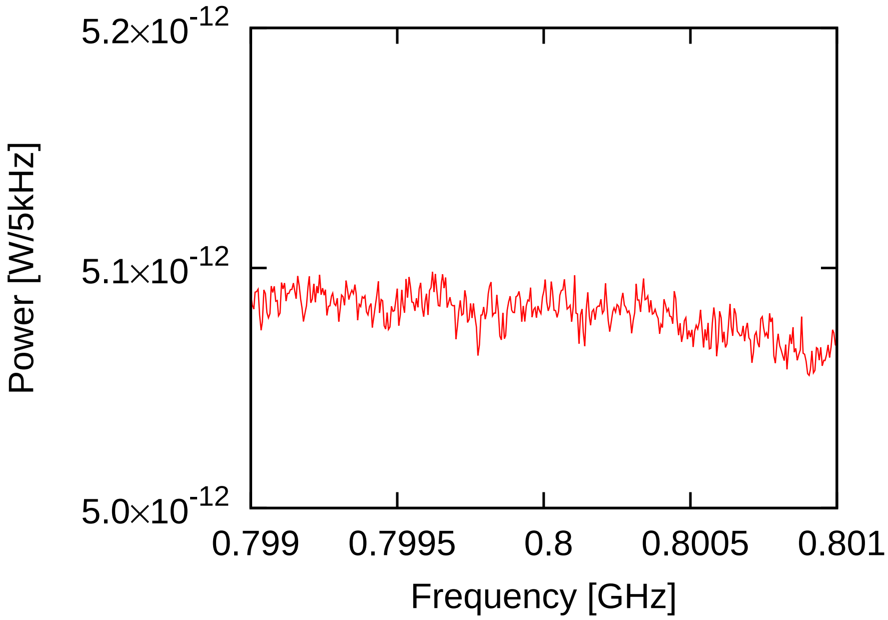

Figure 6.22: The result of correcting the sub-sweeps of 0.75-0.8 GHz and 0.8-0.85 GHz in the group of 55 kHz$\leqq \Delta f <$60 kHz.

3. Combination of all sweeps

After connecting sub-sweeps, we corrected the frequency shift for the data of groups by shifting the RBW bins. For example, for the data of the group of 55 kHz$\leqq \Delta f <$60 kHz, the number of bins corresponding to the frequency shift is,

$$N_{\rm bin} \equiv \left[\frac{\Delta f}{\rm RBW}\right] = 11. \tag{6.10}$$

Next, we combined the data of all frequency shift groups with the weighted mean method. We divided all the data into 9 groups of the same L.O. frequency shift as summarized in Tab. 6.4. The number of bins corresponding to the frequency shift ranged from 8 to 16 bins. Because of the difference of the frequency shift, there are several points whose frequency does not correspond to the data of other groups as shown in Fig. 6.23. We excluded these points for the analysis.

On the other hand, we cannot correct the frequency shift which is smaller than 5 kHz. The distribution of the excess power derived from HPDMs is distorted by this reason. We explain about this distortion in Chap. 7.

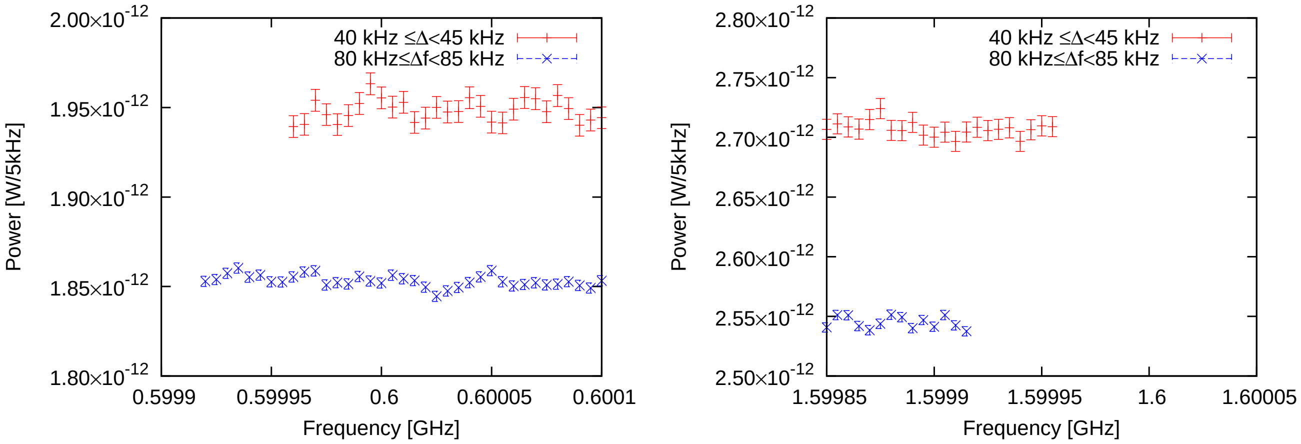

Figure 6.23: The comparison between the combined data in the group of 40 kHz$\leq \Delta f <$45 kHz and the combined data in the group of 80 kHz$\leq \Delta f <$85 kHz. Left: enlarged figure around 0.6 GHz. Right: enlarged figure around 1.6 GHz. There are 8 points which do not overlap on either side.

4. Division by the gain of the LNBF

In order to estimate the input power to the receiver, we divided the power by the gain of the receiver discussed in Sect. 5.2. Since the measuring time is much less than measurement for HPDMs, the statistical error is large. In order to prevent this problem, we fitted the gain. The fitting procedure is as follows:

(a) We fitted the quadratic function to 1000 data points starting from the lower edge. LNBF gains in the first 500 RBW bins are determined by the fitting result.

(b) Gain in the 501th bin is determined by a quadratic function fitting to the 1000 data points around the said bin, i. e. from bin 1 to bin 1000. Gains in the 502th bin is determined by a fitting to the data points of bin 2 to bin 1001, and so on.

(c) Gains in the 500 upper most bins are again determined by a fitting to the last 1000 data points.

For example, Fig. 6.24 shows the result of fitting for the data around start frequency. By this method, we obtained the fitted curve for 0.6-1.6 GHz (Fig. 6.25). We divided the combined data by the fitted curve of the gain of the LNBF (Fig. 6.26). Note that, we must calibrate the L.O. frequency of the LNBF at gain calibration measurement. We measured calibration-sweep in gain calibration measurement. In this measurement, the degrees of frequency shift is 23 bins. As with the procedure 3, we corrected the frequency shifts, and we excluded the points which do not overlap with the combined data computed in procedure 3 for the analysis. Eventually, we are ready to search for the excess power derived from HPDMs. We explain the analysis of the search for HPDMs in following chapter.

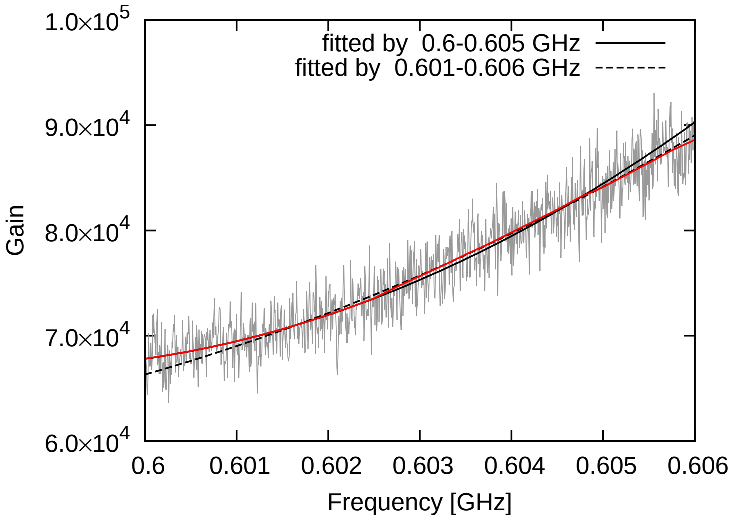

Figure 6.24: The fitting result near the lower end frequency 0.6 GHz. Solid line shows the quadratic function fitting with the points from 0.6 GHz to 0.605 GHz. We used this result as the gain of 0.6-0.6025 GHz. Dotted line shows the fitted function with the points from 0.601-0.606 GHz. We used the fit value at the center point(0.6035 GHz) for the gain at this frequency. Connecting these results, we obtain red solid line.

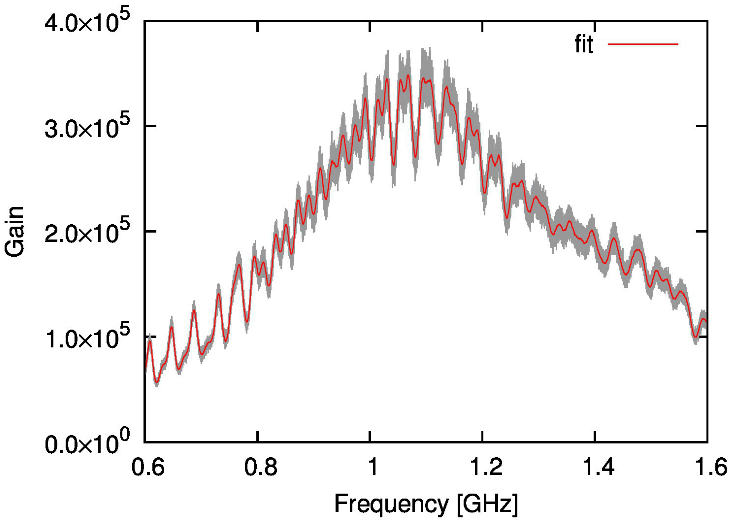

Figure 6.25: The overall view of the result of fitting which we explain in Fig. 6.24.

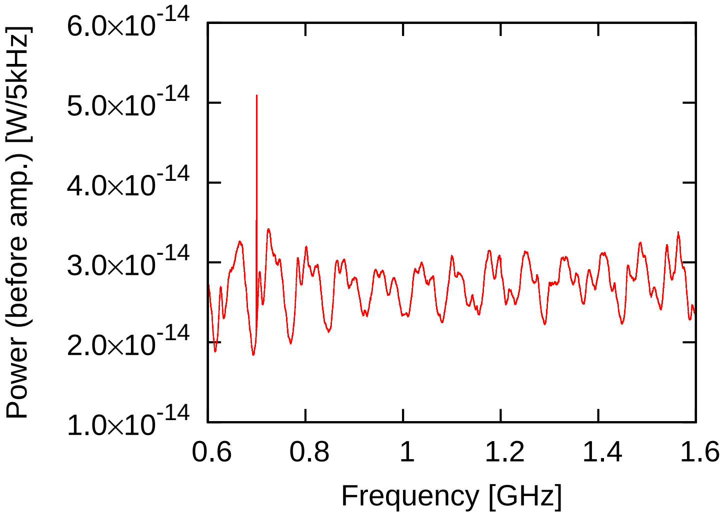

Figure 6.26: The power before amplification by the LNBF. This result is obtained by dividing the combined data which we calculated in procedure 3 by the gain of the LNBF.

Chapter 7

Result and Discussion

7.1 Estimation of the distribution of excess power caused by HPDMs

The energy of the HPDMs which corresponds to the energy of the conversion photons is,

$$\omega = \frac{m_{\gamma'}}{\sqrt{1-\left(\frac{v}{\mathrm{c}}\right)^2}} \simeq m_{\gamma'}\sqrt{1+\left(\frac{v}{\mathrm{c}}\right)^2}, \tag{7.1}$$

where v is the velocity of the HPDMs in the frame of the Earth. If $v = 0$, we obtain,

$$\omega_0 = m_{\gamma'}. \tag{7.2}$$

Then the frequency of the conversion photon is,

$$f = 0.24\ \mathrm{GHz}\left(\frac{\omega}{\mu\mathrm{eV}}\right), \tag{7.3}$$

and for $v = 0$,

$$f_0 = 0.24\ \mathrm{GHz}\left(\frac{m_{\gamma'}}{\mu\mathrm{eV}}\right). \tag{7.4}$$

We assume the isothermal dark matter halo, i.e. the velocity of the HPDMs obeys Maxwell-Boltzmann distribution with the velocity dispersion v_0,

$$f(\boldsymbol{v}, \boldsymbol{v}_{\mathrm{E}}) = \frac{1}{(\pi v_0^2)^{3/2}} e^{-|\boldsymbol{v}+\boldsymbol{v}_E|^2/v_0^2}, \tag{7.5}$$

where $\boldsymbol{v}_{\mathrm{E}}$ is the velocity of the Earth with respect to the galactic halo. The velocity dispersion v_0 is argued by several authors [24] [25], and we set $v_0 =$ 220km/s which is the commonly used value. The earth speed relative to the dark matter halo is described by

$$|\boldsymbol{v}_{\mathrm{E}}| = v_{\odot} + v_{\mathrm{orb}} \cos\gamma \cos(\Omega t), \tag{7.6}$$

where $v_\odot = v_0 + 12\text{km/s}$ is the solar system velocity around the galactic center, $v_{\text{orb}} = 30\text{km/s}$ is the earth's orbital velocity around the sun, $\gamma \simeq 60^\circ$ is the inclination angle of the earth orbital plane with respect to the galactic plane, $\Omega = 2\pi/\text{year}$, and t is the elapsed time from June 2nd in years. Since our experiments was conducted at the end of November, we set $t \simeq 0.5$. Therefore, we obtain,

$$v_{\text{E}} \simeq 217\text{km/s}. \tag{7.7}$$

Inserting Eq. (7.7) and Eq. (7.1) into Eq. (7.5), we obtain the frequency distribution $F(f, f_0)$ using Eq. (7.4) and Eq. (7.3). For example, we calculated $F(f, f_0)$ for $f_0 = 12.4$ up to $f = f_0 + 30$ kHz. It is shown in Fig. 7.1 with a binning of 5 kHz.

Although the receiver frequency is calibrated, if the frequency deviation is smaller than the RBW, we cannot correct such a small shift. For example, even if f_0 corresponds to the lower edge of a bin of 5 kHz in a certain single sweep, f_0 may correspond to the middle of the bin in another sweep because the frequency correction is only possible in a step of 5kHz. However, we can estimate the effect.

Assuming that the distribution of the small frequency shift is uniform, the number of single sweeps should uniformly distributes over the uncorrectable frequency shift of,

$$\Delta f_m = \Delta f - \text{RBW} \times \left[\frac{\Delta\text{f}}{\text{RBW}}\right]. \tag{7.8}$$

The distribution of $N_{\Delta f_m}$ can be obtained from the time series of the peak shift shown in Fig. 6.19, which is measured with a frequency resolution of 1kHz. The distribution is, in fact, roughly consistent with the uniform distribution (Tab. 7.1).

For these reasons, we calculated the effective frequency distribution of the power derived from HPDMs using $F(f, f_0)$ as follows:

$$F_{\text{ave}}(f, f_0) = \frac{1}{\text{RBW}} \int_0^{\text{RBW}} F(f, f_0 + f')df'. \tag{7.9}$$

This was done for various values of f_0 and the result is shown in Fig. 7.2. The effective distributions with any f_0 have similar form, thus we decide to use the distribution for $f_0 = 12.4$ GHz for all values of f_0.

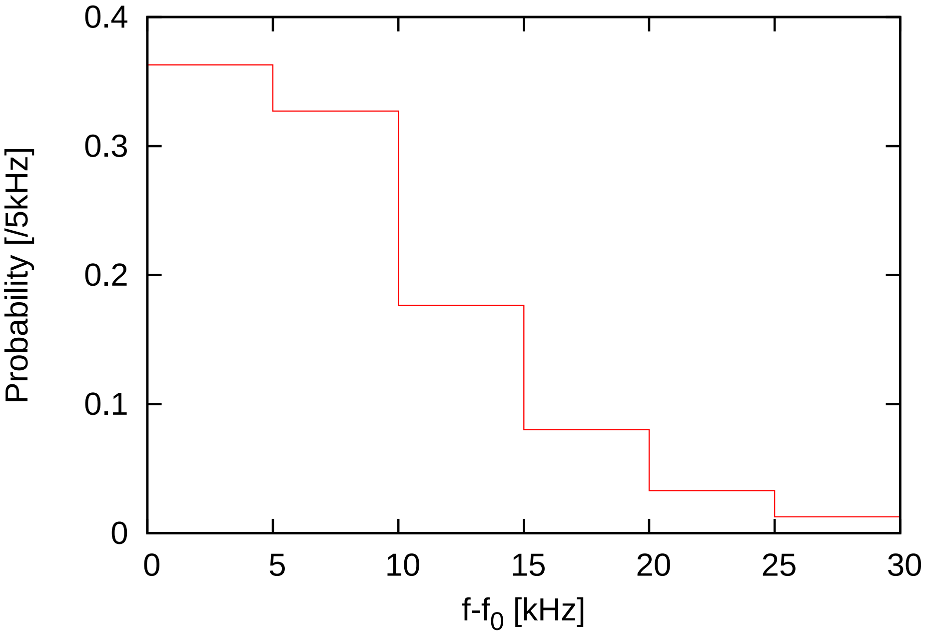

Figure 7.1: An example of the frequency distribution for $f_0 = 12.4$ GHz.

Frequency shifts [kHz]	Number of sweeps
$0 \leqq \Delta f_m < 1$	606
$1 \leqq \Delta f_m < 2$	536
$2 \leqq \Delta f_m < 3$	555
$3 \leqq \Delta f_m < 4$	441
$4 \leqq \Delta f_m < 5$	562

Table 7.1: Number of sweeps of each small frequency shifts.

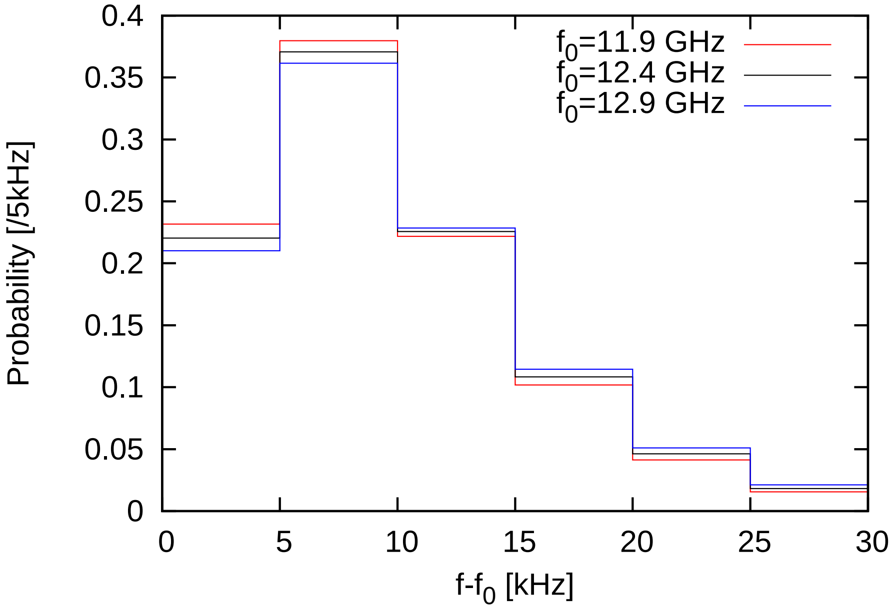

Figure 7.2: The expected effective distribution of HPDM signal.

7.2 Estimation of upper limit of the excess power

7.2.1 Fitting

We searched for possible excess power derived from HPDMs in the spectrum shown in Fig. 6.26. However, the baseline of the spectrum was distorted, thus we fitted a quadratic function with the points around the frequency f_0 to obtain the baseline. We used 50 points with the center at f_0 for fitting a quadratic function and a peak arising from HPDMs (Fig. 7.3). We computed the fitting with f_0 at every RBW bin and estimated the excess power of the best fit P and its error Δ_P (Fig. 7.4). Note that, we used Eq. (5.9) for estimating the standard error of the power with RBW 5kHz bin. Eq. (5.9) means that the standard error of power $\bar{P}_N$, combination of N sweeps, is

$$\sigma_{\bar{P}_N} = \frac{2.57 \times 10^{-2} \times \bar{P}_N}{\sqrt{N}}. \tag{7.10}$$

If there were excess power derived from HPDMs, the value of P at the frequency which corresponds to the mass of HPDMs would be significantly larger than the value of Δ_P. There were actually some points which gave large value of P/Δ_P. However, they were also observed even with a setup which is not for the search for HPDMs (as is explained in detail in appendix C). Therefore, we concluded they are spurious.

We calculated the distribution of P/Δ_P (Fig. 7.5). The filled area means the fitting result including the narrow spurious peaks. We excluded these points for search for the excess power derived from HPDMs, accordingly.

Moreover, we excluded connecting points of the sequence of sub-sweeps from the object of the analysis because of the rough correction of the discontinuities. Taking the frequency shifts into account, there are 8points which should be excluded from the object of the analysis at every connection point of the sub-sweeps. Around 0.65GHz, for example, we excluded the frequency range of 0.64992-0.64996 GHz.

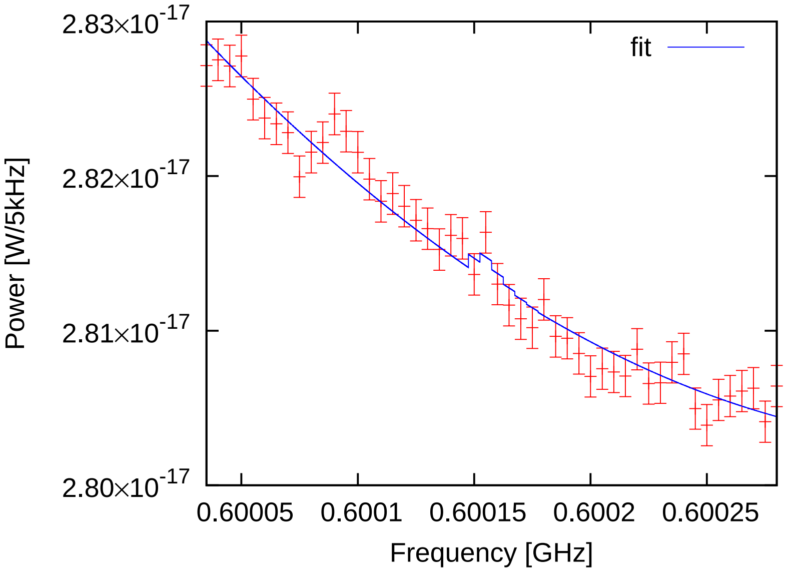

Figure 7.3: An example of the fitting a quadratic function and a peak derived from HPDMs.

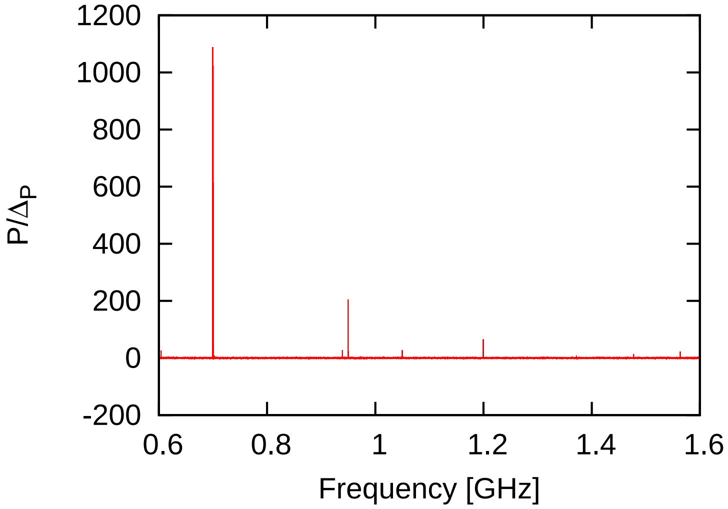

Figure 7.4: The result of fitting versus frequency. Vertical axis shows the value of P/Δ_P.

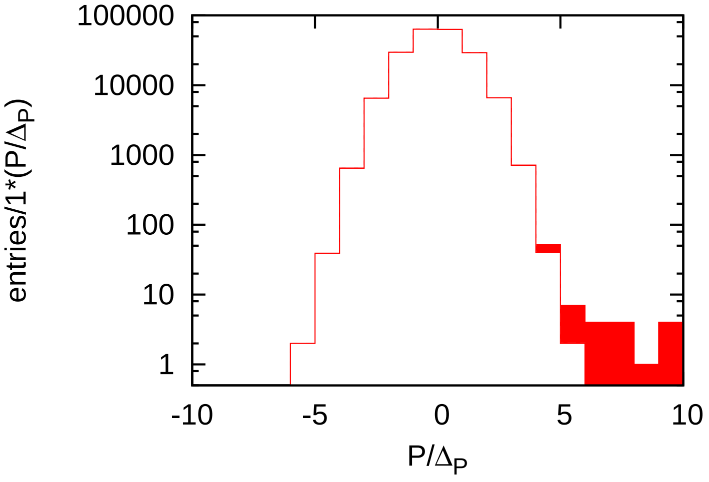

Figure 7.5: The distribution of P/Δ_P. The filled corresponds to the fitting result of the narrow spurious peaks.

7.2.2 Recalculation of the standard error

From the result described in Fig. 7.5(excluding the filled area), we used the following Gaussian function for fitting:

$$\frac{N}{\sqrt{2\pi\sigma^2}} \exp\left(-\frac{(P/\Delta_P - \mu)^2}{2\sigma^2}\right), \tag{7.11}$$

where μ is mean of the distribution of P/Δ_P. We used σ as a fitting parameter. Here, it had been confirmed that the power of a certain bin influenced the neighboring bins by FFT. As a result of the influence, the standard error Δ_P was made smaller than the true value[1] (see appendix D).

On the basis of the effect, we corrected the standard error and recalculated the distribution of P/Δ'_P for recalculated error Δ'_P(Fig. 7.7).

This distribution is consistent with the Gaussian of mean 0, and standard error 1. According to the Gaussian distribution, the expected number which exceeds 4σ is about 6.3. In this result, the number was 8 which was not significantly larger than the expected number. Fig. 7.9 and Fig. 7.10 shows the 8 spectra which exceeds 4σ. Furthermore, there is no entry which exceeds 5σ.

As a result, no significant excess was seen for any f_0 except the spurious peaks which have nothing to do with the HPDMs as explained in appendix C. Therefore, we calculated an upper limit of the excess power $P_{\rm DM}$ at 95% confidence level (C.L.) for f_0 at every RBW bin. They are shown in Fig. 7.8.

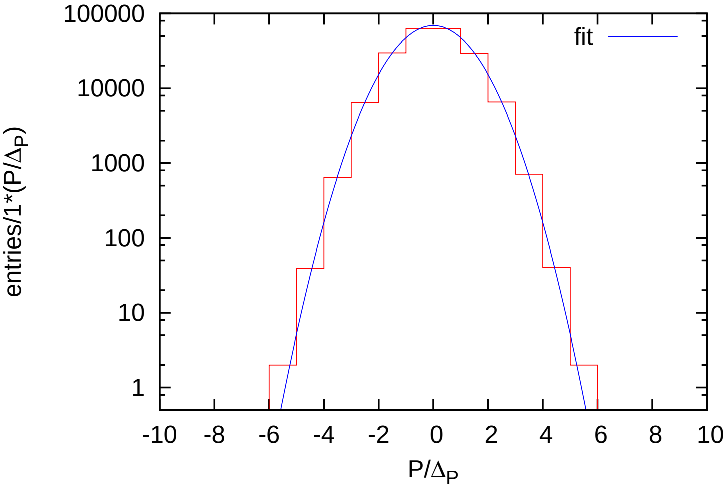

Figure 7.6: We fitted gaussian with the histgram of Fig. 7.5

---

[1] By fitting the Gaussian function with the distribution of P/Δ_P, we obtained the fitting result of $\sigma = 1.1275 \pm 0.002497$ (Fig. 7.6). It is significantly larger than one, which is expected when there is no excess power.

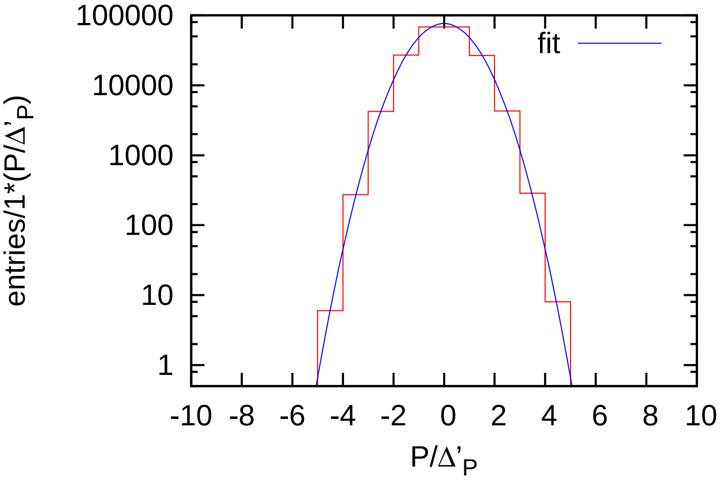

Figure 7.7: The distribution of P/Δ'_P. We corrected the standard error in consideration of the correlation.

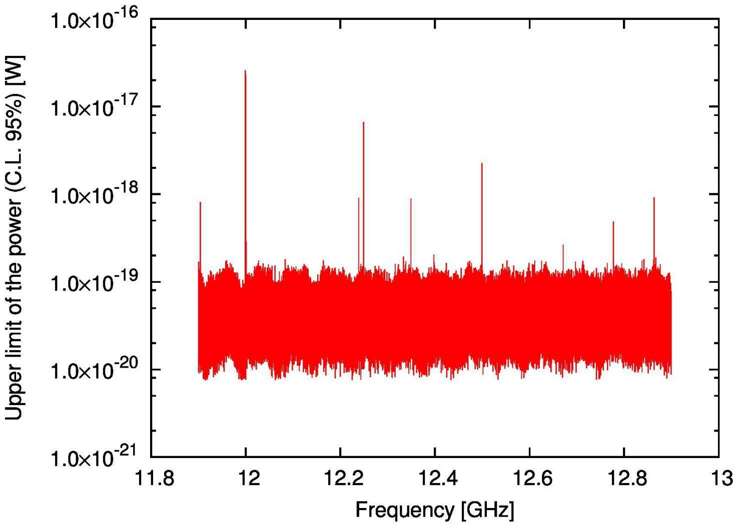

Figure 7.8: 95% C. L. upper limit of excess power derived from HPDMs.

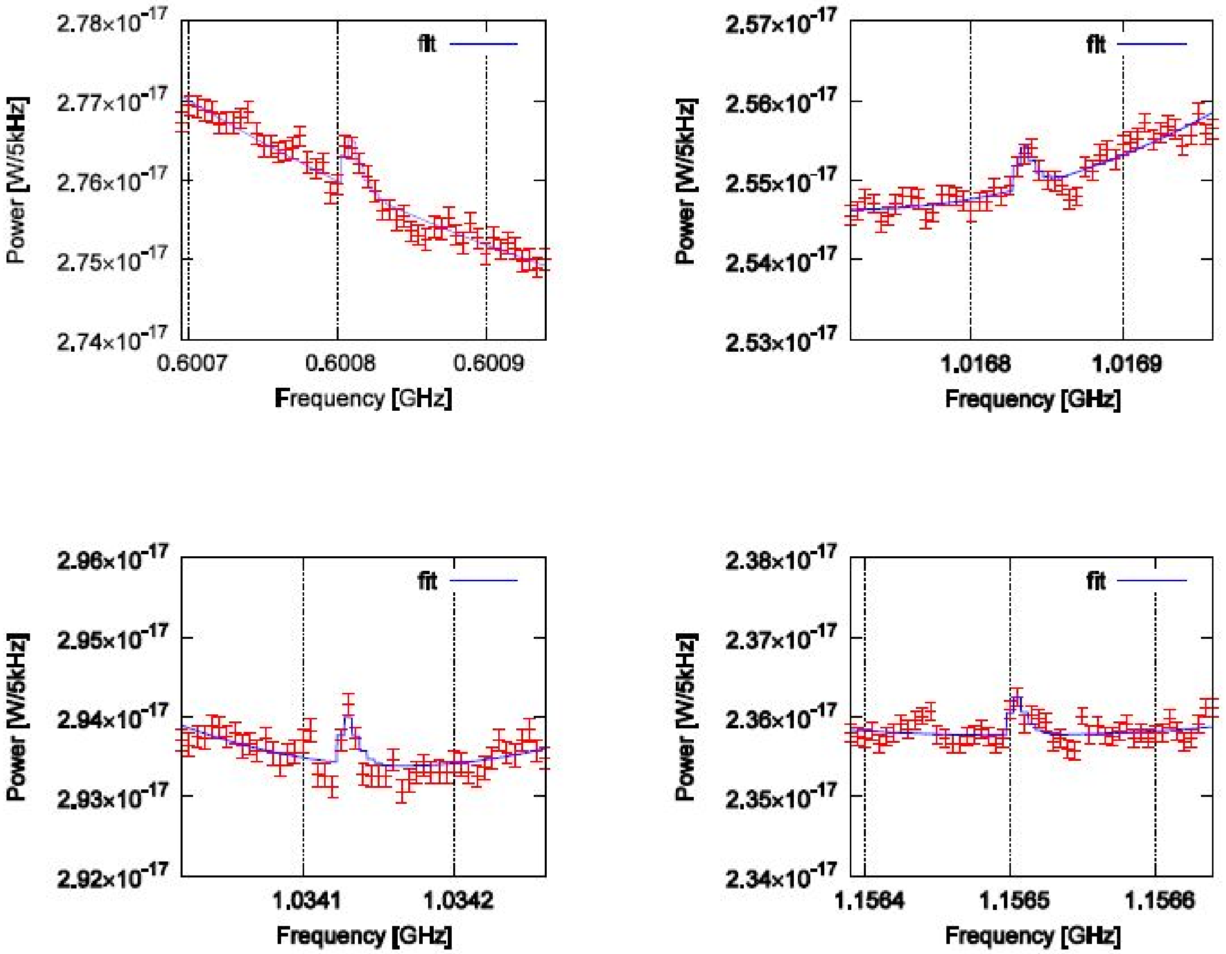

Figure 7.9: The spectra which exceed 4 σ

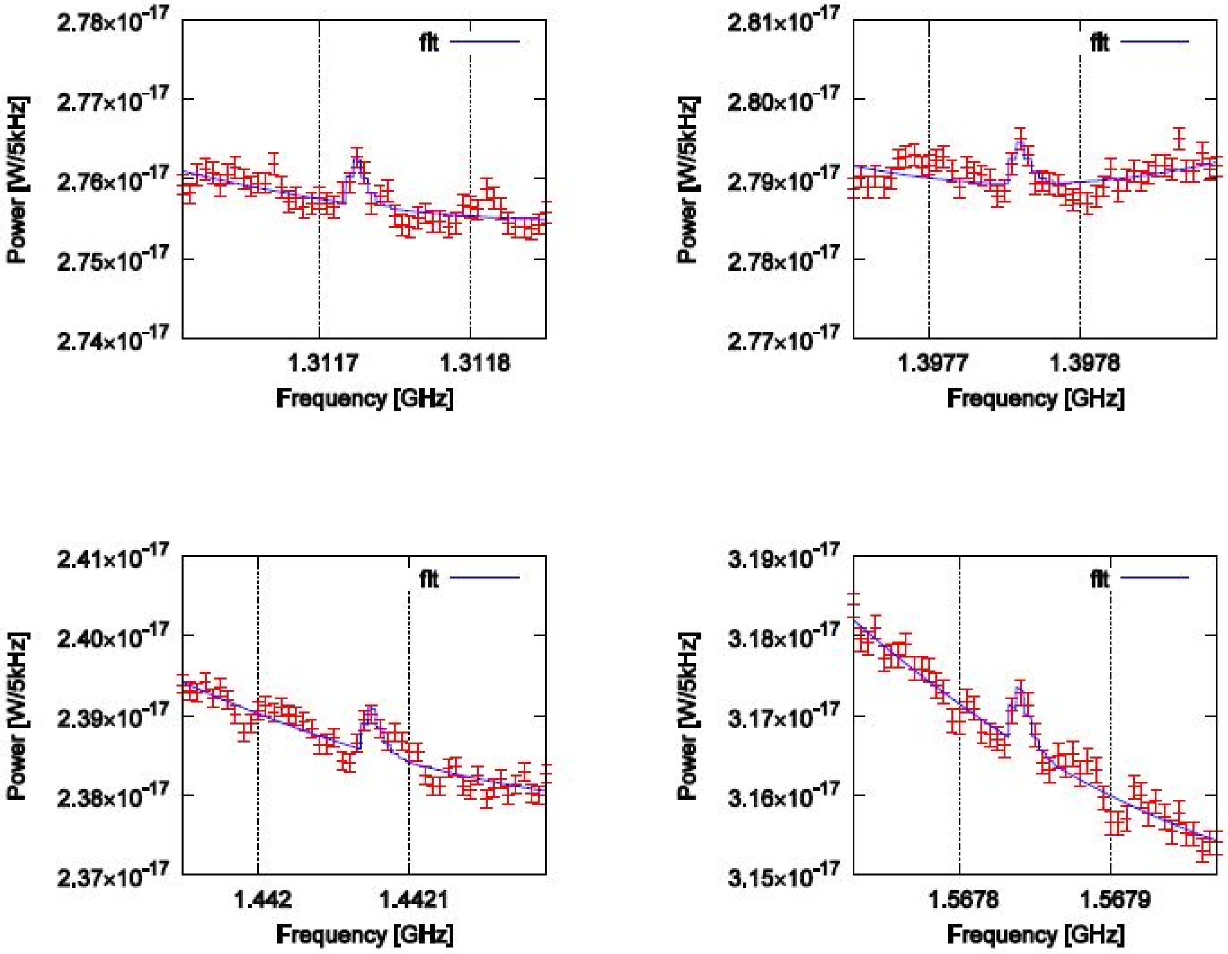

Figure 7.10: The spectra which exceed 4 σ

7.3 Upper limit of mixing parameter χ

In order to calculate upper limit of mixing parameter χ, let us recall the discussion of Sect. 3.2. Using Eq. (3.14) we can easily calculate the upper limit of χ from upper limit of the power of the electromagnetic wave derived from HPDMs P_{limit},

$$\chi_{95\%\mathrm{C.L.}} = 4.5\times10^{-14}\left(\frac{2\times P_{\mathrm{DM,95\%C.L.}}}{10^{-23}\mathrm{W}}\right)^{\frac{1}{2}}\left(\frac{0.3\mathrm{GeV/cm^3}}{\rho_{\mathrm{HP}}}\right)^{\frac{1}{2}}\left(\frac{1\mathrm{m}^2}{A_\mathrm{e}\times\mu_\Delta\times\mu_\theta}\right)^{\frac{1}{2}}\left(\frac{\sqrt{2/3}}{\alpha}\right). \tag{7.12}$$

where $P_{\mathrm{DM,95\%C.L.}}$ is the upper limit of the excess power which we estimeted in Sect. 7.2, μ_Δ represents the deterioration by the irregularity of the plane mirror, and μ_θ represent the deterioration by the incorrectness of the relative positions between the plane mirror and the parabolic antenna. Both of them, we discussed in Sect. 6.1. In Eq. (7.12), factor two for $P_{\mathrm{DM,95\%C.L.}}$ reflects the fact that the receiver can receive only a certain axis of polarization wave.

The error of the relative positions is estimated to be 0.2° as argued in Sect. 6.1. Moreover, the emission angle is not completely perpendicular to the surface of the plane mirror as argued in Sect. 3.2. The emission angle is estimated to be $\simeq |v_{\parallel}|/c$ where $v_{\parallel}$ is the component of v parallel to the surface of mirror. According to Eq. (7.5), HPDMs are expected to have velocity about $10^{-3}c$. Therefore the emission angle is estimated to be not more than 10^{-3} radian, i.e. $\simeq 0.057°$. Therefore, we estimated the total error of the emission angle to be 0.21°. It deteriorates the gain of the dish by the factor of 0.862.

On the other hand, the deviation of irregularity of the plane mirror is estimated to be not more than 1 mm. It deteriorates the gain of the dish by the factor of 0.930.

Eventually, we summarized the total deterioration of the dish gain in Tab. 7.2. Therefore, the effective area of the dish deteriorates to be $1.42\mathrm{m}^2$

Inserting the effective area of the dish and $P_{\mathrm{DM,95\%C.L.}}$ into the Eq. (7.12), we obtain the upper limit of χ as shown in Fig. 7.11. The abscissa is transformed from the frequency f_0 into hidden photon mass $m_{\gamma'}$ using Eq. (7.4).

Causation of deterioration	Degrees of deterioration
Irregularity of the plane mirror	0.930
Emission angle	0.862
Total	0.802

Table 7.2: Estimation of the deterioration of the dish gain

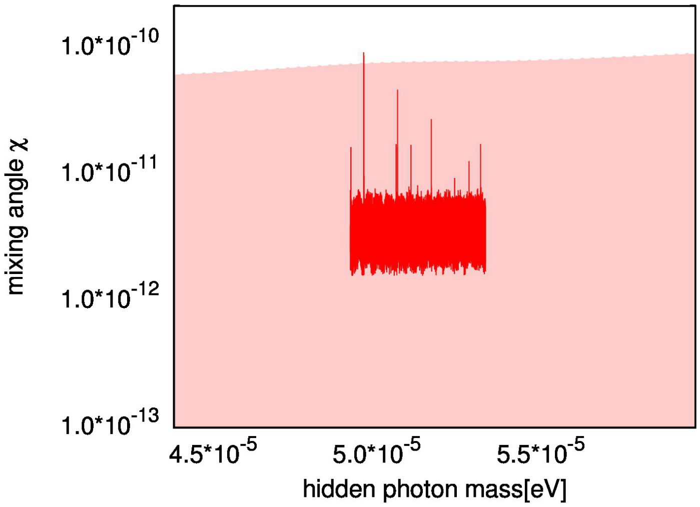

Figure 7.11: Upper limit on χ at 95% confidence level. The filled region with light-red denotes allowed region of HPDM. Note that, no upper limits were given for the mass corresponding to the connecting points between sub-sweeps because of the rough correction of the discontinuities shown in Tab. 6.5. Taking the frequency shifts into account, There are 8 points at every connecting points.

Chapter 8

Conclusion

We have searched for the hidden photon cold dark matter in the frequency range of about 12 GHz which corresponds to the hidden photon mass of 5×10^{-5}eV by using dish antenna method. The experimental apparatus is mainly constructed with the parabolic antenna and the plane mirror. We want to emphasize that there are two important achievements in our experiment. First, this is the world's first experimental search for HPDMs using a dish antenna. Second, using an auxiliary plane mirror, we enabled the use of a parabolic antenna instead of the originally proposed spherical antenna for the search of HPDMs.

In this experiment, we searched for excess emission of electromagnetic wave derived from the HPDMs. In the measurement, we found no significant excess of the power and we set the 95% confidence upper limits of mixing parameter χ as shown in Fig. 7.11 and Fig. 8.1. We set the upper limit of $2.0 \times 10^{-12} - 8.0 \times 10^{-12}$ to the mixing angle χ for the hidden photon mass between 49.1865 and 53.3195 μeV (except the connecting points of the sub-sweeps). This is currently the most stringent constraint in this hidden photon mass region.

The advantage of this method is that the same apparatus can be used in a broadband range of hidden photon masses by using a suitable receiver.

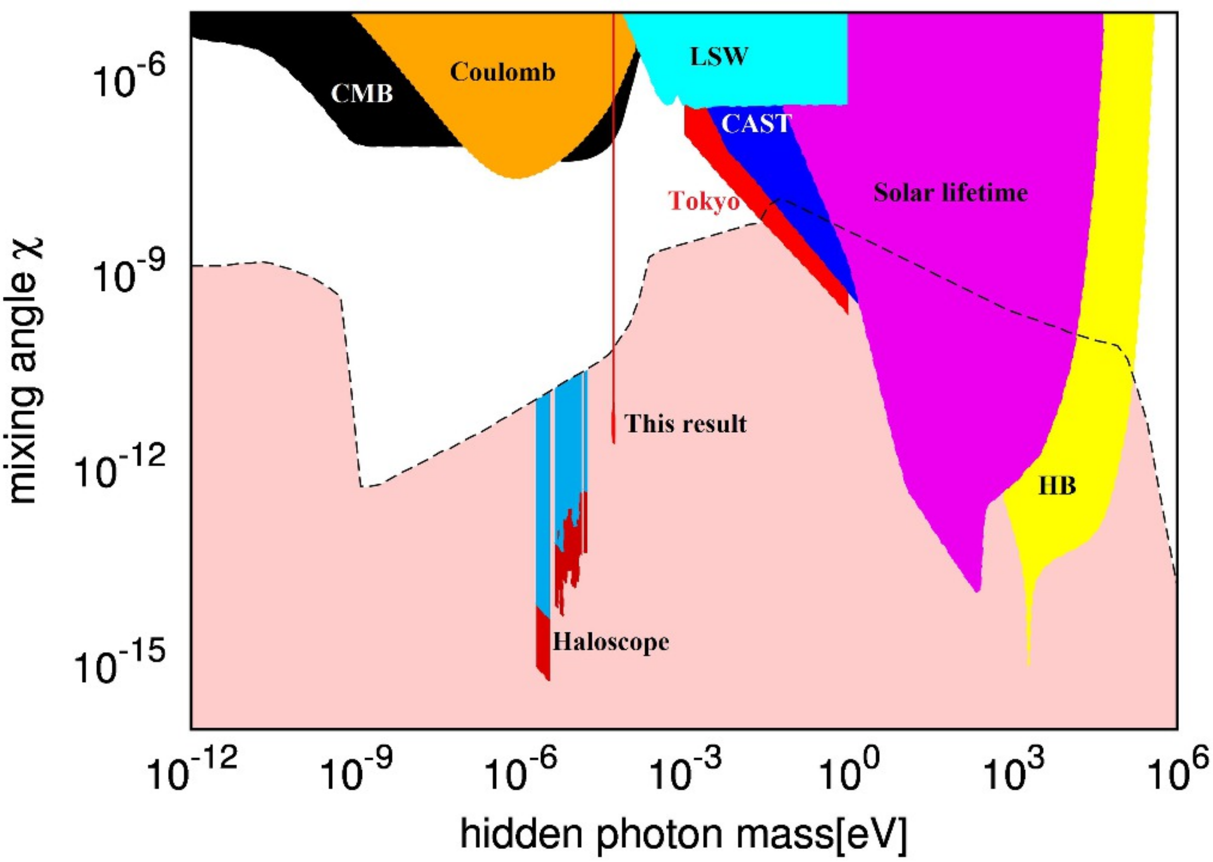

Figure 8.1: Upper limit on mixing parameter χ at 95% confidence level set by this experiment (filled red region). Note that, Note that, no upper limits were given for the mass corresponding to the connecting points between sub-sweeps because of the rough correction of the discontinuities shown in Tab. 6.5. Taking the frequency shifts into account, There are 8 points at every connecting points.

Acknowledgement

First of all, I am sincerely grateful to Professor M. Minowa. Without his guidance and persistent help this thesis would not have been possible. I'm deeply indebted to Y. Inoue for his advice. He gave insightful comments and suggestions. I want to deeply thank J. Suzuki for his assist of my work. I want to deeply thank all members of Minowa group. I further thank S. Otsuka for his advice and support of our engineering work.

This research is supported by the Grant-in-Aid for Challenging Exploratory Research by MEXT, Japan, Research Center for the Early Universe, School of Science, the University of Tokyo, and Advanced Leading Graduate Course for Photon Science (ALPS) at Unuversity of Tokyo.

Appendix A

Input from eccosorb

In order to derive the equation, we start from the description an antenna parameter. In the field of radio astronomy, it is useful to define so-called "beam solid angle" given by,

$$\Omega_{\mathrm{A}} = \int\int_{4\pi} P_n(\theta, \phi)\mathrm{d}\omega, \tag{A.1}$$

where $P_n(\theta, \phi)$ is the normalized power pattern defined as,

$$P_n(\theta, \phi) = \frac{1}{P_{\max}} P(\theta, \phi). \tag{A.2}$$

If a receiving antenna with a normalized power pattern $P_n(\theta, \phi)$ is pointed at a brightness distribution $B_\nu(\theta, \phi)$ in the sky, then the output of the total power is,

$$P_{\mathrm{tot}} = \frac{1}{2} A_{\mathrm{e}} \int\int B_\nu(\theta, \phi) P_n(\theta, \phi)\mathrm{d}\Omega, \tag{A.3}$$

where A_{e} is the (effective) area of the antenna (so-called effective aperture). The factor 1/2 arises from the reason that the LNBF receives a certain axis of polarization wave, but it can not receive another one.

Eq. (A.1) is convenient when the input power is isotropic. For example, let us consider the situation that a parabolic antenna which has the beam solid angle is in a box, and the box is "black" at the frequency of interest. If $h\nu \ll kT$[1], the input power of black body radiation (with frequency bandwidth $\Delta\nu$) from the box is,

$$B_\nu = \frac{2kT_1}{\lambda^2}\Delta\nu, \tag{A.4}$$

where T_1 is the temperature of the box. It is equal in any direction, so we get the output power by inserting Eq. (A.1) and Eq. (A.4) into Eq. (A.3),

$$A_{\mathrm{e}} \frac{kT_1}{\lambda^2}\Delta\nu\Omega_{\mathrm{A}}, \tag{A.5}$$

---

[1] The situation which we focused on is that the frequency is about 12GHz and temperature is about 300K or 77K. The frequency is equal to about 5×10^{-6}eV, the temperatures are equal to 2.6×10^{-2} and 6.6×10^{-3}. So the situation meets the condition.

On the other hand, according to the Nyquist theorem, output noise power from the circuit including the LNBF (with frequency bandwidth $\Delta\nu$),

$$kT_2\Delta\nu. \tag{A.6}$$

where T_2 is the temperature of the circuit.

If they are in thermal equilibrium, i.e. $T_1 = T_2 (= T)$, we find,

$$A_{\mathrm{e}}\frac{kT}{\lambda^2}\Delta\nu\Omega_{\mathrm{A}} = kT\Delta\nu, \tag{A.7}$$

thus,

$$A_{\mathrm{e}}\Omega_{\mathrm{A}} = \lambda^2 \tag{A.8}$$

This equation is independent of temperature, so the equation is valid even if they are not in thermal equilibrium.

Now, let us come back to the discussion about the eccosorb measurement. The view angle of the LNBF corresponds roughly to the solid angle. So if we set the eccosorb so that it can cover the entire visual field of the LNBF, the LNBF collects a total power of

$$W = A_{\mathrm{e}}\frac{kT_1}{\lambda^2}\Delta\nu\Omega_{\mathrm{A}}. \tag{A.9}$$

According to Eq. (A.8), we find,

$$W = kT\Delta\nu. \tag{A.10}$$

Appendix B

Dish gain and free-space path loss

In this appendix, we derive the formulas of Dish gain and free-space path loss.

At first, let us consider ideal lossless isotropic antenna. According to Eq. (A.9), the isotropic antenna has $\Omega_A = 4\pi$. So, we find the effective aperture of the antenna,

$$A_{e,\mathrm{isotropic}} = \frac{\lambda^2}{4\pi}. \tag{B.1}$$

In the field of radio astronomy, it is general to define the dish gain as,

$$G_d = \frac{4\pi A_e}{\lambda^2}. \tag{B.2}$$

It has the same meaning of the effective aperture normalized by $A_{e.\mathrm{isotropic}}$.

On the other hand, let us consider the situation that an isotropic antenna for reception and another isotropic antenna for transmission are separated by a distance d. The power of the signal from the transmission antenna P_t is weakened by the propagation broadening. The received power per unit area is,

$$\frac{P_t}{4\pi d^2}. \tag{B.3}$$

On the other hand, the effective aperture of isotropic antenna is represented by Eq. (B.1) . Then we find the total received power.

$$P_d = \frac{P_t}{4\pi d^2} \times \frac{\lambda^2}{4\pi} = P_t \left(\frac{\lambda}{4\pi d}\right)^2 \tag{B.4}$$

By comparison with the transmission power P_t, the degree of weakening can be calculated by P_d / P_t This weakening is defined as free-space path loss,

$$\mathrm{Ls} = \left(\frac{\lambda}{4\pi d}\right)^2 \tag{B.5}$$

Appendix C

The source of the narrow peaks

In our experiment, several narrow peaks were found. The bandwidth of the peaks is roughly same as the bandwidth HPDMs may have. We investigated the origin of these peaks.

We defined it a peak if there are three or more consecutive sweep points which have more than three-sigma excess above the baseline.

In Fig. 7.4, there are some peaks which satisfy the selection condition in the nine frequency ranges shown in Tab. C.1.

The peak around 1050 MHz is the signal from the signal generator discussed in Sect. 6.2. Therefore, we excluded this frequency range for the investigation.

There is a peak in the sub-sweep of 1450 to 1500 MHz, but it was recorded only two times in the 2700-times sub-sweeps. The sub-sweep spectra when the peak arose are shown in the center of Fig. C.1. Sub-sweep spectra just before and immediately after the sub-sweep with the peak are also shown above and below the spectrum in question, respectively. It is very unlikely for the HPDM signal to appear in a certain moment and go off quickly. Therefore, there is no possibility that this peak is derived from HPDMs.

For other seven peaks, we investigated whether the peaks are derived from HPDMs or not in the following ways:

- In order to shield the receiver from the possible radio wave of HPDM origin, we set an aluminum plate of 220 mm× 300 mm in front of the receiver with gap of 30mm.
- We detached the receiver from the parabolic antenna and set the receiver outside of the apparatus.

In these conditions and the setup for the HPDM search, we conducted the measurements for the seven frequency ranges with RBW=1kHz. The results are shown in Fig. C.2 and the Fig. C.3. All the peaks arose even in the setup with the shield and detached receiver. Furthermore, the power of these peaks got maximized when we pointed the receiver toward the FFT analyzer. Therefore, the source of these peaks were not HPDMs, but the FFT analyzer.

Frequency range for investigation [MHz]
603.9 to 604.3 MHz
699.4 to 700.75 MHz
939.45 to 939.85 MHz
950.0 to 950.4 MHz
(1050 MHz)
1199.95 to 1200.35 MHz
1371.9 to 1372.1 MHz
1450 to 1500 MHz
1563.8 to 1564.2 MHz

Table C.1: Frequency ranges which have the peaks. 1050 MHz corresponds to the frequency of the reference signal from the signal generator.

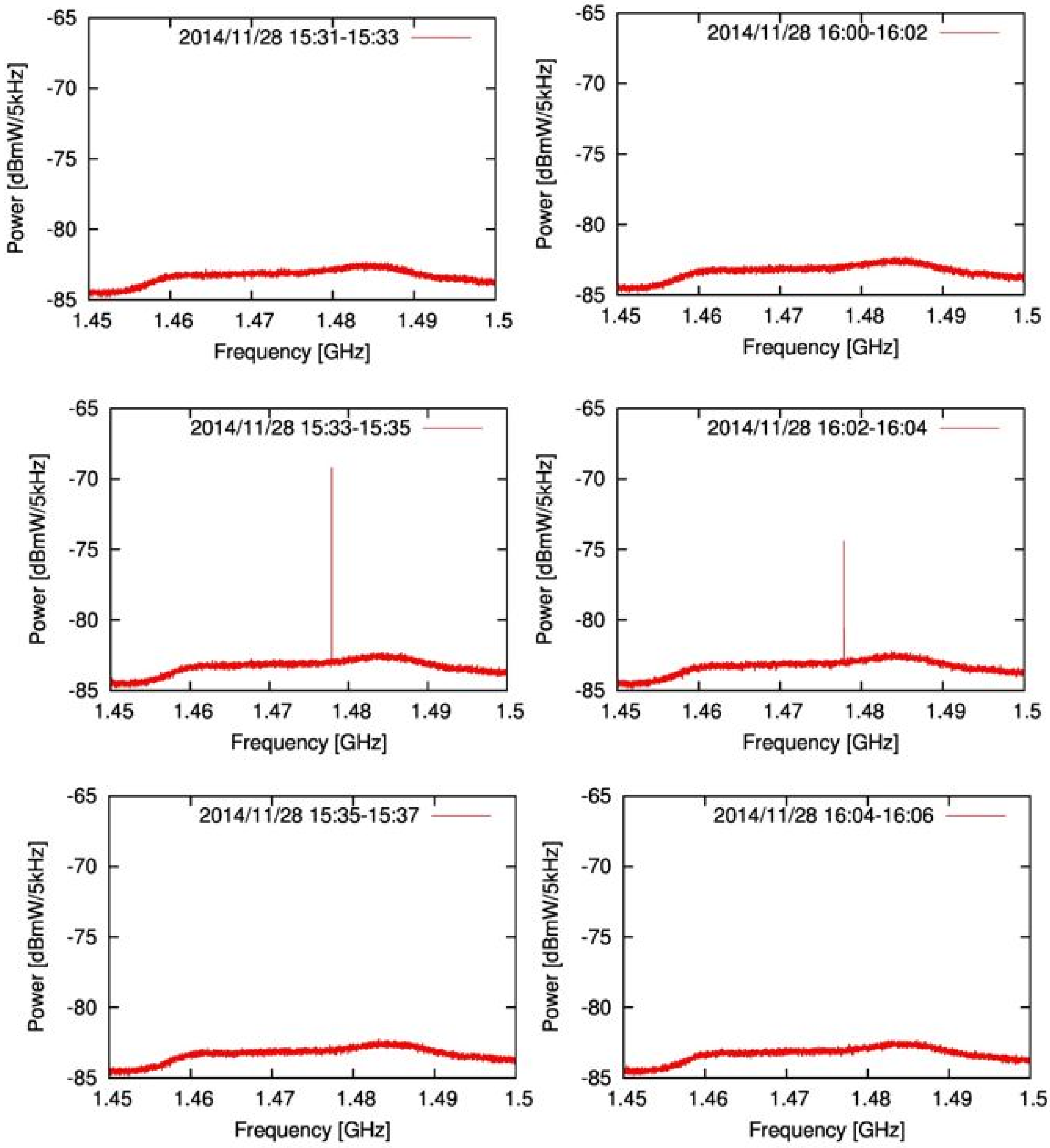

Figure C.1: Two figures of the center show the peaks at about 1478MHz. However, the peaks did not arise in the sub-sweep spectra just before and immediately after these two sub-sweeps as shown in the above and below figures. The times shown in the figures represent the start and finish time of the single sweep.

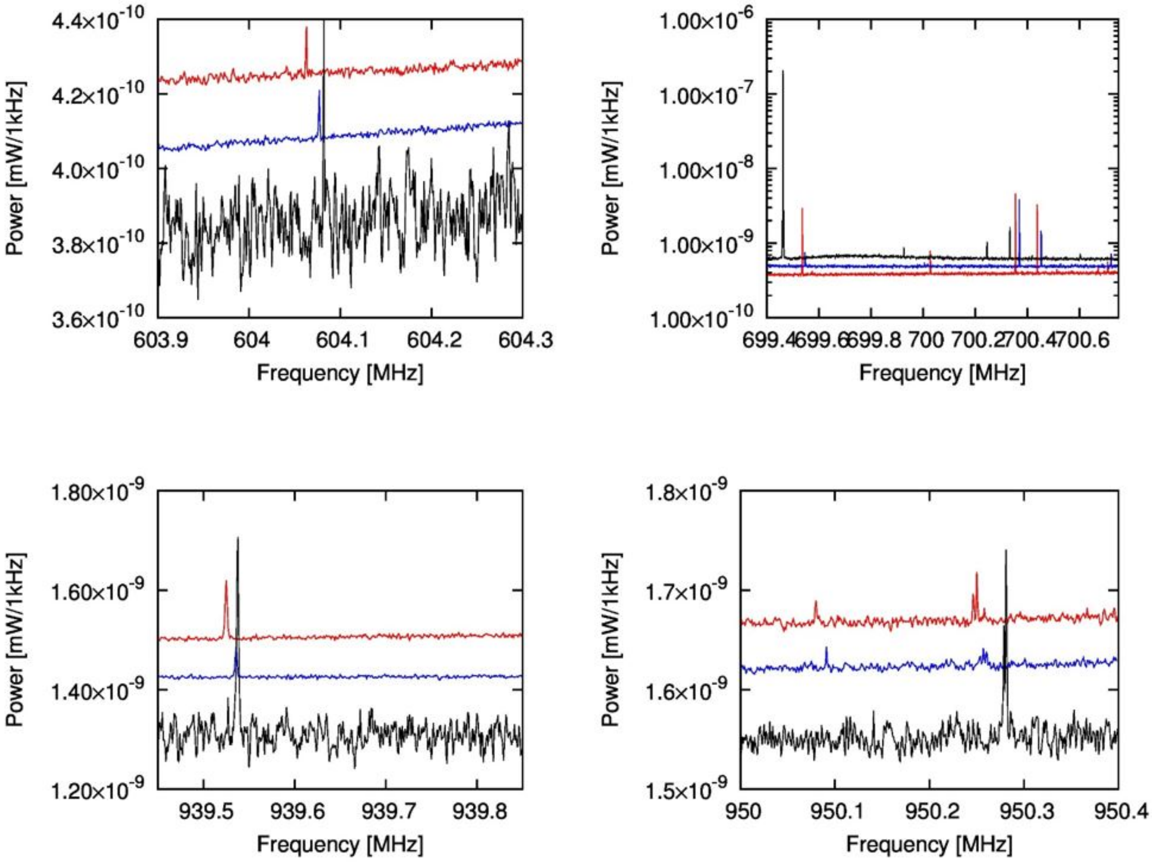

Figure C.2: Spectra under three different setups. The red line was measured with the setup for the HPDM search. The blue line was measured with the shield in front of the receiver. The black line was measured detaching the receiver from the parabolic antenna.

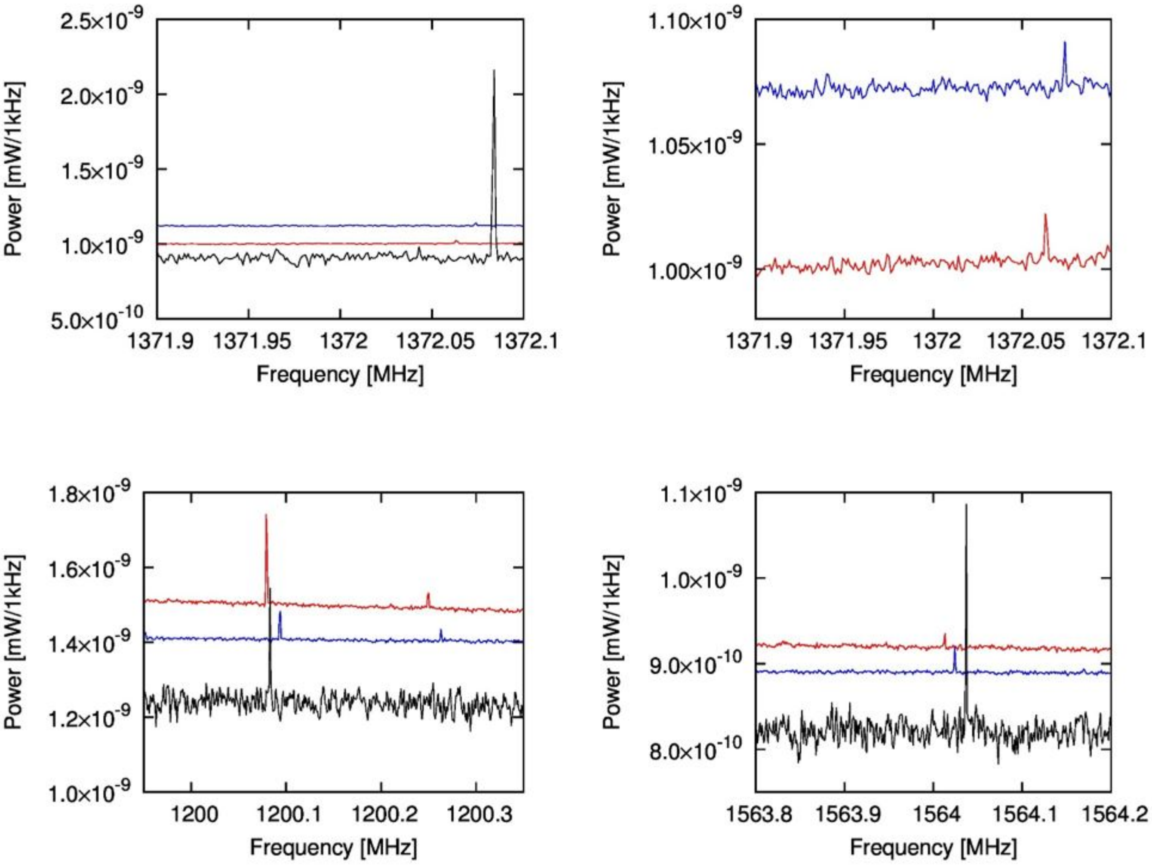

Figure C.3: Spectra under three different setups. We show the figures in the same manner as Fig. C.2. For the spectrum around 1372 MHz shown in the upper left, the peak of black line is much larger than the others. Therefore, we show the other lines separately in the upper right.

Appendix D

Power averaging

We examined how a peak of single frequency is broadened in calculating FFT. We connected the signal generator and the FFT analyzer directly. The output frequency of the signal generator was set to 35 MHz, and output power was set to -40dBm. The setting values of the FFT analyzer was same as the setup for search for HPDMs except that center frequency was set to 35 MHz (Fig. D.1). We calculated the ratio of the power in a bin adjacent to the peak to the total power based on the result of this measurement, and we obtained the ratio value $\simeq 0.074$.

This means that they have a correlation, and a power of a certain bin was averaged by the both side bins. As a result, standard error is made small, for example, the standard error of the n-th bin σ_{P_n} is averaged by neighboring bins as follows;

$$\sigma'_{P_\mathrm{n}} = \sqrt{0.074^2 \times \sigma^2_{P_\mathrm{n-1}} + (1 - 2 \times 0.074)^2 \times \sigma^2_{P_\mathrm{n}} + 0.074^2 \times \sigma^2_{P_\mathrm{n+1}}}. \tag{D.1}$$

Assuming that the standard error of respective bins are equal, σ'_{P_n} is about 0.86 times as large as σ_{P_n}.

The effect accordingly broadens the distribution of P/Δ_P like the one seen in Fig. 7.6. If a power of a bin is larger than the baseline accidentally, the power of the neighboring two bins become large by the correlation, therefore these bins look more similar to the HPDM signal described in Fig. D.1.

We made Monte Carlo simulations to estimate to what extent the distribution of P/Δ_P is modified by the above effect, and to compare it with the result of HPDM search (Sect. 7.2). For the simulation, we supposed a simple model in which there is no distortion of baseline (Fig. D.2). We conducted two simulations. In the first simulation, random power is given to each 5kHz bin with a mean zero and the standard error estimated in Chap. 5. Then, we allow the power of each bin to spill over into the neighboring bins as estimated above in the second simulation. The distributions of P/Δ_P computed from the two simulations are shown in Fig. D.3. In the second case, the distribution was broadened. We fitted the Gaussian in the same way which we explained in Sect. 7.2, and the result of the fitting was $\sigma = 1.1277 \pm 0.00185$. This corresponds to the standard error which we calculated in Sect. 7.2.

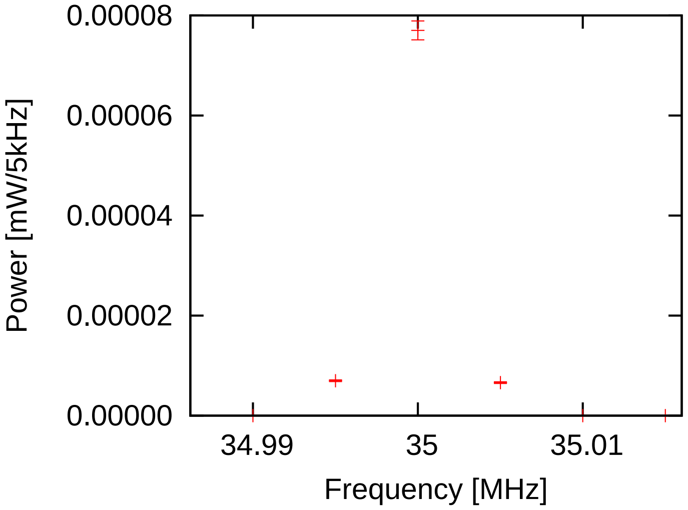

Figure D.1: The signal of the frequency 35MHz from the signal generator

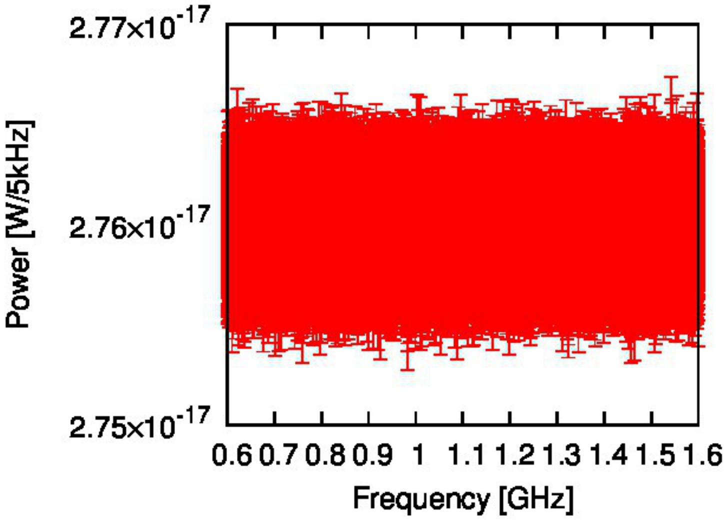

Figure D.2: The virtual input for estimating to what extent the distribution of P/Δ_P

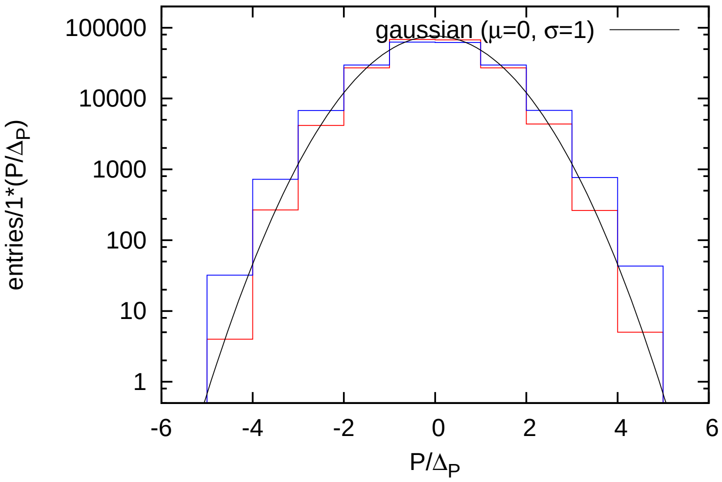

Figure D.3: The comparison of the distributions of P/Δ_P

Bibliography

[1] P. A. R. Ade *et al.* [Planck Collaboration], arXiv:1303.5076 [astro-ph.CO]

[2] J. Jaeckel and A. Ringwald, Ann. Rev. Nucl. Part. Sci. **60** (2010) 405 [arXiv:1002.0329 [hep-ph]].

[3] G. Bertone *et al.*, Phys. Rept. **405** (2005) 279 [hep-ph/0404175].

[4] J. Preskill *et al.*, Phys. Lett. B **120** (1983) 127.

[5] L. Abbott and P. Sikivie, Phys. Lett. B **120** (1983) 133.

[6] M. Dine and W. Fischler, Phys. Lett. B **120** (1983)137.

[7] L. B. Okun, Sov. Phys. JETP **56**, (1982) 502 [Zh. Eksp. Teor. Fiz. **83**, (1982) 892].

[8] B. Holdom, Phys. Lett. B **166** (1986) 196.

[9] T. Mizumoto *et al.*, JCAP **07** (2013) 013 [arXiv:1302.1000[astro-ph]].

[10] J. Redondo, JCAP **0807** (2008) 008 [arXiv:0801.1527 [hep-ph]].

[11] K. Ehret *et al.*, Phys.

[12] J. Redondo and M. Postma, JCAP **0902**, (2009) 005 [arXiv:0811.0326[hep-ph]].

[13] P. Arias *et al.*, JCAP **1206**, (2012) 013 [arXiv:1201.5902[hep-ph]].

[14] A. E. Nelson and J. Scholtz, Phys. Rev. D **84** (2011) 103501 [arXiv:1105.2812 [hep-ph]].

[15] S. De Panfilis, *et al.*, Phys. Rev. Lett. **59** (1987) 839.

[16] W. Wuensch *et al.*, Phys. Rev. D **40** (1989) 3153.

[17] C. Hagmann *et al.*, Phys. Rev. D **42** (1990) 1297.

[18] S. J. Asztalos *et al.*, Phys. Rev. D **64** (2001) 092003.

[19] S. J. Asztalos *et al.* [The ADMX Collaboration], Phys. Rev. Lett. **104** (2010) 041301 [arXiv:0910.5914 [astro-ph.CO]].

[20] M. Tada *et al.*, Nucl. Phys. Proc. Suppl. **72** (1999) 164.

[21] J. Ruze, Suppl. Nuovo Cimento, **9** (1952) 364.

[22] J. Ruze, Proc. IEEE, **54** (1966) 633.

[23] D. Horns *et al.*, JCAP **1304**, (2013) 016 [arXiv:1212.2970[hep-ph]].

[24] K. M. Cudworth, Astron. J. **99** (1990) 590.

[25] C. S. Kochanek, Astrophys. J. **457** (1996) 228.

[26] McNeill and Partick L. Ryan, Master thesis, UNIVERSITY OF NORTH TEXAS (2002) `http://digital.library.unt.edu/ark:/67531/metadc5801/m2/1/high_res_d/thesis.pdf`

[27] D. Budker *et al.*, Phys. Rev. X **4**, (2014) 021030 [arXiv:1306.6089 [hep-ph]].